Amélioration de la modélisation 2D et 3D de vagues déferlantes en milieu maritime

Sunil Mohanlal

École des Ponts ParisTech

THÈSE DE DOCTORAT

de l'École des Ponts ParisTech

Amélioration de la modélisation 2D et 3D de vagues déferlantes en milieu maritime

École doctorale N°531, Sciences, Ingénierie et Environnement (SIE)

Mécanique des fluides

Thèse préparée au **Laboratoire d'Hydraulique Saint-Venant**

Thèse soutenue publiquement le 27/11/2023, par **Sunil MOHANLAL**

Composition du jury:

Guillaume Ducrozet Professeur, École Centrale de Nantes	*Président du Jury*
Yves-Marie Scolan Professeur, ENSTA Bretagne	*Rapporteur*
Alessandro Iafrati Directeur de recherche, Istituto di Ingegneria del Mare	*Rapporteur*
Alison Raby Professeure, University of Plymouth	*Examinatrice*
Michel Benoit Professeur, LHSV & EDF R&D	*Examinateur*
Jeffrey Harris Chargé de recherche, LHSV & ENPC	*Directeur de thèse*
Luc Pastur Professeur associé, ENSTA Paris	*Co-directeur de thèse*
Marissa Yates Chargée de recherche, LHSV & ENPC	*Co-encadrante de thèse*
Christophe Peyrard Ingénieur, Chercheur expert, EDF R&D, LNHE	*Invité*
Stéphan Grilli Professeur, University of Rhode Island	*Invité*

Thèse effectuée au sein du **Laboratoire d'Hydraulique Saint-Venant**

de l'École des Ponts ParisTech

6, quai Watier

BP 49

78401 Chatou cedex

France

Résumé

Les modèles d'écoulement potentiel non-linéaire ont été largement utilisés pour diverses applications, notamment la propagation d'ondes non-linéaires et dispersives à différentes profondeurs d'eau, la modélisation de la transformation des vagues sur des pentes abruptes, l'étude des interactions non-linéaires des vagues avec des structures fixes et flottantes et la simulation des vagues qui se retournent (utilisant une formulation Lagrangienne), entre autres applications.

De plus, ces modèles ont été appliqués pour simuler des phénomènes spécifiques qui ne pourraient pas être pris en compte dans les hypothèses d'écoulement irrotationnel et non visqueux, tels que le frottement du fond dans les eaux peu profondes, les effets visqueux et le déferlement des vagues. Ces dernières années, il y a eu un intérêt croissant dans la compréhension des vagues déferlantes, en particulier dans le contexte de conditions de vagues extrêmes. Cette étude se concentre sur le développement d'un modèle paramétré de déferlement de vagues dans les modèles d'écoulement potentiel non linéaire, en mettant l'accent particulièrement sur un modèle basé sur la physique enlever du phénomène et en garantissant une applicabilité plus large en minimisant le nombre de paramètres de calibration.

Tout d'abord, les vagues déferlantes 2D (i.e., à crête longue) sont explorées. Un modèle paramétré de détection et de dissipation de déferlement est présenté pour des ondes déferlantes 2D à profondeur limitée. Le modèle intègre un critère universel de début de déferlement et un nouveau modèle de dissipation. Le modèle proposé est validé avec des vagues régulières et irrégulières déferlantes, y compris des déferlantes glissantes et plongeantes sur des barres et des pentes submergées. Un autre modèle paramétré de déferlement est proposé pour les ondes déferlantes à cambrure limitée en 2D, utilisant le même paramètre d'initiation de déferlement que le modèle précédent, ainsi qu'un modèle de dissipation de la littérature, basé sur le paquet d'ondes d'entrée. Ce modèle est ensuite validé à l'aide d'expériences en laboratoire avec des ondes déferlantes focalisées.

Enfin, le modèle proposé de dissipation 2D à profondeur limitée est étendu aux ondes déferlantes 3D à profondeur limitée. Cette extension nécessite de diviser les fronts d'onde en subdivisions plus petites jusqu'à un certain degré, où les conditions d'onde peuvent être supposées constantes sur toute la longueur de chaque subdivision. Par conséquent, ces subdivisions individuelles sont traitées comme des ondes 2D à crête longue. Le modèle proposé est validé avec des vagues déferlantes glissantes et plongeantes sur une barre submergée 3D et un bosse elliptique focalisant, dans le but prospectif d'appliquer les modèles d'écoulement potentiel non-linéaire pour la simulation des vagues déferlantes sur des sites offshore.

Mots-clé:

L'écoulement potentiel non linéaire; Début de déferlement des vagues; Dissipation de déferlement des vagues; Vague déferlante à profondeur limitée; Vague déferlante à cambrure limitée.

Improvement of the 2D and 3D modeling of breaking waves in a maritime environment

Abstract

Fully nonlinear potential flow models (FNPF) have been extensively employed for diverse applications, including the propagation of nonlinear and dispersive waves in varying water depths, modeling wave runup over steep slopes, investigating nonlinear wave interactions with fixed and floating structures, and simulating overturning waves (using a Lagrangian formulation), among other applications.

Additionally, FNPF models have been applied to simulate specific phenomena that might not be accounted for under the irrotational and inviscid flow assumptions, such as bottom friction in shallow water, viscous effects, and wave breaking. In recent years, there has been growing interest in understanding breaking waves, particularly in extreme wave conditions. This study focuses on the development of a parameterized wave breaking model for FNPF models, with a specific emphasis on basing the model on the underlying physics of the phenomenon and ensuring broader applicability by using minimal calibration parameters.

Firstly, 2D (i.e., long-crested) breaking waves are explored. A parameterized breaking detection and dissipation model is presented for 2D depth-limited breaking waves. The model incorporates a universal breaking onset criterion and a newly derived dissipation strength model. The proposed model is validated with regular and irregular breaking waves, including spilling and plunging breakers over submerged bars and slopes. Another parameterized breaking model is proposed for 2D steepness-limited breaking waves, utilizing the same onset parameter as the previous model, with a dissipation strength model from the literature, based on the input wave packet. This model is then validated using laboratory experiments of focused breaking waves.

Finally, the proposed 2D depth-limited dissipation model is extended to 3D depth-limited breaking waves. This extension involves dividing wavefronts into smaller subdivisions, where wave conditions can be assumed constant across the span of each subdivision. Consequently, these individual subdivisions are treated as 2D long-crested waves. The proposed model is validated with spilling and plunging breaking waves over a 3D submerged bar and an elliptical shoal, with the prospective aim of applying FNPF models for the simulation of breaking waves at offshore locations.

Keywords:

Fully non-linear potential flow; Breaking onset; Breaking dissipation; Depth-limited breaking; Steepness-limited breaking.

Remerciements

I would like to thank E4C for funding this thesis for the past three years. I would like to thank my advising committee, whose collective efforts have shaped this work; without them, this thesis would not have been possible. I am deeply thankful to my advisor, Jeffery, whose exceptional guidance, valuable insights, and constant availability, even amidst busy schedules, have been invaluable. I would also like to thank him for making it possible for me to go to two international conferences! Special thanks to Marissa for introducing me to wave modeling and wave breaking during my master's internship at LHSV and for her pivotal role in putting together this thesis, as well as her valuable contributions to my research and write-ups over the last three and a half years. I would also like to thank Luc and Christophe for their help in putting together this thesis.

I express my gratitude to the rapporteurs, Yves-Marie Scolan and Alessandro Iafrati, for dedicating their time to evaluate this thesis manuscript. I extend my appreciation to the examiners, Guillaume Ducrozet, Alison Raby, and Michel Benoit, for agreeing to be part of my thesis jury. Special thanks to Stéphan Grilli for engaging in insightful discussions over the past three years and for being a valuable part of this work. Additionally, I would like to acknowledge Lili Kimmoun for providing experimental data on steepness-limited breaking waves, which greatly contributed to the content of Chapter 3.

I wish to express my appreciation to my office mates at LHSV, including Rémi, Jiaze, Jiankai, Prokopios, Zied, and Faten, who made my time here truly memorable. Special thanks to Mehdi for his encouragement during the final stages of manuscript completion. My gratitude also extends to the wonderful colleagues I had the pleasure of getting to know at LHSV: Teddy, Marc, Elie, Antoine, Bastien, Noémie, Fatna, Elisa, Maxime, Guillaume, and Jean-Paul for the enriching discussions and shared laughter. I extend my deepest gratitude to Sébastien Bourban for introducing me to HR Wallingford!

I extend my gratitude to Uday for all the memorable student days since my bachelor's degree that I will forever cherish. Additionally, I express my thanks to Karthik, Ram, Nistha, and Sai for their companionship during various memorable adventurous trips over the past three years.

Finally, and most importantly, I express my heartfelt gratitude to my parents, sisters, and my love for their constant encouragement throughout the journey of this thesis.

Contents

List of Figures

List of Tables

Chapter 1

Introduction

Le déferlement des vagues est un phénomène dissipatif complexe crucial pour comprendre les courants côtiers qui entraînent le transport des sédiments et les charges de claquement sur les structures offshore. Il s'agit donc d'un phénomène d'une très grande importance, et qui n'est pas encore bien compris. Plusieurs études expérimentales ont été menées pour comprendre ce phénomène. Il est possible de simuler des vagues déferlantes dans les modèles Navier-Stokes, cependant, nous sommes actuellement limités à de petits domaines spatiaux et temporels en raison des coûts de calcul et des erreurs. Avec un besoin toujours croissant de comprendre l'évolution des états de la mer irréguliers à l'échelle d'un site offshore avec les effets du déferlement des vagues, nous avons besoin de modèles simplifiés numériquement avec lesquels nous pouvons atteindre ces objectifs. Nous examinons ici le contexte de cette étude, les modèles simplifiées développées au fil des ans, suivis de l'état de l'art de la compréhension des vagues déferlantes à partir des observations expérimentales ainsi que des modèles de haute fidélité et de la manière dont ces informations sont utilisées pour simuler explicitement le déferlement des vagues. Enfin, l'organisation du reste du manuscrit est présentée.

1.1 Context

In recent years, the European Union (EU) has set ambitious goals to become carbon-free within the next few decades, leading to significant growth in the renewable energy sector (*IEA, Net Zero by 2050* 2021; *IEA, Renewables* 2022). With the presence of vast coastlines and large regions covered with water, offshore wind energy has gained major interest, particularly with floating and fixed wind turbines (*IEA, Offshore Wind Outlook* 2019), as compared to the other existing sectors such as solar energy. Consequently, extensive research has been conducted over the past decade to better understand the irregular evolution of sea states around these structures, for example, the work in Filipot et al. 2018, where extreme sea states are captured with a focus on their wave breaking properties to help in refining the design conditions for Marine Renewable Energy Converters. Funded by Energy4Climate (E4C), an organization that focuses on research for achieving a clean energy transition, this thesis is aimed at improving and developing numerical models that could be used to simulate and study these site-scale sea states.

There exist many Navier-Stokes models of water waves (e.g., Liu et al. 1999; Dalrymple & Rogers 2006; Higuera et al. 2013) with Direct Numerical Simulation (DNS) (e.g., Moin & Mahesh 1998; Deike et al. 2016; De Vita et al. 2018), or Large Eddy Simulation (LES) models, where one can include the effect of eddies through turbulence modeling (e.g., Deardorff 1970; Lubin & Glockner 2015), which can simulate fully nonlinear and dispersive waves with bathymetric effects, breaking waves, and wave structure interactions.

Nevertheless, the computational resources required for these models limit their applicability to small domains. For instance, an intercomparison study conducted by Vyzikas et al. 2020 reveals that the computational cost of running OpenFOAM, a RANS model, is approximately three orders of magnitude higher than that of SWASH (Simulating WAves till SHore; Zijlema et al. 2011), a nonlinear shallow water wave model, and the computational cost of SWASH is approximately one order of magnitude higher than that of HOS-NWT (High Order Spectral - Numerical Wave Tank; Ducrozet et al. 2012), a potential flow (irrotational and inviscid) model.

A simplified model implies certain assumptions about the physics of the flow. In general, more assumptions lead to a simpler model, which in turn leads to faster calculations and vice versa. Therefore, a choice has to be made with respect to the extent of physics to be modeled and the computational costs. The type of waves that are of interest for designing offshore wind turbines are the extreme ones (most energetic) that are large, steep, and highly nonlinear, as they carry a large amount of energy with them that could potentially damage or destroy these deployed structures. Thus, the model of interest should avoid making any assumptions about the nonlinearity or dispersion of the waves. Among the computationally efficient ones that respect these assumptions are fully nonlinear potential flow (FNPF) models, which are therefore used for this study.

FNPF models consider the flow to be irrotational and inviscid, and in the presence of breaking waves, are limited up to the instant the free surface becomes vertical (those with an Eulerian frame of reference), or in some models (those with a Lagrangian frame of reference) up to when

the overturning wave hits the free surface (Fig. 1.1). However, through parameterized modeling, several numerical techniques have been developed in the past few decades to model breaking waves in numerically simplified models, such as FNPF. The parameterized modeling of breaking waves generally requires identifying the instant wave breaking dissipation begins, the magnitude of dissipation applied to a determined region, and the duration this dissipation would continue.

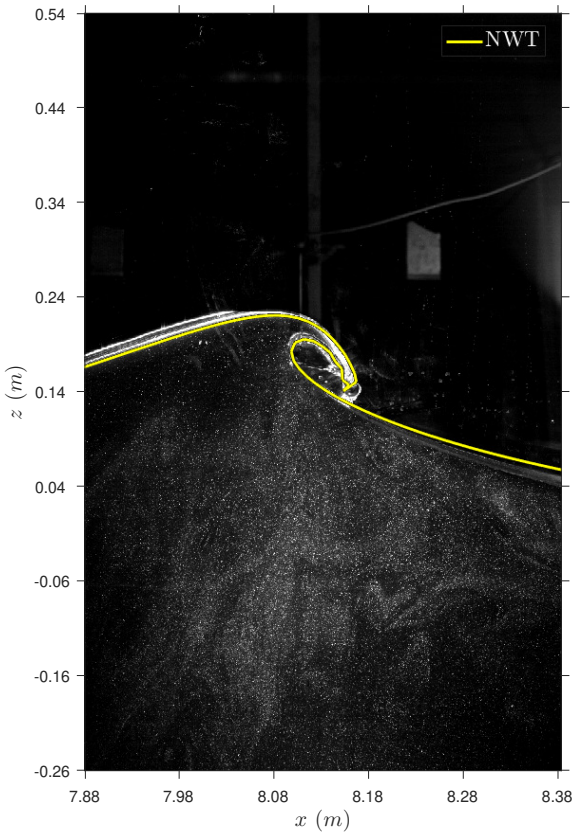

Figure 1.1: A wave at the moment the overturning jet hits the free surface. The yellow line represents simulation results from the Numerical wave tank (NWT, described in Chapter 2), a fully nonlinear potential flow model. The experimental data are from Lili Kimmoun.

Some breaking waves, for example, the less violent ones in which the breaking event is seen as white foam rolling down on the front face of the wave (e.g., spilling breaking waves), have been shown to resemble another analytically studied dissipative mechanism, a hydraulic jump (Svendsen et al. 1978; Stive 1984), which makes them easier to model. However, a general understanding of breaking waves is still a field of active research. Therefore, most of the attempts made in the previous few decades to model breaking waves in numerically simple models have been defined for specific types of breaking waves and often have test case-dependent parameters that require calibration (Kennedy et al. 2000; Guignard & Grilli 2001; Papoutsellis et al. 2019; Simon et al. 2019). Therefore, there is a need to obtain a general wave breaking model that can be applied to irregular sea states where one might expect any type of breaking waves.

1.2 Basics of wave motion

A progressive monochromatic wave in depth d is defined by its time period (T), wave height (H), wavelength (L), and wave celerity (c) (Fig. 1.2). Under linear assumptions, i.e., $H/d \ll 1$, and $H/L \ll 1$, the free surface elevation can be written as $\eta = A\cos\theta$, with $\theta(x,t) = kx - \omega t + \varphi$ where $A = H/2$, is the wave amplitude, k, the wave number, ω, the wave angular frequency, and φ, the phase. A wave can also be characterized by its horizontal and vertical velocities (u, w). For describing waves, instead of the above ratios (H/d and H/L), often the quantities $\epsilon = kA$, termed as the nonlinearity parameter, and $\mu = kd$, termed as the dispersion parameter are used.

Under the linear assumptions, the quantities ω and k can be related to each other with the linear dispersion relation (Dean & Dalrymple 1991),

$$\omega^2 = gk\tanh(kd) \tag{1.1}$$

where $\omega = 2\pi/T = 2\pi f$ and $k = 2\pi/L$. The phase speed ($c = \omega/k$), or celerity, can also be defined as the rate of change of displacement of a crest in time. In shallow water depth (i.e., $d/L < 1/20$), the Eq. 1.1 reduces to $c = \sqrt{gd}$ and in deep water conditions (i.e., $d/L > 1/2$) to $c = gT/2\pi$.

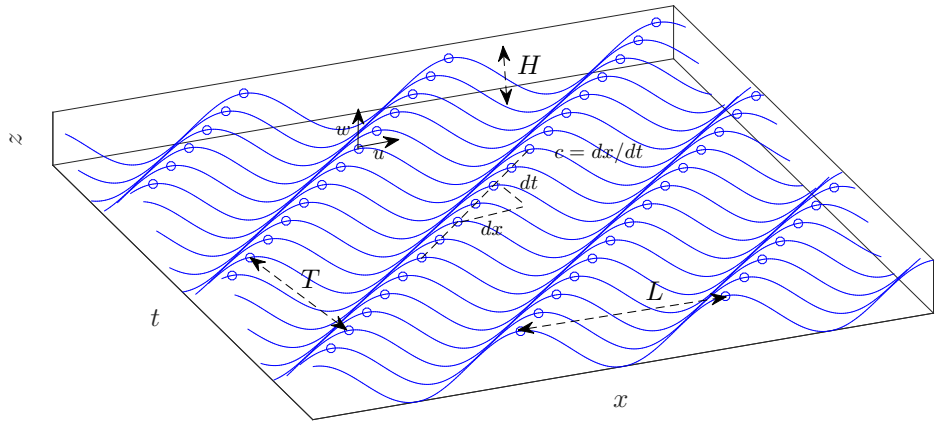

Figure 1.2: General characteristics of a progressive 2D (x, z) monochromatic wave with wavelength, L, wave height, H, period, T, phase speed, c, and horizontal and vertical particle velocities, u, w, respectively.

An irregular sea state cannot be represented by a single monochromatic wave. It is instead taken to be a superposition of many such waves of different frequency and amplitude. Therefore, sea states are often described by either a discrete spectrum, S_i,

$$S_i = \frac{A_i^2}{2\Delta f} \tag{1.2}$$

where A_i is the amplitude of the i^{th} frequency component (ω_i) and Δf is the frequency interval,

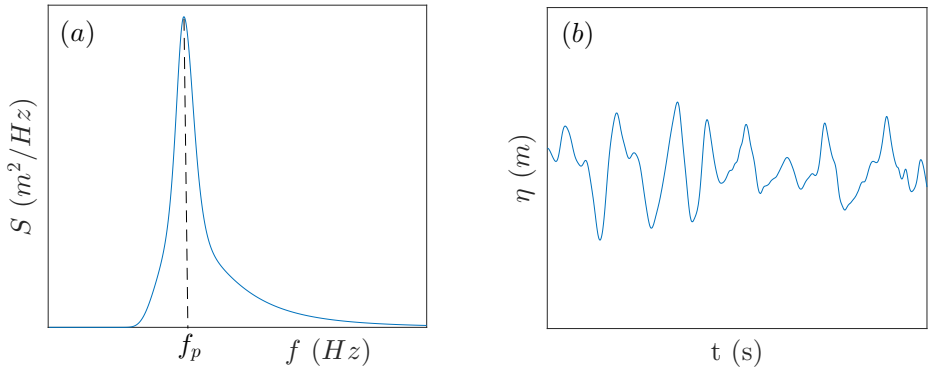

Figure 1.3: (a) A qualitative JONSWAP energy density spectrum. (b) a time series of irregular waves from a JONSWAP spectrum.

or a continuous energy density spectrum S. Typically, S can be described by certain characteristics, including a dominant frequency (f_p), the width of the peak (narrow or wide), and parameters such as the peak enhancement factor that influences the height of the peak. One commonly used description of wave spectra is the JONSWAP (JOint North Sea WAve Project; Hasselmann et al. 1973) spectrum (Fig. 1.3 (a)), given by,

$$S(\omega) = \frac{\alpha g^2}{\omega^5} \exp\left[-\frac{5}{4}\left(\frac{\omega_p}{\omega}\right)^4\right] \gamma^r, \tag{1.3}$$

with $r = \exp\left[-\frac{(\omega-\omega_p)^2}{2\sigma^2\omega_p^2}\right]$, where α is σ are non-dimensional parameters, γ is a peak enhancement factor, g is the acceleration due to gravity, and ω_p is a peak frequency. The individual wave properties of the i^{th} component, A_i, ω_i, and k_i are then determined from these spectra based on the desired frequency interval and superposed to get the free surface elevation as,

$$\eta(x,t) = \sum_i^N A_i \cos(k_i x - \omega_i t + \varphi_i) \tag{1.4}$$

with φ_i, the phase angle can either be random or a prescribed value. An example of such a free surface as a function of time is shown in Fig. 1.3 (b).

To illustrate nonlinear effects (i.e., when ϵ is finite), several perturbation approaches (assuming the solution depends on the small quantity, ϵ), were developed, e.g., Stokes waves (Stokes 1847). The 2^{nd} order free surface elevation for regular waves is given by,

$$\eta(x,t) = A\left\{\cos\,\theta + kA\,\frac{3-\sigma^2}{4\,\sigma^3}\,\cos\,2\theta\right\} + \mathcal{O}\left((kA)^3\right) \tag{1.5}$$

with $\sigma = \tanh\, kd$. This expansion, however, is non-converging in very shallow conditions. Alternate approximate theories in shallow water for solitary (Boussinesq 1872) and cnoidal waves (Korteweg & De Vries 1895) were developed, which were generalized in Dingemans 1997 as the

approximate solution for wave elevation,

$$\eta(x,t) = \eta_2 + H\ \mathrm{cn}^2\left(\ 2\,K(m)\,\frac{x - c\,t}{\lambda}\ \right) \tag{1.6}$$

where H is the wave height, λ is the wavelength, c is the phase speed, η_2 is the trough elevation, cn is one of the Jacobi elliptic functions, and $K(m)$ is the complete elliptic integral of the first kind with parameter m (for more details refer to Dean & Dalrymple 1991). The parameter $m = 0$ gives a sinusoid, m between 0 and 1 gives a cnoidal wave and at the limit, $m = 1$ gives a solitary wave. Cnoidal waves have sharp and steep crests with flat and wide troughs relative to sinusoidal waves that have symmetric crests and troughs. At the limit of infinite wavelength, a cnoidal wave becomes a solitary wave.

With the advent of computers, numerical modeling became a practical tool for understanding and studying fluid flow problems. Among the early uses was in calculating stream function waves, obtained by solving a potential flow problem in constant depth such that the stream function vector field, $\psi(x,z)$ satisfies $\partial_x\psi = -w$ and $\partial_z\psi = u$, where (u,w) are the horizontal and vertical velocities, respectively (Dean 1965), which could also be applied for cases with a steady current. With the advances in computational powers and modern numerical methods, complex phenomenons such as wave overturning were simulated (Longuet-Higgins & Cokelet 1976). Another big step was in simulating wave propagation over a slope followed by runup (e.g., Kennedy et al. 2000). This was done in models that limit the degrees of wave non-linearity (ϵ) and dispersion (μ). For example, in shallow water, where nonlinearity and bottom effects dominate, and dispersive effects are insignificant, models based on the Nonlinear Shallow Water equations, which assume a uniform velocity over depth were derived (Stelling & Zijlema 2003). In intermediate water depth, where both non-linearity and dispersion are important, Boussinesq-type models are used (Kirby 2016, Nwogu 1996).

One of the most significant developments from Euler formulations (irrotational and inviscid) of the fluid flow is the Fully Nonlinear Potential Flow model (FNPF), which is derived either from Zakharov 1968 or Longuet-Higgins & Cokelet 1976 (e.g., Dold & Peregrine 1985; West et al. 1987; Grilli et al. 1989; Newman & Lee 2002; Ducrozet et al. 2007; Fochesato et al. 2007; Bingham & Zhang 2007; Belibassakis & Athanassoulis 2011; Nimmala et al. 2013; Yates & Benoit 2015; Ducrozet et al. 2017). These models do not make any assumptions on nonlinearity or dispersion, taking into account variable bathymetry, and are valid up to the breaking onset (a detailed summary of FNPF models is given in Chapter 2).

Finally, there are Navier-Stokes models (e.g., two-fluid models such as Guignard et al. 2001; Abadie et al. 2010; Derakhti et al. 2016; and LES such as Harris & Grilli 2014) that can simulate the complete physics. However, the computational time required to apply Navier-Stokes models restricts their use to small domains and short temporal scales.

1.3 FNPF models

This thesis makes use of two FNPF models that have been developed and/or utilized at the Laboratoire d'Hydraulique Saint-Venant (LHSV) in the past decade. A brief overview of their development and applications at LHSV is presented in the following subsections (a description of these models is provided in Chapter 2).

1.3.1 Misthyc

Based on Zakharov 1968 and the spectral approach of Tian & Sato 2008, the Misthyc model in 2D was developed by Yates & Benoit 2012 and Benoit et al. 2013. Yates & Benoit 2015 studied the convergence properties, model propagation errors, and CPU time to find optimal numerical model parameters (CFL number and resolution in the vertical). This model was later extended to 3D with an unstructured discretization (scattered nodes) in the horizontal plane with the horizontal derivatives estimated using the RBF-FD (Radial Basis Function - Finite Difference) method in Raoult 2016. A new version of the 3D Misthyc model called Whispers-3D is utilized in studying wave bottom interactions (Zhang & Benoit 2021) and in comparing wave breaking modeling with several other models of low to high computational complexity (Benoit et al. 2023). In this study, only the 2D Misthyc model is used.

1.3.2 NWT

The Boundary Element Method NWT was developed in 2D in Grilli et al. 1989, and 3D in Grilli et al. 2001, based on the approach of Longuet-Higgins & Cokelet 1976. The 3D model was used in the works of Guerber 2011 and was later extended to solve large-scale wave-structure interaction problems for surface-piercing bodies, for engineering applications, by reformulating the NWT to use cubic B-splines and accelerating the BEM solution with a parallelized Fast Multipole Method (FMM) based on ExaFMM at LHSV by Kuznetsov et al. 2018 and Harris et al. 2022. Applications of this model for wave structure interactions are shown in Harris et al. 2016, Dombre 2015, and Dombre et al. 2019. Landesman 2022 coupled the NWT to a Volume Of Fluid (VOF) model with the NWT limited to non-breaking waves. In this study, the 2D model of Grilli et al. 1989 and the 3D model of Harris et al. 2022 are used.

1.4 The physics of wave breaking

Wave breaking is a phenomenon of large interest as it is responsible for the transfer of energy from the atmosphere through waves to the ocean surface, it helps exchange gases from the atmosphere and the large force of breaking wave impacts is important to consider for the safety of offshore structures. This dissipative phenomenon is observed when wave crests become unstable thus transforming to turbulent kinetic energy. Based on driving physics, long-crested breaking waves have been broadly classified into depth-limited (manifested by shoaling) and steepness-

limited (manifested by focusing energy at a particular point). The waves breaking over a slope are also classified into three types. The first type is known as spilling, which occurs over a gentle slope. In spilling breakers, the waves are observed as white foam spilling down the front face of the wave. The second type is plunging breakers, which occur over a steeper slope. In plunging breakers, the waves form a distinctive jet that overturns on the front face of the wave. The third type is surging breakers, which occur over a very steep slope. Surging breakers are characterized by the waves surging forward and breaking forcefully on a steep slope, and this kind of breaking typically occurs directly at the waterline (Fig. 1.4). These are quantitatively also classified by the Iribarren number,

$$\xi_0 = \frac{\tan\ \alpha}{\sqrt{H_0/L_0}} \tag{1.7}$$

where α is the beach slope, H_0 is the offshore wave height and L_0 is the deep-water wavelength. The breaker types are classified as spilling for $\xi_0 < 0.5$, plunging for $0.5 < \xi_0 < 3.3$ and surging for $\xi_0 > 3.3$ (Battjes 1974).

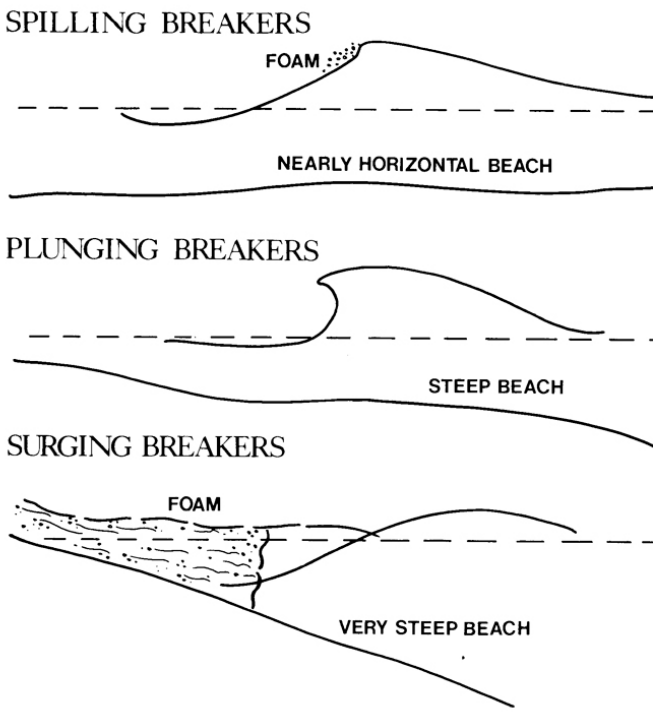

Figure 1.4: Types of breaking waves over a slope (source: Hayes 1985).

Early attempts were made by Stokes 1880 to propose a theoretical limit for wave steepness by considering that waves break if the particle velocity at the crest exceeds the phase speed. In terms of the geometric parameters, this corresponded to waves with the angle between two lines tangent to the surface profile at the wave crest of 120° (Fig. 1.5). In deep water, Michell 1893 found that in deep water, this criterion corresponds to a wave steepness of $kA = 0.44$. In shallow water, McCowan 1894 formulated the breaking wave height, $H_b = 0.78 d_b$ where d_b denotes the depth at breaking. Consistent with this, more general shallow water results have had bounds for the

ratio of wave height to water depth ($\kappa = H/d$) observed to be in $[0.7,\ 1.2]$ (Battjes 1974, Dean & Dalrymple 1991, Mei 1989). Others have considered vertical acceleration as a breaking criterion, for example, Taylor 1953 show both theoretically and experimentally that a standing wave of maximum amplitude has the vertical acceleration at the crest equal to $-g$.

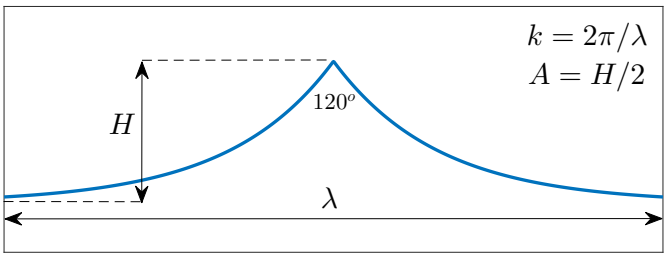

Figure 1.5: Limiting Stokes wave in deep water.

Over the past half a century, researchers have been working to understand this phenomenon (e.g., Svendsen et al. 1978; Stive 1984; Phillips 1985) and to predict its behavior (i.e., the loads exerted, wave height decay, probability of occurrence, etc.) from experimental observations as well as higher-fidelity wave model simulations.

1.4.1 Experimental interpretation

Experimental interpretations are derived from either field studies conducted in natural environments or laboratory experiments conducted in controlled test facilities. In field studies, a specific region of interest is selected in which several instruments are deployed to collect data, for example, sensors to record wave elevations. Laboratory studies are generally carried out in a wave flume (for 2D effects) or a wave tank (for 3D effects). An example laboratory wave flume is shown in Fig. 1.6. The setup includes a flap-type wavemaker designed to generate waves. Flap-type wavemakers are commonly employed for generating deep to intermediate water waves, as the motion of the flap closely mimics that of fluid particles. In contrast, piston-type wavemakers are typically used for generating shallow water waves, as the motion of the piston better resembles the behavior of fluid particles in such conditions. The wave flume here has a constant depth bottom but can have any desired bathymetry.

With several theoretical predictions of wave heights at the breaking onset, researchers then attempted to predict the evolution of wave heights caused by wave breaking. In the surf zone with mild slopes where breaking waves are generated by shoaling due to a decrease in water depth, Svendsen et al. 1978 suggested that in the inner breaking region i.e., the region extending from the location of breaking onset up to where the run-up starts, resembles a moving bore or a hydraulic jump, whose characteristics are locally controlled by the depth and bed slope. They compared the energy dissipated by a mild spilling breaking wave from the experiments in a wave flume with a $1/34.25$ bottom slope to a wave height decay model formulated from the conservation of energy principle, with the magnitude of the dissipation rate of an equivalent hydraulic jump.

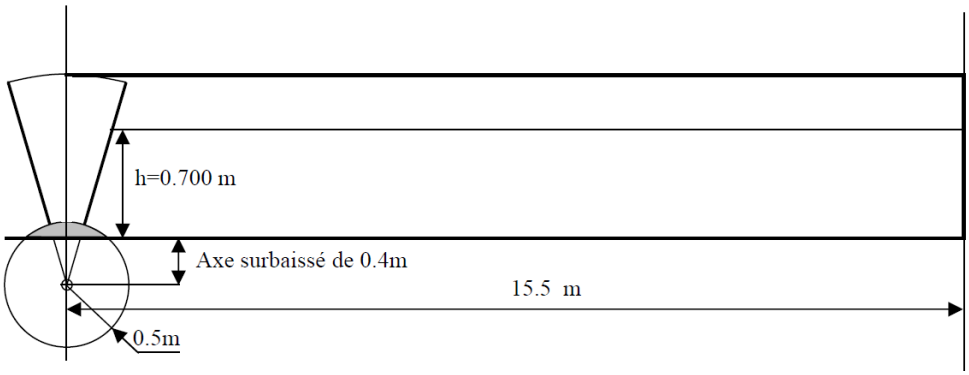

Figure 1.6: The wave flume at Ecole Centrale Marseille, with a flat bottom and flap-type wavemaker. Source: Lili Kimmoun

They found the ratio of energy dissipation from the breaking wave and that of the hydraulic jump to be between 1.4 to 1.6 for the bed slope of $1/34.25$. Stive 1984 later obtained a similar ratio for a few different bed slopes (ranging from $1/20$ to $1/80$). Basco & Svendsen 1984 made an attempt to develop a semi-empirical distribution for surf zone energy dissipation by introducing a momentum flux correction coefficient α.

In deep water, several studies have been done to understand the onset of breaking waves, or in other words, the probability of occurrence of breaking waves, given the wave conditions. Phillips 1985 proposed a distribution $\Lambda(c)$, the length of breaking fronts with velocities in the range $(c,\ c+dc)$ per unit surface area, such that its first moment, $\int c\Lambda(c)dc$, gives the number of breaking waves passing a given point and the fifth moment, $\int c^5\Lambda(c)dc$, is related to the energy lost due to wave breaking. Romero et al. 2012 extended this approach to establish a semi-empirical relation for the spectral dependence of the energy dissipation to propose a model for the spectral dependence of the breaking strength parameter (b, defined such that the total wave breaking energy dissipated, $\epsilon = b\rho c^5/g$). Rapp & Melville 1990 carried out deep-water wave breaking experiments to further understand its kinematics and energy dissipation by showing the quantitative importance of the breaking process in wave modeling, in mixing, and in transferring horizontal momentum. Banner & Peregrine 1993 explain the various field measurements that can be carried out to capture breaking waves in deep water. In recent years, a unified criterion to distinguish breaking from non-breaking crests was proposed by looking at the ratio of horizontal crest velocity to phase speed, $B = u/c$ of a crest. When B exceeds a certain threshold, waves will ultimately break. Due to the difference in scaling, several threshold ratios have been suggested (e.g., Grue & Jensen 2012, $B = 0.45$; Barthelemy et al. 2018, $B = 0.85$). A few exceptions to the threshold given by Barthelemy et al. 2018 are reported in Hasan et al. 2019 (the existence of non-breaking crests at intermediate depth with $B \in [0.9 - 0.92]$), and Scolan & Etienne 2023 (the existence of non-breaking crests for a focused intermediate depth breaker and for a dam breaking flow leading to soliton with $B \in [0.9 - 1]$).

Duncan 1981 and Duncan 1983 conducted a series of experiments of steady breaking waves induced by fully submerged towed 2D symmetric hydrofoils, and quantified for these cases, the

non-dimensional breaking strength parameter, b. Cointe 1987 derived a mathematical model from these steady spilling breaker observations, and then also extended it to account for unsteady effects. Banner & Peirson 2007 determined this breaking strength for deep-water breaking waves to be strongly correlated to a growth rate parameter at the onset ($1/\omega_c \; D(Ek^2)/Dt$, where ω_c is the initial mean carrier wave frequency and Ek^2, a non-dimensional variable reflecting the depth-integrated local total energy density (E) and local wavenumber (k) behavior). This work of parameterization motivated several researchers (e.g., Derakhti, Banner & Kirby 2018; Mostert & Deike 2020) to determine this breaking strength with respect to other wave parameters that could be calculated from the input waves or at the onset of breaking, specifically from Navier-Stokes models.

1.4.2 Higher-fidelity model interpretation

In recent years, several studies have been done to understand breaking waves through higher-fidelity models (e.g., Navier-Stokes LES; DNS), and possibly relate the initiation of breaking and the magnitude of energy dissipated to local quantities of the input wave or at the onset, a subject of great interest for simplified numerical models. Iafrati 2009 looked at the role of breaking intensity on free surface dynamics, air entrainment, energy dissipation, the vertical transfer of momentum, and vorticity. Iafrati 2011 reported the evolution of instantaneous energy dissipation and breaking strength from spilling and plunging breaking. Derakhti, Banner & Kirby 2018 provided an empirical prediction of the breaking strength (b) for deep and intermediate breaking waves by looking at the time rate of change of the ratio of horizontal speed to phase speed at the onset. Mostert & Deike 2020 related energy dissipation from breaking to the local wave height, depth, and beach slope for shoaling and breaking solitary waves on beaches.

1.5 Parameterized wave breaking modeling

With the existing knowledge of breaking waves, several attempts have been made to implement their effects in numerically simplified models that are unable to model breaking waves explicitly, due to the assumptions made in deriving them (e.g., Guignard & Grilli 2001; Kennedy et al. 2000; Papoutsellis et al. 2019; Simon et al. 2019). A parameterized wave breaking model is composed of three steps. First, the onset, or the instant in time at which waves break, is identified, then the amount of energy to be dissipated is estimated, and finally, a termination criterion to cease this dissipation.

Wave breaking onset parameters are classified as geometric, relating to the shape of the wave; kinematic, relating to the velocity at the crests; and dynamic, relating to the energy at the crest. A geometric criterion, wave crest front slope threshold was first used by Schäffer et al. 1993 and later Guignard & Grilli 2001, which was calibrated for weak spilling breakers. Among kinematic criteria, a threshold for the time rate of change of free surface elevation was used in Kennedy et al. 2000; Papoutsellis et al. 2019; and Simon et al. 2019, who calibrated it to specific cases. In recent years, a unified onset criterion was introduced by Barthelemy et al. 2018 for deep water

and then Derakhti et al. 2020 for all relative depths, a threshold in the ratio of the horizontal velocity of a particle to phase speed of a crest, thus not requiring to calibrate it for individual cases. Among the dynamic criterion is the wave Froude number threshold from Okamoto & Basco 2006 separating breaking and non-breaking regimes. The onset parameter is often used at a lower threshold as a termination criterion which must be calibrated for individual test cases, due to insufficient knowledge. A comparison of different onset and termination criteria is done in Simon et al. 2019, which shows various optimal calibration parameters with respect to a few dissipation models and onset criteria for a few test cases.

To model breaking dissipation, Nwogu 1996 extended their Boussinesq model to include the effects of wave breaking in the surf zone by coupling the mass and momentum equations with a one-equation model for the temporal and spatial evolution of the turbulent kinetic energy. Tonelli & Petti 2009 formulated a hybrid method consisting of suppressing the dispersive terms in breaking regions and treating breaking waves as shocks by switching from Boussinesq formulation to a nonlinear shallow water equation. This model is compared with the one from Nwogu 1996 in Kazolea & Ricchiuto 2018. Tian et al. 2010, 2012 describe an eddy viscosity model, parameterized in the kinematic and the dynamic free surface boundary conditions, for deep water breaking, with the magnitude of the eddy viscosity dependent on the wave height, wavelength, and wave period defined at breaking onset. This model is also later used in the high-order spectral model of Seiffert & Ducrozet 2018. Viviano et al. 2015 extended their Boussinesq-type model to include the effects of vorticity due to wave breaking for spilling breakers by assuming an analogy between these breakers and hydraulic jumps.

A brief review of reduced-form dissipation models applied to nonlinear Schrodinger equations in deep water is done in Liu et al. 2023, suggesting the addition of a global kinematic breaking onset criterion instead of turning on dissipation when the wave group narrows and possible extensions of spectral dissipation in irregular seas.

Kennedy et al. 2000 demonstrated the use of an eddy viscosity model in which the dissipation term due to wave breaking is added to the momentum equations of their Boussinesq model, based on the tangential velocity at the free surface. This dissipation term is modeled as a damping pressure added to the dynamic free surface boundary condition in Papoutsellis et al. 2019 and Simon et al. 2019 as,

$$\partial_x P = \frac{1}{d+\eta}\partial_x F \tag{1.8}$$

where P is damping pressure divided by density, with $F = -\Delta(d+\eta)(\partial_t \eta)^2$, d is the water depth, η is the free surface elevation, $\Delta = \delta^2 B$ with δ controlling the magnitude of dissipation, which they determined by numerical tests as equal to 1.2 and B is a smooth function varying from 0 to 1 in time and space to prevent instabilities. The suffixes denote the respective derivative. A comparison of the dissipation models based on a hydraulic jump damping pressure and an eddy viscosity model is done in Papoutsellis et al. 2019 and Simon et al. 2019 concluding that the hydraulic jump analogy works better for spilling breakers and the eddy viscosity model for plunging breakers.

Due to the lack of a more general understanding of spilling and plunging breakers, and the dif-

ferences in the physical breaking processes/mechanism, these two types of wave breaking are often treated separately. The magnitude of energy dissipated from mild spilling breakers is sometimes taken to be proportional to that of an equivalent hydraulic jump, with the proportionality constant determined from experimental observations (Svendsen et al. 1978). This energy can be modeled as an absorbing pressure on the free surface around the breaking crest, such that this pressure times the normal velocity integrated over the breaking region gives the instantaneous power to be dissipated (Guignard & Grilli 2001; Papoutsellis et al. 2019; Simon et al. 2019), with the breaking region centered around a crest.

1.6 Manuscript Overview

Chapter 2 discusses the 2D unified depth-limited wave breaking detection and dissipation model developed during the thesis. This model is then validated with several regular and irregular cases. This chapter is an article published in Coastal Engineering: Mohanlal et al. 2023.

Chapter 3 discusses the 2D steepness-limited wave breaking dissipation model. This model is used to validate focused breaking tests conducted by Lili Kimmoun at Ecole Centrale Marseille (ECM) and was presented at the 37^{th} International Conference on Coastal Engineering.

Chapter 4 discusses the 3D wave breaking model developed during the thesis. This model is an extension of the 2D depth-limited dissipation model presented in Chapter 2. It is described and validated with several regular breaking experiments. This work was presented at two conferences, the 38th International Workshop on Water Waves and Floating Bodies and the 5th B'WAVES workshop, and is currently being prepared to be submitted as a journal article.

Chapter 5 summarises the main findings of this thesis, the applicability of the proposed models, their limitations, and perspectives for future work.

Finally, the appendices include all the abstracts submitted to conferences during this thesis and the test matrix of the focused breaking waves conducted by Lili Kimmoun at ECM.

Chapter 2

Unified depth-limited wave breaking model

by S. Mohanlal, J. Harris, M. Yates, and S. Grilli
Coastal Engineering 183:104316, 2023
DOI: 10.1016/j.coastaleng.2023.104316

Une nouvelle méthode est proposée pour simuler la dissipation d'énergie résultant d'un déferlement de vague en profondeur limitée, en combinaison avec un critère de début de déferlement universel, dans des modèles bidimensionnels (2D) d'écoulement potentiel non linéaire (FNPF). La méthode introduit un paramètre non dimensionnel d'intensité du déferlement. Deux modèles 2D-FNPF différents sont utilisés, qui résolvent l'équation de Laplace, l'un par développements polynomiaux de Chebyshev, l'autre par une méthode d'élément de frontière. Dans ces modèles, l'imminence du déferlement est détecté en temps réel à l'aide d'un critère universel de début de déferlement proposé dans des travaux antérieurs, basé sur le rapport de la vitesse horizontale des particules à la crête u, par rapport à la vitesse de crête c, $B = u/c > 0.85$. Pour ces vagues, l'énergie est dissipée localement par l'introduction d'une pression de surface absorbante qui est calibrée par analogie à un ressaut hydraulique inversé. Cette approche est d'abord validée pour des vagues périodiques qui deviennent des déferlantes glissantes sur des plages à pente constante et des barres, pour lesquels les résultats s'avèrent en bon accord avec les données expérimentales. En reformulant ce modèle de dissipation du déferlement en termes d'intensité du déferlement non-dimensionnelle, l'analogue avec un ressaut hydraulique fournit des résultats similaires à ceux d'un modèle d'intensité du déferlement constante et donne également un bon accord pour des vagues périodiques qui deviennent des déferlantes plongeantes. La même approche est ensuite appliquée aux vagues irrégulières propageant sur une barre submergée, et s'avère en bon accord avec les données expérimentales pour la hauteur des vagues, l'asymétrie et le kurtosis. Les travaux futurs étendront ce modèle de déferlement 2D aux cas de vagues déferlantes tridimensionnelles (3D), simulées dans des modèles 3D-FNPF existants, dans des conditions d'eau peu profonde ou profonde.

Abstract

A new method is proposed for simulating the energy dissipation resulting from depth-limited wave breaking, in combination with a universal breaking onset criterion, in two-dimensional (2D) fully nonlinear potential flow (FNPF) models, based on a non-dimensional breaking strength parameter. Two different 2D-FNPF models are used, which solve the Laplace equation based on Chebyshev polynomial expansions or a boundary element method. In these models, impending breaking waves are detected in real time using a universal breaking onset criterion proposed in earlier work, based on the ratio of the horizontal particle velocity at the crest u, relative to the crest velocity c, $B = u/c > 0.85$. For these waves, wave energy is dissipated locally with an absorbing surface pressure that is calibrated using an inverted hydraulic jump analogy. This approach is first validated for periodic spilling breakers over plane beaches and bars, for which results are shown to be in good agreement with experimental data. Recasting this breaking dissipation model in terms of a non-dimensional breaking strength, the hydraulic jump analog is shown to provide results similar to those of a constant breaking strength model, and to yield good agreement for periodic plunging breakers as well. The same approach is then applied to irregular waves shoaling over a submerged bar, and is shown to agree well with experimental data for the wave height, asymmetry, skewness, and kurtosis. Future work will extend this 2D breaker model to cases of three-dimensional (3D) breaking waves, simulated in existing 3D-FNPF models, in shallow or deep water conditions.

2.1 Introduction

Once generated by wind, ocean waves evolve with complex kinematics and dynamics, as a result of nonlinear and dispersive effects, bathymetric variability, and dissipation from wave breaking and bottom friction, to name a few. Accurate simulations of this evolution are crucial for predicting phase-resolved surface wave properties in complex sea states, which govern wave interactions with fixed and floating objects, including offshore renewable energy systems, and surf zone parameters that drive nearshore currents and sediment processes, whose understanding and prediction are key to coastal management decisions.

Wave processes in complex sea states have already been simulated to some extent, based on equations representing the complete physics (i.e., derived from Navier-Stokes equations for single or multiple fluids). However, such simulations are highly computationally intensive and, hence, limited to small spatial and temporal scales. In contrast, operational models have been developed based on equations that simplify the wave physics, but nevertheless can simulate realistically many ocean wave processes over large areas and for long time periods. In such models, which are usually restricted to a specific wave regime (e.g., shallow or deep water conditions, small amplitude waves), important processes missing from the equations are parameterized in an ad-hoc manner, often on the basis of semi-empirical terms (e.g., breaking or bottom friction dissipation, the presence of structures). In this category are the standard phase-averaged wind wave models that are based on a spectral representation of the wave energy as a function of frequency and

direction (e.g., STWAVE, Smith et al. 2001; TOMAWAC, Benoit et al. 1997; WAVEWATCH III, Tolman 2009).

However, in many engineering applications, phase-resolved wave properties are required in real time. Thus, there is a need for models in which the wave elevation and kinematics are predicted over space and time, and in which the complex physics resulting from wave nonlinearity and fluid interactions with structures and the seafloor can be accurately represented. Examples of problems requiring the use of such models include ship or ocean energy system seakeeping and motion control/optimization, coastal wave runup, and the prediction of extreme wave loads on ocean structures.

Phase-resolved models take many forms, depending on their domain of application. Ocean waves are often classified by the the depth d to wavelength L ratio. In deep water, for $d \gtrsim L/2$, where nonlinearity is usually weak but dispersive effects are important, one might apply models based on the linear mild-slope equation (MSE), such as REFDIF (Kirby & Dalrymple 1983). In shallow water, for $d \lesssim L/20$, where nonlinearity and bottom effects dominate, and dispersive effects become less significant, models based on the Nonlinear Shallow Water (NSW) equations, which assume a uniform velocity over depth, could be an optimal choice (e.g., Stelling & Zijlema 2003; Zijlema & Stelling 2008). Lastly, in intermediate water depth, where both wave nonlinearity and dispersion are important, Boussinesq-type models (Kirby 2016) that feature both nonlinearity and dispersion to some extent, based on specifying a cutoff on higher-order terms representing these processes, are preferred provided that the horizontal velocity varies only moderately with depth such that it can be described by a polynomial approximation (e.g., Madsen & Schäffer 1998; Agnon et al. 1999; Madsen et al. 2002; Kennedy et al. 2000) and fully nonlinear Serre-Green-Naghdi-type models (e.g., Wei et al. 1995; Cienfuegos et al. 2006; Bonneton, Chazel, Lannes, Marche & Tissier 2011; Shi et al. 2012; and Zhao et al. 2014). Boussinesq-type models are typically developed based on a perturbation expansion of the Fully Nonlinear Potential flow (FNPF) equations (Kirby 2016), with wave breaking, bottom friction, and horizontal vorticity effects represented by terms added to the equations to parameterize these physical processes (Kazolea & Ricchiuto 2018, Kennedy et al. 2000, Shi et al. 2012). These models have proved accurate in simulating laboratory experiments in which waves are generated in deep to intermediate water conditions and propagate into shallow water.

Models that directly solve the FNPF equations (e.g., Dold & Peregrine 1985; Dommermuth & Yue 1987; Grilli et al. 1989, Grilli & Subramanya 1996; Grilli et al. 2001; Bingham & Zhang 2007; Belibassakis & Athanassoulis 2011; Yates & Benoit 2015; Ducrozet et al. 2017) are more computationally demanding than MSE, NSW, or Boussinesq-type models, but can accurately simulate waves in all water depth regimes up to wave breaking, since no assumptions are made about the wave nonlinearity or dispersion. FNPF models assume the flow is irrotational and, hence, are governed by Laplace's equation for the velocity potential, which makes them more computationally efficient than full Navier-Stokes (NS) models. Among FNPF models, those based on the Higher-order Spectral (HOS) method (Dommermuth & Yue 1987) are notably very efficient, but can typically only be applied to waves propagating in constant depth and up to a certain wave height, unless a modified form of the models is used, which makes them less efficient (Ducrozet et al. 2017).

FNPF models (except HOS-based models that require spatial periodicity) can also simulate wave interactions with structures and wave shoaling over an arbitrary bathymetry (e.g., slopes and/or bars), up to and into breaking/overturning (e.g., Grilli et al. 2004, Grilli, Subramanya, Svendsen & Veeramony 1994, Grilli, Losada & Martin 1994, Grilli et al. 1997, 1998; Grilli & Horrillo 1999; Guyenne & Grilli 2006; Fochesato et al. 2007; Pomeau et al. 2008). However, FNPF models become unstable when waves begin to break and overturn, unless this process can be prevented by artificially specifying the dissipation of wave energy caused by breaking (e.g., Guignard & Grilli 2001; Grilli, Horrillo & Guignard 2020 for a review).

As noted before, many NS models of wave breaking have been developed, using various numerical schemes and methods, including two-fluid models that represent the air and water (e.g., Guignard et al. 2001; Lachaume et al. 2003; Abadie et al. 2010; Banari et al. 2014; Derakhti et al. 2016), which can accurately simulate wave breaking either in direct NS simulations or based on standard turbulence models such as Large Eddy Simulation (LES; e.g., Harris & Grilli 2014). However, the spatial resolution (and hence computational time) required to apply NS models currently restricts their use to small spatial and temporal scales and thus often to academic or idealized problems. Therefore, considering the large range of engineering applications involving strongly nonlinear and breaking waves, it is highly desirable to extend FNPF models to adequately model breaking waves and their related energy dissipation.

Earlier work has simulated the energy dissipation resulting from breaking waves in FNPF models (e.g., Grilli, Horrillo & Guignard 2020, Guignard & Grilli 2001, Papoutsellis et al. 2019, Seiffert & Ducrozet 2018, Seiffert et al. 2017, Simon et al. 2019), but here a more general and accurate way of both detecting breaking onset in any conditions (i.e., wave types, bathymetry, and breaker types), including for nonlinear irregular wave trains, and simulating the corresponding energy dissipation in a more realistic manner are proposed. The present paper only describes two-dimensional (2D) models featuring 2D breaking waves, and the extension to three-dimensions (3D) will be presented in future work.

FNPF models use fully nonlinear kinematic and dynamic boundary conditions that are typically derived based on the formulations of Zakharov (1968) or Longuet-Higgins & Cokelet (1976). With the Eulerian framework of Zakharov (1968), the free surface elevation is assumed single-valued, and thus waves can be modeled only until the instant that the free surface becomes vertical (e.g., Dommermuth & Yue 1987; Craig & Sulem 1993, Bingham & Zhang 2007; Yates & Benoit 2015, Belibassakis & Athanassoulis 2011). In models that follow the Eulerian-Lagrangian framework of Longuet-Higgins & Cokelet (1976), the free surface can be multivalued (e.g., for plunging breakers) and hence accurately simulated (in comparison to experiments) until the breaker jet impacts the free surface (e.g., in 2D, Dold & Peregrine 1985; Grilli et al. 2004, 1989, Grilli & Subramanya 1996, Grilli et al. 1997, 1998; or, in 3D, Guyenne & Grilli 2006; Fochesato et al. 2007).

In the present study, two 2D-FNPF models are modified and used to demonstrate the application of a novel combination of breaking onset/termination criteria and a breaker model: (i) an Eulerian model based on a finite difference approach, Misthyc (Yates & Benoit 2015), and (ii) an Eulerian-Lagrangian model based on a boundary element approach, first proposed by Grilli et al. (1989),

hereafter referred to as the "numerical wave tank" (NWT). Although the latter model can simulate all the cases presented here, some wave propagation cases can be simulated more efficiently by one of the models. For instance, Misthyc, similar to other models of this type (e.g., Dommermuth & Yue 1987; Bingham & Zhang 2007; Engsig-Karup et al. 2009; Ducrozet et al. 2017) that only apply to single-valued free surfaces, may be faster for larger domain sizes. In contrast, the higher-order Boundary Element Method (BEM) used in the NWT can simulate the exact geometry of a moving wavemaker, or complex bottom geometries, as well as multivalued free surfaces. Both types of models are equally able to simulate accurately highly nonlinear and dispersive waves propagating over arbitrary bathymetries. In both models, when waves are detected to approach breaking, an energy dissipation is explicitly specified to prevent wave breaking (e.g., instability or overturning) from occurring, which would interrupt the simulations. This is done by first identifying where and when in the computational domain impending breaking waves occur, using a *breaking onset criterion*, then applying a *physically realistic energy dissipation* onto these waves, commensurate with their parameters, and finally defining where and when this dissipation should cease to be applied, using a *breaking termination criterion*.

Wave breaking onset (or impending breaking) refers to the location in space and moment in time where and when some properties of an individual wave reach values indicating that the wave will soon begin to break and dissipate some of its energy through turbulence and viscosity. In a NS model of breaking waves, this process is included in the model equations and typically occurs automatically in the simulations. In models with reduced physics, such as FNPF, explicit breaking criteria must be defined to detect impending wave breaking. Wave breaking criteria usually depend on local wave properties such as the crest kinematics, steepness, surface slope, or curvature reaching a specified threshold value. Since the physics of wave breaking varies from deep to shallow water, until recently, different breaking criteria have been proposed to simulate different wave breaking regimes. In deep water, wave breaking is usually attributed to exceeding a critical wave steepness, and is referred to as steepness-limited breaking. In shallow water, wave breaking is usually induced by bathymetric effects, occurring during the shoaling process as waves propagate into shallow water, and is referred to as depth-limited breaking. In the latter case, the type of wave breaking (e.g. spilling or plunging) and the energy dissipation intensity depend on the incident wave train and wave shoaling process (e.g. bottom slope). Spilling breaking generally occurs over mild slopes, plunging breaking over steeper slopes, and surging breaking over very steep slopes (see, e.g., Grilli et al. 1997 for solitary wave shoaling). Accordingly, many different definitions and criteria have been proposed for estimating breaking onset, and they can be broadly classified (Derakhti et al. 2020) as geometric (e.g., Schäffer et al. 1993), kinematic (e.g., Wei et al. 1995; Kurnia & van Groesen 2014), or dynamic (e.g., Barthelemy et al. 2018) criteria. For depth-limited breaking, the geometric and kinematic criteria are often used (Grilli, Horrillo & Guignard 2020, Grilli et al. 1997, Papoutsellis et al. 2019, Simon et al. 2019), but they require an empirical constant that is case-specific and depends on the bathymetry and incident wave conditions. Barthelemy et al. (2018) and Derakhti et al. (2020) recently showed that there appears to be a universal breaking onset criterion for an evolving crest in the form of the ratio of the horizontal particle velocity at the crest to the wave (or crest) celerity, $B = u/c$ reaching a threshold

value $B_{th} = 0.85$. This criterion indicates that, when the wave crest reaches this B_{th} value, the wave will inevitably evolve towards breaking, although it does not necessarily start breaking at the threshold. Seiffert et al. (2017) and Seiffert & Ducrozet (2018) recently used this criterion in a HOS model, coupled with an energy dissipation model based on an eddy viscosity, and they demonstrated the accuracy of this criterion for focused wave trains breaking over a flat bottom in intermediate water depths with comparisons to laboratory experiments. This breaking onset criterion based on B is used in the present work.

Energy dissipation resulting from wave breaking is complex and not yet fully understood, thus simulating it in reduced-physics models, including those based on FNPF, has often relied on analogies with well-known dissipative phenomena, such as a hydraulic jump (HJ; e.g., Guignard & Grilli 2001). For example, a weak spilling breaker dissipates energy as white water rolls on the front face of the wave and, by moving in a frame of reference at the wave speed, this process resembles a bore or a HJ. Svendsen et al. (1978) and Stive (1984) compared the energy dissipated by a spilling breaker with that of a bore and estimated an empirical constant, $\mu \simeq 1.5$, quantifying the ratio of energy dissipated by the breaking wave to that of an equivalent HJ. This analogy has been successfully used to simulate spilling breaking wave dissipation in FNPF models (Grilli, Horrillo & Guignard 2020, Papoutsellis et al. 2019, Simon et al. 2019); it will also be applied in the present work. Although the HJ analog approach should be less accurate for plunging breakers, because breaking is more violent and the overturning surface no longer resembles a hydraulic jump, it appears adequate in most cases. However, to simulate long-term irregular sea states, where both spilling and plunging wave breaking occurs, it is necessary to develop a breaker model that does not rely on test case dependent empirical constants.

Over the past few decades, many advances have been made in parameterizing wave breaking dissipation. Duncan (1983) conducted a series of experiments on steady breaking waves induced by fully submerged towed 2D hydrofoils, and quantified for these cases the non-dimensional breaking strength parameter b (the wave breaking energy normalized by the fifth power of the wave celerity). Similarly, Phillips (1985), formulated spectral breaking strength as a function of wave speed using b in deep water for irregular wind-generated waves in the ocean. Based on laboratory experiments, Romero et al. (2012) followed up on this idea for deep water focused breaking waves, defining an empirical curve for b as a function of the maximum surface slope of the focusing wave packet. Derakhti, Banner & Kirby (2018) proposed an empirical relationship for parameterizing the breaking strength b as a function of the time rate of change dB/dt of the breaking onset parameter (Barthelemy et al. 2018) at breaking onset $B = B_{th}$, for deep or intermediate water 2D/3D focused waves. In this approach, by estimating the onset kinematics, the total energy dissipation of the resulting focused breaking can also be estimated.

To utilize this new criteria in FNPF models, a universal breaking parameterization extending from shallow to deep water conditions is needed, and the instantaneous energy dissipation needs to be specified explicitly. The objectives of the current study are thus to propose a universal breaking parameterization for FNPF models, with a particular focus in depth-limited breaking waves.

The paper is organized as follows. The formulations of the two FNPF models used are briefly

described in Section 2.2. The breaking onset/termination criteria and the breaking dissipation models are described in Section 2.3, including the hydraulic jump model and a newer dynamic model proposed by Derakhti, Kirby Jr, Banner, Grilli & Thomson (2018). Applications of both models are presented in Section 2.4 for several regular and irregular depth-limited breaking wave cases. Finally, the results are discussed and conclusions drawn in Sections 2.5 and 2.6.

2.2 FNPF models

FNPF models compute the irrotational motion of an incompressible and inviscid fluid, for which the fluid velocity $\mathbf{u}$ is represented by a scalar potential ϕ, with $\mathbf{u} = \nabla\phi$. For such flows, mass conservation becomes the Laplace equation for the potential,

$$\nabla^2\phi = 0 \tag{2.1}$$

in the fluid domain Ω of boundary Γ.

For two-dimensional (2D) transient free surface flows in a vertical plane (x, z), with a single-valued free surface elevation $\eta(x, t)$, the kinematic and dynamic free surface boundary conditions are,

$$\frac{\partial\eta}{\partial t} = \frac{\partial\phi}{\partial z} - \frac{\partial\eta}{\partial x}\frac{\partial\phi}{\partial x} \tag{2.2}$$

$$\frac{\partial\phi}{\partial t} = -g\eta - \frac{1}{2}|\nabla\phi|^2 - \frac{p_a}{\rho}, \tag{2.3}$$

on the boundary Γ_f and where g denotes the gravitational acceleration, ρ is the fluid density, and p_a is the free surface (atmospheric) pressure.

For typical 2D wave propagation problems, the fluid domain has an impermeable bottom boundary where a no-flow, Neumann bottom boundary condition is specified as,

$$\mathbf{u}\cdot\mathbf{n} = \frac{\partial\phi}{\partial n} = 0 \tag{2.4}$$

on the boundary Γ_b, where $\mathbf{n}$ denotes the outward unit normal vector to the boundary. Typical conditions at the lateral boundaries of the 2D domain will be periodicity, a wave maker for generating waves, or an absorbing beach for dissipating waves. The details of these boundary conditions are provided in Section 2.4 for each specific application.

In the following subsections, the equations are briefly presented, and the numerical methods are summarized for the two existing FNPF models that use different versions of the free surface boundary conditions and different numerical methods for solving Laplace's Equation (Eq. 2.1).

2.2.1 Misthyc

The Misthyc FNPF model, developed by Yates & Benoit (2015), solves Laplace's Equation (Eq. 2.1) by mapping the potential $\phi(x, z, t)$ onto a boundary fitted vertical coordinate $s \in [-1,\ 1]$ and using a spectral approach to express $\phi(x, s, t)$ as a linear combination of Chebyshev polynomials (following Tian & Sato 2008). At each time step, $\phi(x, s, t)$ is calculated by solving a system of $N_x(N_T + 1)$ linear equations, where N_x is the number of free surface nodes in the horizontal direction x and N_T is the maximum order of the Chebyshev polynomials (here $N_T = 7$, following Yates & Benoit 2015).

Assuming single-valued free surface elevations $\eta(x, t)$, the free surface boundary condition Eqs. (2.2-2.3) are expressed following Zakharov (1968) as,

$$\frac{\partial \eta}{\partial t} = \tilde{w}\left\{1 + \left(\frac{\partial \eta}{\partial x}\right)^2\right\} - \frac{\partial \eta}{\partial x}\frac{\partial \tilde{\phi}}{\partial x} \tag{2.5}$$

$$\frac{\partial \tilde{\phi}}{\partial t} = -g\eta - \frac{1}{2}\left(\frac{\partial \tilde{\phi}}{\partial x}\right)^2 + \frac{1}{2}\tilde{w}^2\left\{1 + \left(\frac{\partial \eta}{\partial x}\right)^2\right\} - \frac{p_a}{\rho}, \tag{2.6}$$

where $\tilde{\phi}(x, t) = \phi(x, z = \eta, t)$ and $\tilde{w}(x, t) = w(x, z = \eta, t) = \partial_s \phi(x, s, t)|_{s=1}$ are the velocity potential and the vertical velocity on the free surface Γ_f, respectively (where subscripts indicate partial derivatives). Note that Eqs. (2.5-2.6) can be transformed to express a relationship between η and $\tilde{\phi}$ in the form of a so-called Dirichlet-Neumann (DtN) operator (Craig & Sulem 1993). Following Bingham & Zhang (2007), Yates & Benoit (2015) formulated the DtN problem corresponding to these equations.

Assuming known $\eta(x, t)$ and $\tilde{\phi}(x, t)$ values on $\Gamma_f(t)$, once $\tilde{w}(x, t)$ is computed from the solution of Laplace's equation, these quantities are advanced to time $t + \Delta t$ by integrating Eqs. (2.5-2.6) with an explicit fourth-order Runge-Kutta scheme.

With the assumption of single-valued free surface in the Misthyc model, the resolution along the vertical for spectral approximation becomes undefined when the free surface becomes vertical, causing the model to numerically break down. To prevent this situation from occurring, impending wave breaking is detected using a breaking onset criterion, and a local damping is specified in the dynamic free surface boundary condition using an absorbing pressure p_a calibrated to simulate the wave breaking dissipation (Grilli, Horrillo & Guignard 2020, Guignard & Grilli 2001, Papoutsellis et al. 2019, Simon et al. 2019). Finally, waves are generated and absorbed at each end of the fluid domain by specifying relaxation zones that extend horizontally for $\sim 3L$, where L is the dominant wavelength. Details are provided for specific cases in Section 2.4.

2.2.2 Numerical Wave Tank (NWT)

Longuet-Higgins & Cokelet (1976) first proposed a 2D-FNPF model to simulate overturning waves in a periodic domain with constant depth, until the instant the breaker jet impinges the free surface. The model solved Laplace's Eq. (2.1) at each time t, based on a complex potential Boundary Integral Equation (BIE) formulation (in a conformally mapped space) and integrated

the kinematic and dynamic free surface boundary conditions Eqs. (2.2-2.3), expressed in a mixed Eulerian-Lagrangian frame of reference,

$$\frac{D\mathbf{r}}{Dt} = \frac{\partial \mathbf{r}}{\partial t} + (\mathbf{u}\cdot\nabla)\mathbf{r} = \mathbf{u} = \nabla\phi \tag{2.7}$$

$$\frac{D\phi}{Dt} = -gz + \frac{1}{2}|\nabla\phi|^2 - \frac{p_a}{\rho}, \tag{2.8}$$

by way of a predictor-corrector scheme, where $\mathbf{r}$ denotes the position vector on the free surface Γ_f. Dold & Peregrine (1985) later proposed a more accurate time integration scheme for this model, based on an explicit Taylor series expansion of both $\mathbf{r}$ and ϕ on the free surface, which requires computing the successive material derivatives of Eqs. (2.7-2.8) and solving additional Laplace's equations for the corresponding time derivatives of the potential, up to a desired order. However, their model was still expressed in a conformally mapped domain and limited to space-periodic waves propagating in constant depth.

The 2D-FNPF model of Grilli & Svendsen (1990*b*), Grilli & Horrillo (1997), Grilli et al. (1989), Grilli & Subramanya (1994, 1996) used here is based on the same approach, but is formulated in the physical space, which allows for modeling wavemakers or other types of exact generation of fully nonlinear waves, such as from streamfunction wave theory, an absorbing beach at the far end of the domain, and an arbitrary bottom bathymetry. Laplace's Eq. (2.1) is solved based on a BIE derived from Green's second identity,

$$\alpha(\mathbf{x}_i)\phi(\mathbf{x}_i) = \int_\Gamma \left\{ \frac{\partial\phi}{\partial n}(\mathbf{x})G(\mathbf{x}-\mathbf{x}_i) - \phi(\mathbf{x})\frac{\partial G}{\partial n}(\mathbf{x}-\mathbf{x}_i) \right\} \mathrm{d}\Gamma, \tag{2.9}$$

where ϕ is the velocity potential on the boundary Γ, α is the interior angle made by the boundary at point $\mathbf{x}_i$ and $G(\mathbf{x},\mathbf{x}_i) = -(1/2\pi)\ln r_i$ is the 2D free space Green's function (with $r_i = |\mathbf{x}-\mathbf{x}_i|$). In the model, this equation is discretized by various types of higher-order boundary elements and both regular and singular, as well as quasi-singular (occurring when two parts of the boundary are close to each other, e.g., in the tip of breaker jets) integrals are computed by very accurate methods (Grilli & Subramanya 1994, 1996). Additionally, extended compatibility conditions of the solution on both sides of the boundary are specified at corners in the domain (e.g., between a wave maker and the free surface, Grilli & Svendsen 1990*b*, Grilli & Subramanya 1996).

Assuming known $\eta(x,t)$ and $\phi(x,t)$ values on $\Gamma_f(t)$, once $\partial_n\phi$ is computed from the solution of Eq. (2.9), these quantities are advanced to time $t+\Delta t$, by integrating Eqs. (2.7-2.8), as in Dold & Peregrine (1985), based on explicit Taylor series expansions of both $\mathbf{r}$ and ϕ, limited here to second-order, hence requiring to solve an additional Laplace's equation for $\partial_t\phi$. This is done using a similar BIE to Eq. (2.9) in the same discretized computational domain, for a modest additional computational effort.

To generate waves, the NWT can simulate the motion of a flap or piston wavemaker, or the generation of numerically exact streamfunction waves on a lateral boundary (Grilli & Horrillo 1997). For wave absorption, an absorbing beach can be specified at the far end of the domain,

combining an absorbing free surface pressure for high-frequency waves and an absorbing lateral piston wavemaker for low-frequency waves (Grilli & Horrillo 1997).

2.3 Wave breaking model

Wave breaking in a FNPF model requires three steps: (i) a breaking onset criterion, which allows identifying where on the free surface and when a wave has reached a threshold beyond which breaking is inevitable, and indicating where on the free surface and when the application of an energy absorption in the model should start; (ii) based on wave parameters, a method to quantify the energy dissipation rate that should be specified in the model to damp waves that are identified to be breaking in (i); and (iii) a breaking termination criterion, which indicates where on the free surface and when the application of the energy dissipation should end.

2.3.1 Breaking onset criterion

As discussed in the introduction, in this work, breaking onset is detected based on the universal criterion proposed by Barthelemy et al. (2018) for deep and intermediate water depth breaking, and validated by Derakhti et al. (2020) for shallow water breaking of any type (i.e., spilling, plunging, or surging). These studies showed, for a wide variety of conditions leading to breaking such as energy focusing or effects of bathymetry, that a steepening wave whose ratio of the horizontal particle velocity at the crest u to the wave (or crest) celerity c, noted $B = u/c$, exceeds the threshold value $B_{th} = 0.85$, will eventually break; and waves for which $B < B_{th}$ will not break. It should be emphasized that wave breaking does not start at this threshold, but later on when $B \simeq 1$. Instead, the B criterion predicts where and when a wave crest passes a point of no return, beyond which it will eventually break. Derakhti et al. (2020) showed that, in shallow water, this occurs about $0.2\overline{T}$ in average after breaking onset, where $\overline{T}$ is the mean wave period in the sea state. In the FNPF models, it takes time for the absorbing pressure that is used to damp impending breaking waves (see next subsection) to extract enough energy from the wave crest to prevent breaking. Therefore, the energy dissipation in the models is applied when a wave reaches the threshold $B = B_{th}$.

One challenging aspect of applying this dynamic breaking criterion is that it is local and requires first that all wave crests be identified and tracked at all times over the entire free surface Γ_f, and second that the crest celerity, $c = dx_c/dt$ is computed accurately (where $x_c(t)$ denotes a given wave crest location as a function of time). Accordingly, in the models, similar to Guignard & Grilli (2001), Grilli, Horrillo & Guignard (2020), and Stansell & MacFarlane (2002), the instantaneous celerity $c(t)$ of individual tracked wave crests is computed by fitting a moving polynomial to $x_c(t)$ over a time interval $[t - n\Delta t,\ t]$ (where n denotes the number of time steps involved in the curve fit), and taking the time derivative analytically in the polynomial. Details of the numerical method used to compute c are provided in Appendix 1.

2.3.2 Breaking dissipation

2.3.2.1 Absorbing surface pressure

For waves that have been identified as evolving to breaking by the breaking onset criterion, the energy dissipation is specified, as in earlier work (Grilli & Horrillo 1997, Grilli, Horrillo & Guignard 2020, Guignard & Grilli 2001, Papoutsellis et al. 2019), using an absorbing (or damping) surface pressure p_a in the dynamic free surface boundary condition, Eq. (2.6) or (2.8) for the Misthyc and NWT models, respectively. This pressure is applied spatially across part of the back and front of the breaking wave crest, and it is defined as being proportional to the normal velocity of water particles at the free surface (Fig. 2.1),

$$p_a(x,t) = \nu_a(t)\, S(x) \frac{\partial \phi}{\partial n}(x,t) \qquad \forall x \in (x_l, x_r) \tag{2.10}$$

where $S(x)$ is a non-dimensional shape function (defined below) and $\nu_a(t)$ is an absorption function, with the dimension of $\rho\, c$ (i.e., units of kg m^{-2} s^{-1}), defined such that the rate of work produced by the pressure against the wave motion, $p_a\, \partial_n \phi$, integrated over the selected segment of the breaking wave surface, matches an expected rate of energy dissipation per unit length of crest, Π_b for the wave, as will be described in the following subsection.

For single valued surface elevations Eq. (2.10) yields,

$$\nu_a(t) = \frac{\Pi_b}{\int_{x_l}^{x_r} S(x)(\partial_n \phi)^2 \sqrt{1+(\partial_x \eta)^2}\, dx}. \tag{2.11}$$

in which the square root is the Jacobian, $d\Gamma/dx$.

The limits of integration in Eq. (2.11) are defined across each breaking wave crest, with (x_l, x_r) located near the troughs located behind and ahead of the breaking wave crest, respectively, such that $|\partial_n \phi| < \varepsilon\, |\partial_n \phi|_{max}$, where $\varepsilon \ll 1$ (here $\varepsilon = 10^{-4}$). As shown in Fig. 2.1, $S(x)$ is a smooth function that varies from 0 to 1 over the breaking region, with a ramp to ensure smooth transitions of p_a between zero in non-breaking regions and its calculated value in breaking regions (Grilli, Horrillo & Guignard 2020, Guignard & Grilli 2001, Papoutsellis et al. 2019),

$$S(x) = \begin{cases} 0, & x \le x_l \\ \cos\left(\frac{\pi}{2}\frac{x-x_{l1}}{x_l-x_{l1}}\right), & x_l \le x \le x_{l1} \\ 1, & x_{l1} \le x \le x_{r1} \\ \cos\left(\frac{\pi}{2}\frac{x-x_{r1}}{x_r-x_{r1}}\right), & x_{r1} \le x \le x_r \\ 0, & x \ge x_r \end{cases} \tag{2.12}$$

where $x_{l1} = x_l + \alpha(x_r - x_l)$ and $x_{r1} = x_r - \alpha(x_r - x_l)$, $\alpha = 0.1$.

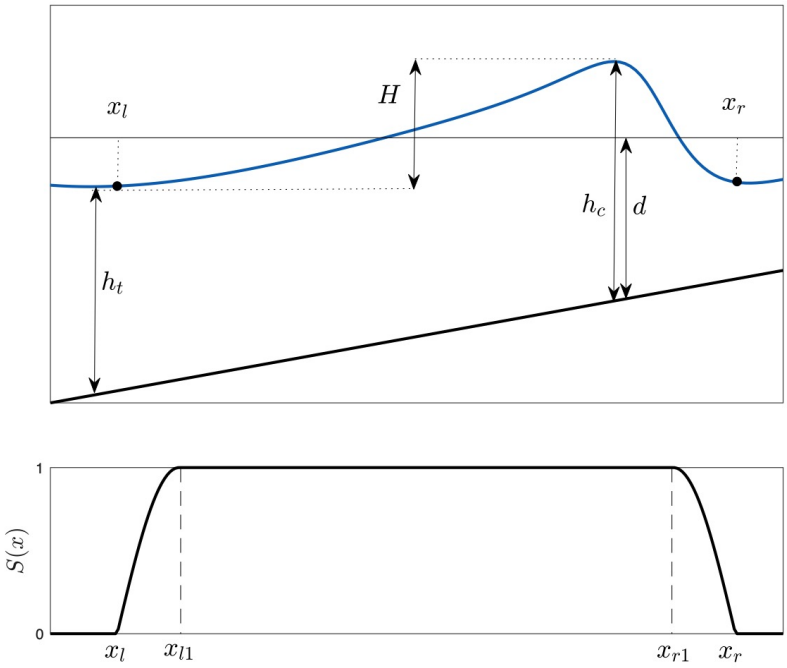

Figure 2.1: (top) Geometric parameters used to calculate the HJ dissipation, and (bottom) the shape function $S(x)$

2.3.2.2 Rate of energy dissipation

Two different parameterizations of the rate of energy dissipation in breaking waves, Π_b, will be considered in this work. The first one, based on the hydraulic jump analogy introduced in earlier work (Grilli, Horrillo & Guignard 2020, Guignard & Grilli 2001, Papoutsellis et al. 2019), will be the default method used in both models, and the second one, based on the time rate of change of the breaking onset criterion, recently proposed by Derakhti, Kirby Jr, Banner, Grilli & Thomson (2018), will be used for comparison.

Hydraulic jump analogy: In earlier work, Guignard & Grilli (2001), Papoutsellis et al. (2019), and Grilli, Horrillo & Guignard (2020) parameterized Π_b based on the classical energy dissipation of an hydraulic jump (HJ), i.e.,

$$\Pi_h = \rho g c\, d \frac{H^3}{4 h_c h_t} \quad \text{with} \quad \Pi_b = \mu \Pi_h, \tag{2.13}$$

where c is the wave phase speed (or crest celerity), d the undisturbed water depth below the point of maximum front slope, H the wave height (measured trough to crest), h_c the total depth below wave crest, and h_t the total depth below wave trough (Fig. 2.1). As shown in Svendsen et al. (1978) and Stive (1984), the equation for Π_h can be obtained easily from a control volume approach by deriving equations for mass, momentum, and energy conservation assuming periodic waves with a uniform velocity over depth, hydrostatic pressure, and negligible bottom friction. Based

on laboratory experiments for spilling breakers propagating over mild slopes, Svendsen et al. (1978) proposed that $\mu = 1.5$.

Note, for symmetric linear waves breaking over mild slopes, $H = 2a$, with a the wave amplitude, $c \simeq c_\ell = \sqrt{gd}$, $h_t \simeq d - a$ and $h_c \simeq d + a$, and Eq. (2.13) transforms into,

$$\Pi_b = \mu \left(\frac{\epsilon}{b}\right) \frac{2F^3}{1 - F^2} \tag{2.14}$$

$$\text{with} \quad \epsilon = b\rho g^{-1} c^5, \tag{2.15}$$

where $F = ga/c_\ell^2$ is the wave Froude number (Kirby 1998), which for long breaking waves in shallow water reduces to $F \simeq a/d$, ϵ is the breaking energy dissipation rate per unit of wave crest width proposed by Duncan (1981, 1983), based on measurements of steady spilling breakers in deep-water, and b is a non-dimensional breaking strength parameter that was parameterized as a function of the hydrofoil characteristics and submergence depth used in these experiments. To obtain $\Pi_b = \epsilon$ requires that $b \simeq 2\mu F^3$ in Eq. (2.14), assuming $F^2 \ll 1$. Based on Svendsen's parameterization, for small F, the HJ breaking strength parameter can thus be expressed as $b \simeq 2\mu F^3 = 3F^3$.

Making various scaling arguments of the turbulent energy dissipation for unsteady breakers in deep or intermediate water, Drazen et al. (2008) showed that $b \propto F^{2.5}$, while more recently, using different scaling arguments, Mostert & Deike (2020) proposed that $b \propto F^{3.5}$ for unsteady shallow water breakers. Thus, the above formulation of b falls in between these independent results, without any clear guidance on which result is most realistic. Note that, consistent with the analysis of Drazen et al. (2008), Romero et al. (2012) and Derakhti, Kirby Jr, Banner, Grilli & Thomson (2018) assumed that $b \propto F^{2.5}$. It is outside the scope of this paper to attempt to reconcile these conflicting results, which will be the object of other studies (Derakhti et al. 2022).

The default parameterization of energy dissipation in both FNPF models used in the present applications will thus be based on Eq. (2.13), with $\mu = 1.5$. It should be noted that, similar to the breaking onset criterion used to detect impending breaking in the models, computing Π_h requires identifying individual wave crests and troughs and accurately computing the crest celerity. The same method used to compute the onset criterion is thus used to compute the parameters required for estimating the wave energy dissipation.

Parameterization based on time rate of breaking onset criterion: By performing numerical simulations of focused waves, Romero et al. (2012) and Derakhti et al. (2016) extended Duncan's parameterization of the rate of energy dissipation ϵ to intermediate water, steepness-limited, plunging breaking waves and irregular wave trains. Following the introduction of the breaking onset criterion based on B by Barthelemy et al. (2018), Derakhti, Banner & Kirby (2018) observed in their NS simulations of focused wave trains, that the slope of $B(t)$ at breaking onset was correlated with the average breaking power dissipated in the model, from breaking onset to termination, $\langle\epsilon\rangle$, or the corresponding breaking strength $\overline{b}$ obtained from Eq. (2.15). On this

basis, they proposed a new parameterization of the breaking strength parameter,

$$\overline{b} = \frac{g\langle\epsilon\rangle}{\rho c_{lb}^5} = 0.034\,(\gamma - 0.30)^{2.5} \tag{2.16}$$

$$\gamma = T_b \left.\frac{dB}{dt}\right|_{B=B_{th}} \tag{2.17}$$

computed based on wave crest parameters at breaking onset and a breaking wave period, $T_b = L_b/c_{lb}$, estimated based on, $c_{lb} = \sqrt{g\,\tanh(k_b d)/k_b}$, with $k_b = 2\pi/L_b$, the linear wave celerity at breaking in arbitrary depth, and L_b a relevant breaking wave length calculated based on the method proposed by Derakhti et al. 2020. Specifically, the width of the breaking crest is taken as twice the distance between two zero-crossing points, except in cases where, particularly for long waves, this does not describe well the breaking region. In this case, an equivalent zero-crossing distance is computed (cf., Fig. A2 in Derakhti et al. 2020), here with a manual computation instead of a skew Gaussian due to the simpler geometry of a BEM result compared to their Navier-Stokes solver. In some of the applications in Section 2.4, $\overline{b}$ will be computed with Eq. (2.17) and compared to results based on the HJ analog. To do so, the time rate of change of B at the threshold will be calculated by applying a linear fit to the B values computed in the interval [0.82, 0.85] (In the NWT, the nodes are regridded every few time steps (Grilli & Subramanya 1996), thus the time variation of B at the crest may exhibit sawtooth oscillations when the wave becomes very steep as B approaches the threshold value. In this case, regridding is turned off when $B \approx [0.7,\ 0.85]$.) Note that $\overline{b}$, which quantifies the average energy dissipation rate during a breaking event based on γ, computed at breaking onset, is not the time average of $b(t)$, which quantifies the instantaneous energy dissipation rate based on instantaneous wave parameters.

As discussed before, Derakhti et al. (2020) showed that the B criterion also applies to shallow water breaking waves and, hence, is universal. Calculating the energy dissipation rate in their model for shallow water breaking waves, Derakhti, Kirby Jr, Banner, Grilli & Thomson (2018) confirmed the parameterization of $\overline{b}$ in Eq. (2.17) for $\gamma < 1.11$, with the breaking strength parameter reaching an upper bound $b_{max} = 0.02$ for larger γ values, although this parameterization, particularly for large γ, was revised by Derakhti et al. (2022).

Given $\Pi_b = \epsilon$, the second parameterization of energy dissipation considered in both FNPF models in the present applications will be based on the expression of ϵ in Eq. (2.15), with b obtained from Eq. (2.17) for $\gamma \leq 1.3$, and $b = b_{max}$ for $\gamma \geq 1.3$. As before, most wave crest parameters required to compute Π_b are similar to those used to compute B and are already available in the models.

2.3.3 Breaking termination criterion

Breaking termination is also an important factor to extract accurately the appropriate amount of energy from breaking waves in the models. However, unlike in actual waves, as would for instance be simulated in a NS-VOF model (Derakhti et al. 2020), the value of B does not grow much beyond or remain above B_{th} in the FNPF model once dissipation is applied and a different method is required to detect breaking termination. To be consistent with the onset criterion, the

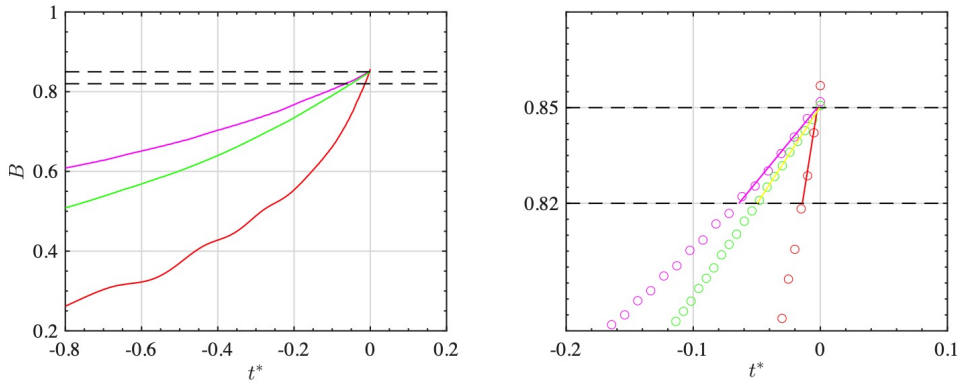

Figure 2.2: Evolution of $B = u/c$ in simulations with the Misthyc model as a function of non-dimensional time $t^* = (t - t_b)/T_b$ (t_b denotes the time of breaking onset when $B = B_{th} = 0.85$), for periodic: (i) plunging breaking waves propagating over a bar, from Beji & Battjes (1993) (BB-regular, red); (ii) spilling breaking waves propagating over a plane slope, from Hansen & Svendsen (1979) (HS, magenta); and shoaling and spilling breaking waves propagating over a plane slope, from Ting & Kirby (1994) (TK, green).

termination criterion is based on B reaching a value B_{off} that is lower than the onset threshold, and needs to be calibrated based on benchmark data. For the applications considered here, the optimal B_{off} value appeared to be problem dependent. Specific values and their implications are discussed in the section 2.4.2.

2.4 Applications

2.4.1 Comparison of the two formulations of breaking dissipation

Before presenting detailed applications using the same breaking onset/termination criteria, it is of interest to analyze and compare values of B and dB/dt computed near and at the breaking onset for various cases, as well as the breaking strength parameter b and/or dissipation rate Π_b resulting from the two parameterizations of the rate of energy dissipation discussed before. These are the experimentally validated depth-limited HJ spilling breaker model (Grilli, Horrillo & Guignard 2020), whose energy dissipation rate is given by Eq. (2.13) and for which b can readily be obtained based on the expression of ϵ in Eq. (2.15), assuming $\Pi_b = \epsilon$, and the newer dissipation rate based on dB/dt and γ (Derakhti, Kirby Jr, Banner, Grilli & Thomson 2018), with b given by Eq. (2.17).

In the following, breaking wave parameters calculated based on the HJ breaking model, with Misthyc and the NWT, are compared by simulating laboratory experiments of: (i) periodic shoaling and plunging breaking waves propagating over a bar, from Beji & Battjes (1993) (BB-regular); (ii) periodic shoaling and spilling breaking waves propagating over a plane slope, from Hansen & Svendsen (1979) (HS); and (iii) periodic shoaling and spilling breaking waves propagating over a plane slope from Ting & Kirby (1994) (TK). The details of the set-up and numerical parameters

for these simulations are described in the following subsections. Note, the HJ dissipation model and corresponding Π_b values were previously experimentally validated using the NWT model for the HS test cases by Grilli, Horrillo & Guignard (2020), and using the Misthyc model for the regular and irregular BB cases by Simon et al. (2019), and with another FNPF model called HCMT, for the regular wave TK and BB cases by Papoutsellis et al. (2019).

In each test case, the HJ breaking dissipation model is used, and the parameter b is calculated using the expression of ϵ in Eq. (2.15), based on the average power dissipated in the model over the breaking onset/termination range, $\epsilon = \langle \Pi_b \rangle$, through the application of the absorbing pressure p_a based on Eqs. (2.10-2.12), with the instantaneous $\Pi_b(t)$ given by Eq. (2.13). For the second parameterization of dissipation, the corresponding b values are found using Eq. (2.17), based on the wave parameters computed at breaking onset.

Fig. 2.2 shows the evolution of B computed leading up to wave breaking with the Misthyc model as a function of the non-dimensional time $t^* = (t - t_b)/T_b$, where t_b is the time of breaking onset over the region of interest for calculating dB/dt. Consistent with Derakhti, Banner & Kirby (2018), Derakhti, Kirby Jr, Banner, Grilli & Thomson (2018), of the three test cases shown, the plunging breaker case (BB-regular) has the fastest rate of change of B at the threshold, whereas the spilling breaker cases (HS and TK) show slower changes in B. The calculation of dB/dt was found to be sensitive to the interval over which it is calculated, as well as to the spatial and temporal resolution of the simulation. Fig. 2.2 (right) shows the linear fit applied to B in the interval [0.82, 0.85], used to compute dB/dt and, for this interval for the HS case, Table 2.1 shows the sensitivity of the dB/dt and γ values calculated for different spatial and temporal grids.

Fig. 2.3 shows the average b values computed in each test case using the HJ model as a function of γ, compared to the values predicted by the second parameterization based on γ (Eq. 2.17). Average values of b computed over the breaking region using the HJ dissipation range within [0.02, 0.08], and corresponding γ vary within [0.6, 2.5]. These results are in moderate agreement with those of the Derakhti, Banner & Kirby (2018), Derakhti, Kirby Jr, Banner, Grilli & Thomson (2018) parameterization, when $\gamma \in [1,\ 2]$. Some differences between these two parameterizations of b are to be expected since even the Derakhti, Banner & Kirby (2018), Derakhti, Kirby Jr, Banner, Grilli & Thomson (2018) parameterization is only a curve fit, with significant spread of individual values. Recall also that the breaking strength shown here is based on an average energy dissipation rate, $\langle \epsilon \rangle$, which will have a different value depending on the duration of active breaking, which in both models could be adjusted without affecting significantly the resultant wave characteristics. Finally, in this paper potential flow is assumed, while wave breaking transfers energy to non-potential components of the flow (e.g., vorticity) that may not be dissipated and would appear as an over-prediction of the energy dissipation.

Based on the b values simulated in these applications, an instantaneous dissipation rate $\Pi_b = \epsilon$ defined with the expression of ϵ in Eq. (2.15), based on a constant breaking strength $b = 0.05$, was also tested. Since the wave celerity used in the definition of ϵ is a function of space and time, $c(x, t)$, this parameterization also provides a time-varying dissipation rate. For instance, for the BB-regular case, Fig. 2.4 shows that this constant breaking strength yields an instantaneous

Model	$\Delta x\ (m)$	$\Delta t\ (s)$	$\frac{dB}{dt}\|_{B=B_{th}}\ (s^{-1})$	γ
Misthyc	0.020	0.008	0.974	0.788
Misthyc	0.028	0.007	0.885	0.726
NWT	0.031	0.008	1.00	0.774
NWT	0.041	0.010	1.075	0.791

Table 2.1: Sensitivity of γ computed with Eq. (2.17) for different spatial and temporal resolutions, for the Hansen & Svendsen (1979) (HS) case.

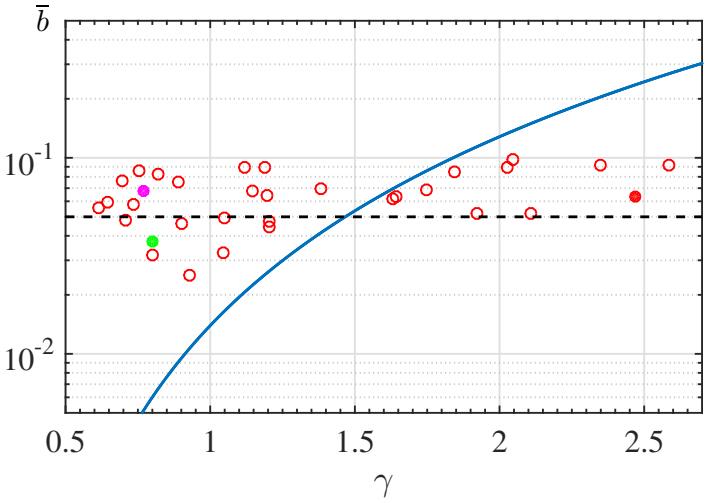

Figure 2.3: Average breaking strength $\overline{b}$ computed for the HJ parameterization, as a function of γ for depth-limited breaking waves simulated in Misthyc including: (filled circles) regular wave cases, magenta: HS, green: TK and red: BB; (hollow circles) BB-irregular cases. For comparison, the empirical parmaterization from Eq. 2.17 proposed by Derakhti, Banner & Kirby (2018), is indicated with a solid line. The dashed line shows the constant strength average breaking value $b = 0.05$ used in the Mis-005 parameterization.

dissipation rate that agrees well with that calculated using Eq. (2.13) for the HJ parameterization. Therefore, for the BB-regular case, the constant strength approach would likely be accurate enough, and Fig. 2.3 shows that for the wider range of cases that will be considered hereafter, the average b value computed in the model in each case is on the same order as $b = 0.05$.

2.4.2 Experimental validations

In this subsection, the results of numerical simulations with one or both FNPF models, using the energy dissipation rate of the HJ model, the constant breaking strength $b = 0.05$, or both, are compared with laboratory experiments performed for five standard benchmark cases. The five test cases are the periodic spilling breaker experiments over a plane slope of Hansen & Svendsen (1979), and Ting & Kirby (1994), the regular and irregular plunging breakers over a bar of Beji & Battjes (1993), and the irregular breaking waves over a bar of Adytia et al. (2018). In the

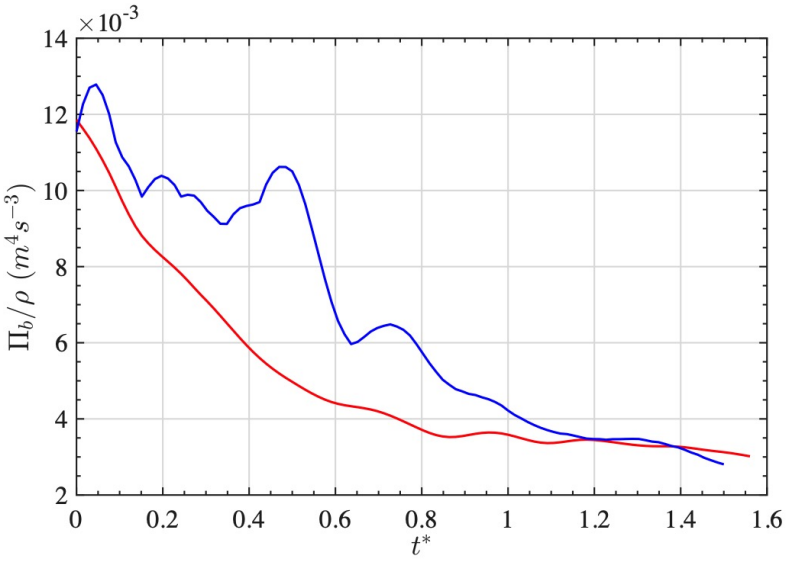

Figure 2.4: Comparison of the instantaneous energy dissipation rate $\Pi_b(t)$ calculated for the plunging BB-regular case in the Misthyc model using: (blue) the HJ analogy Eq. (2.13), or (red) the Mis-b005 Eq. (2.15) parameterization with $b = 0.05$.

models, fully nonlinear periodic waves are generated based on streamfunction wave theory in the generation zone for Misthyc (Benoit et al. 2002), and using an exact wavemaking (particle curtain) boundary (Grilli & Horrillo 1997) for the NWT. Irregular waves are simulated in the model using a flap wave maker boundary (e.g., Grilli & Horrillo 1997).

The model discretizations in space and time are specified such that the Courant number, CFL $\approx$ 1.0 in Misthyc (as suggested by Yates & Benoit 2015) and CFL ≈ 0.45 in the NWT (found to be optimal by Grilli & Subramanya 1996). Using the optimal CFL number for each model, a refined spatial discretization is specified in each case to ensure high numerical accuracy (see Grilli & Subramanya 1996 for guidance). Fig. 2.5 shows examples of the instantaneous free surface elevation computed for the HS test case for a range of spatial discretizations after simulations reach a quasi-steady state in the models. These are defined based on the initial spatial discretization on the free surface Δx, where $L/\Delta x = 35$, 50, or 70, and L is the incident wave length. The simulation results show that free surface elevations are nearly identical in deeper water for both models over the range of tested discretizations. Small differences can only be seen in shallower depths, particularly near the wave crests. Based on these results, in all the simulations discussed hereafter, the spatial discretization was prescribed such that $L/\Delta x > 50$ (note, for irregular waves, L denotes the dominant wavelength). Table 2.2 summarizes the spatio-temporal parameters used in the simulations with the Misthyc and NWT models for the five benchmark cases detailed in the following sections.

2.4.2.1 Periodic spilling breakers on a slope - Hansen & Svendsen (1979)

Hansen & Svendsen (1979) (referred to as HS) performed experiments for periodic waves shoal-

Test case	$\Delta x\ (m)$		$\Delta t\ (s)$		Domain	T_{max}
	Misthyc	NWT	Misthyc	NWT	length (m)	(s)
HS	0.019	0.031	0.008	0.008	22.7	25
TK	0.019	0.055	0.008	0.013	29.7	32
BB-regular	0.014	0.048	0.01	0.015	34.4	35
BB-irregular	0.02	-	0.01	-	30	600
AH	0.02	-	0.01	-	60	500

Table 2.2: Numerical parameters used in the simulations with the Misthyc and NWT models for the five experimental benchmark test cases.

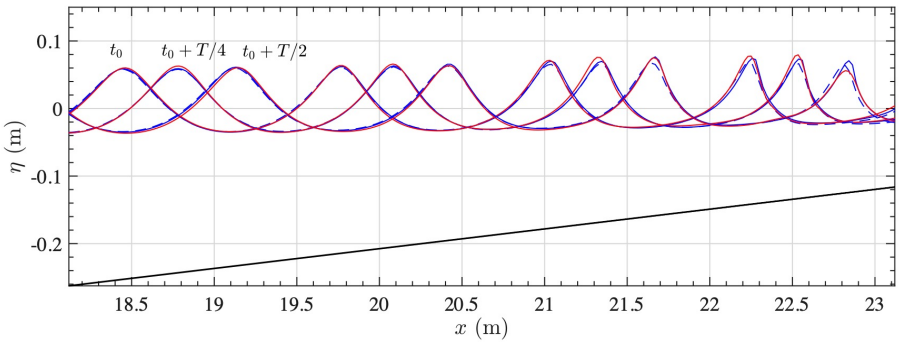

Figure 2.5: Sensitivity of the simulation results to the spatial discretization for the HS test case using the NWT (blue dashed, $L/\Delta x = 35$, and blue solid, $L/\Delta x = 50$) and Misthyc (solid red with $L/\Delta x = 70$) model.

ing and spilling breaking waves propagating over a mild slope. The wave tank had a constant initial depth of $h_0 = 0.36$ m, from the wavemaker up to $x = 14.78$ m, the toe of the $1/34.26$ slope. Regular waves with an initial height $H_0 = 0.095$ m, period $T = 1$ s, and incident wavelength $L_0 = 1.43$ m were generated at the wavemaker (note, these waves were generated in intermediate waver conditions, with $h_0/L_0 = 0.252$). This benchmark was simulated with both Misthyc and the NWT, using the energy dissipation rates from the HJ and Mis-b005 or NWT-b005 models, respectively (see Table 2.2 for the numerical parameters used). Since wave runup was not considered in either model, an absorbing beach was modeled for $x \geq 25.5$ m with a deepening bathymetry (for $x \in [25.5,\ 27]$ to induce deshoaling, which aids the absorption of waves) followed by constant depth in the absorption zone (see Fig. 2.6a and Fig. 1 in Grilli, Horrillo & Guignard 2020 for details). In these experiments, the breakers reach the shoreline, so $B_{\text{off}} = 0$ is used as the breaking termination criterion. Preliminary tests with larger values appeared to cause wave reformation that was not observed in the experiments. In the numerical models, breaking onset with $B = B_{th} = 0.85$ occurs at $x_b \simeq 22.2$ m, as compared to $x_b \simeq 22.5$ m in the experiments. The model results were averaged over 5 successive wave periods after the simulations reached a quasi-steady state.

Fig. 2.6b shows (in both the experiments and all numerical simulations) the wave celerity normalized by the deep water linear celerity $c_0 = gT/(2\pi)$ gradually decreases in the shoaling region. In general, the simulation results agree well with the experimental measurements, but less so in breaking region ($x > x_b$; where experimental data is very noisy) due to unsteady variations in calculations of the derivative of the wave crest displacement. For $x < x_b$, c/c_0 is slightly larger than in experiments, which is consistent with the results of Grilli, Horrillo & Guignard (2020). Fig. 2.6c shows the wave height normalized by H_0 gradually increases over the shoaling region then rapidly decreases beyond breaking onset and, in all cases, the simulation results agree well with experimental measurements.

Considering the two parameterizations of energy dissipation in Misthyc, the simulation results show only small differences throughout the simulations, and these differences, as well as those with the NWT results, mostly occur at the far end of the tank for $x > 23.5\ m$. The differences likely result from the different numerical methods and discretizations, as well as the regridding used in the NWT, where the Eulerian-Lagrangian approach causes grid points to cluster around the breaking crests. To limit this clustering, regridding is periodically calculated in the model using cubic shape functions (Grilli & Subramanya 1996), which may slightly affect the application of the breaker model around the breaking crests.

Note, when using the NWT with the HJ model and a geometric breaking criterion (front slope $\beta_{max} = 37^o$) for this case, Grilli, Horrillo & Guignard (2020) predicted breaking onset slightly sooner at $x_b = 21.75$ m and, as a consequence, had lower H/H_0 values at $x = 22.5$ m relative to both the present simulations and the experimental data.

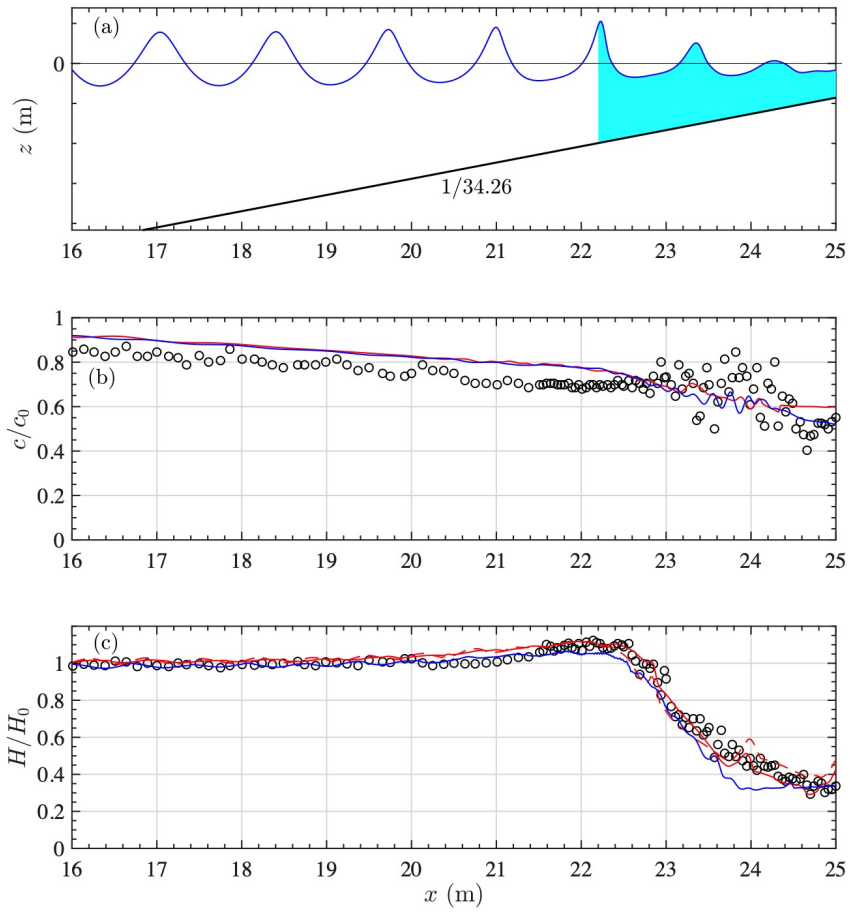

Figure 2.6: (a) Bathymetry of the Hansen & Svendsen (1979) (HS) experimental set-up for periodic shoaling and spilling breaking waves, where the shaded cyan region indicates the wave crest location from the onset of wave breaking (note an absorbing beach is specified in the models for $x \geq 25.5$ m). Spatial evolution of the (b) wave celerity, and (c) wave height in the experimental data (circles), Misthyc using the HJ model (dashed red line), Mis-b005 (solid red line) and NWT-b005 (solid blue line), averaged over 5 successive wave periods after a quasi-steady state is reached.

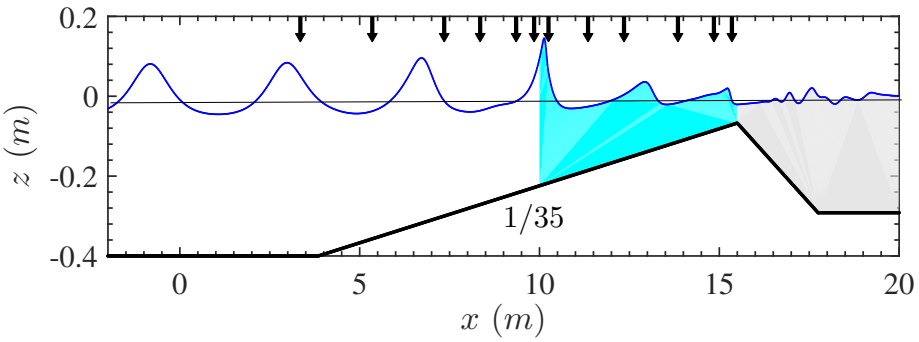

Figure 2.7: Setup for Ting & Kirby (1994) laboratory experiments of periodic spilling breakers propagating over a 1/35 slope, with black arrows showing the locations of the 12 wave gauges. The cyan shading indicates the simulated wave breaking region, from onset to termination. The gray shading indicates the beach absorption zone.

2.4.2.2 Periodic spilling breakers on a slope - Ting & Kirby (1994)

Experiments of shoaling and spilling breaking waves propagating over a plane 1/35 slope, similar to those by HS in the previous section, were performed by Ting & Kirby (1994) (referred to as TK). Periodic waves of height $H_0 = 0.125$ m, period $T = 2.0$ s, and wavelength $L_0 = 3.85$ m, were generated by a piston wavemaker and propagated in a tank of constant depth $h_0 = 0.4$ m to $x = 3.85$ m, the toe of the slope. Similar to the previous test case, in the models, an absorbing beach was specified for $x > 15.5$ m, starting in a water depth $h = 0.067$ m and gradually deepening to $h = 0.29$ m at $x = 18$ m. As in the previous case, $B_{\text{off}} = 0$. Fig. 2.7 shows the experimental setup along with the the locations of the 12 wave gauges that measured the free surface position.

For this test case, the models detected the onset of wave breaking at $x_b \simeq 10.0$ m, with $h_b = 0.21$ m and $H_b = 0.178$ m, which agrees well with the experimental values, $x_{be} = 10.25$ m, $h_{be} = 0.196$ m, and $H_{be} = 0.162$ m. Fig. 2.8 shows a 4-second window of the measured and simulated free surface elevation at 12 wave gauges after a quasi-steady state was achieved. The free surface elevations computed with Misthyc and the NWT for $x < x_b$ are in close agreement with each other, and are nearly identical the experimental measurements. Note, using a kinematic onset criterion ($\gamma_i\sqrt{gh}$), Papoutsellis et al. (2019) reported breaking onset at $x = 9.7$ m, which led to an underestimation of the crest and wave height at gauge $x = 10.25$ m, whereas, using the $B = 0.85$ criterion, both models predict more accurately the wave elevation at this gauge. Beyond breaking (for $x > x_b$), results from Misthyc using the HJ model agree reasonably well with the experiments at all subsequent gauges, whereas using Mis-b005 yields similar results until $x = 12.35$ m, but increasingly large differences in the crest area for shallower gauges. In contrast, the results of NWT-b005 yield surface elevations in better agreement with those predicted by Misthyc with the HJ energy dissipation model.

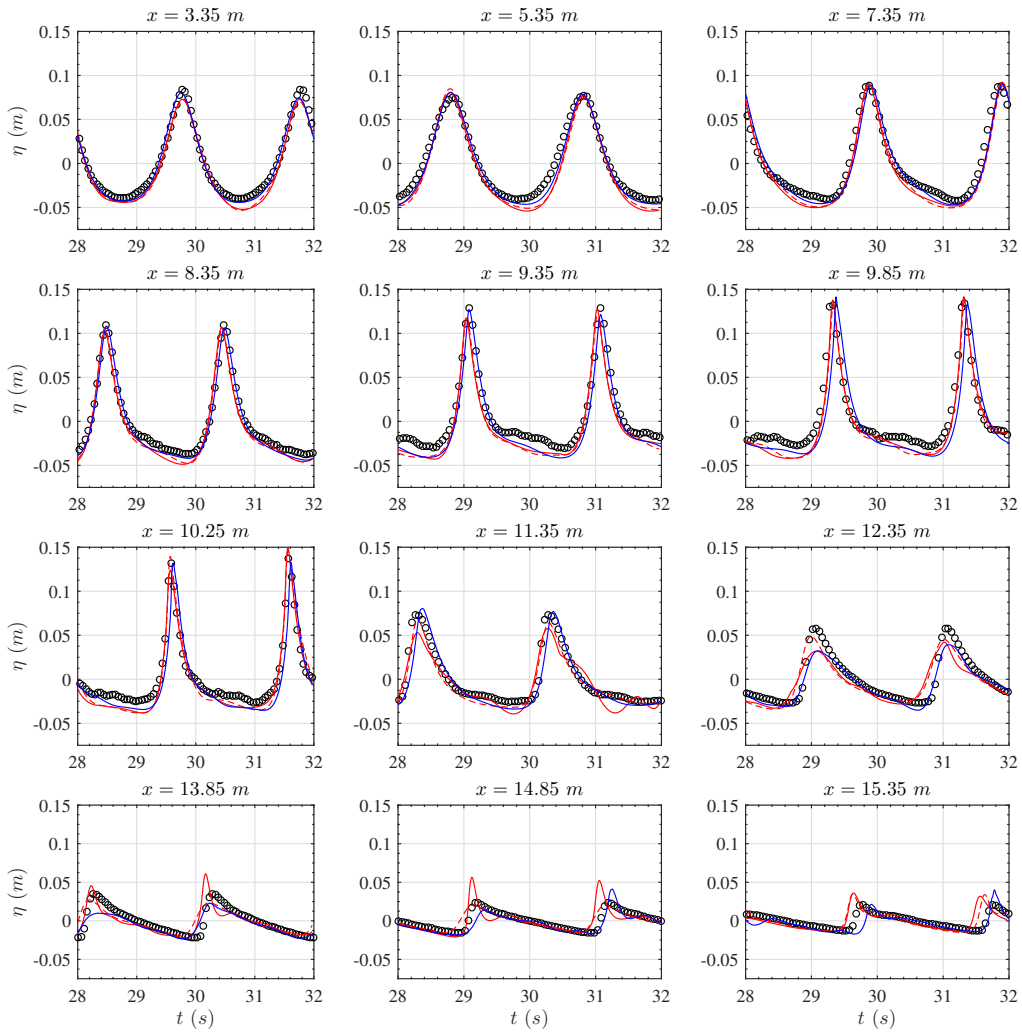

Figure 2.8: Comparison of the temporal evolution of the free surface position measured at the gauge locations from Ting & Kirby (1994) for regular spilling waves (circles) with simulations using Misthyc with the HJ model (dashed red line), Mis-b005 (solid red line), and NWT-b005 (solid blue line).

2.4.2.3 Periodic plunging breakers over a bar - Beji & Battjes (1993)

Beji & Battjes (1993), among others, performed laboratory experiments for periodic waves propagating over a trapezoidal bar (referred to here as BB-regular). Some of the generated incident waves were sufficiently steep to break over the bar as plunging breakers. Fig. 2.9 shows the set-up of the computational domain used in the models to simulate BB's experiments, with arrows indicating the locations of the wave gauge, where time series of the free surface elevation were measured in experiments. Waves were generated at $x = 0$ in the constant depth region with $h_0 = 0.4$ m, shoaled over the bar with a mild 1/20 offshore slope, and then broke over the crest of the bar where $h = 0.1$ m, before the water depth increased again over the 1/10 onshore slope of the bar.

The target periodic wave characteristics in these experiments were a height $H_0 = 0.054$ m, period $T = 2.5$ s, and wavelength $L_0 = 4.8$ m in the region of constant depth. However, in the wave gauge measurements, the actual wave height was $H_0 \simeq 0.042$ m at the toe of the slope, which was thus used as the wave height in the simulations. Simulations were performed with Misthyc and the NWT using $b = 0.05$ and, in both models, breaking onset occurred at $x_b \simeq 12.2$ m, as compared to between 12 and 13 m in experiments. The breaking termination was specified at $B_{\text{off}} = 0.3$ in the models, which occurs before the water depth increases shoreward and causes wave deshoaling (end of cyan shaded region in Fig. 2.9).

Fig. 2.10, compares the measured time series of free surface elevations to those computed in the models. They agree well in the shoaling region, for $6 < x < 12$ m, and in the breaking region, for $12 < x < 14$ m. Larger differences start occurring for $x > 14$ m, but wave breaking on top of the bar and deshoaling for $14 < x < 17$ m are simulated well overall. Differences between the results of both models are small, except for higher harmonics generated on top of and beyond the bar, which Misthyc does not capture as well as the NWT. This may be due to the limited number of vertical layers (N_T), or the difference in timestep used.

The effect of the breaking termination criterion value was tested in the Misthyc model in the range $B_{\text{off}} = 0.2$ to 0.35. Fig. 2.11 shows the simulated and measured spatial variation of the significant wave height H_s throughout the domain. The results show that, in the zone after wave breaking (for $x > 14$ m), using $B_{\text{off}} = 0.20$ leads to underpredicting H_s, whereas using $B_{\text{off}} = 0.35$ leads to overpredicting it. Using $B_{\text{off}} = 0.30$ or even 0.25, allows reproducing well H_s measured in the experiments after the bar. Thus, $B_{\text{off}} = 0.30$ was selected for all cases shown here involving submerged bars (where waves deshoal).

2.4.2.4 Irregular plunging breakers over a bar - Beji & Battjes (1993)

Using the same submerged bar, water depth, and set of wave gauges (see Fig. 2.9), Beji & Battjes (1993) also tested cases with irregular incident wave trains generated at the wavemaker based on a JONSWAP spectrum with significant wave height $H_s = 0.049$ m and peak spectral period $T_p = 1/f_p = 2.5$ s (referred to as BB-irregular). In the simulations, performed here using only Misthyc with $b = 0.05$, incident waves are specified as a linear superposition of periodic waves

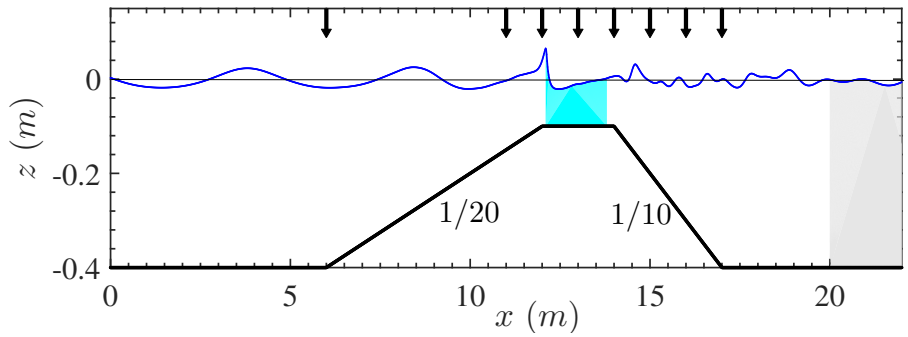

Figure 2.9: Set-up of the computational domains in the simulations of the Beji & Battjes (1993) experiments for periodic waves shoaling and plunging breaking over a bar (BB). Arrows indicate the locations of wave gauges in the experiments and simulations. Wave breaking occurs in the models in the cyan shaded region, from onset to termination, and the gray shaded region indicates the absorbing beach. Note, the free surface shown is of BB-regular.

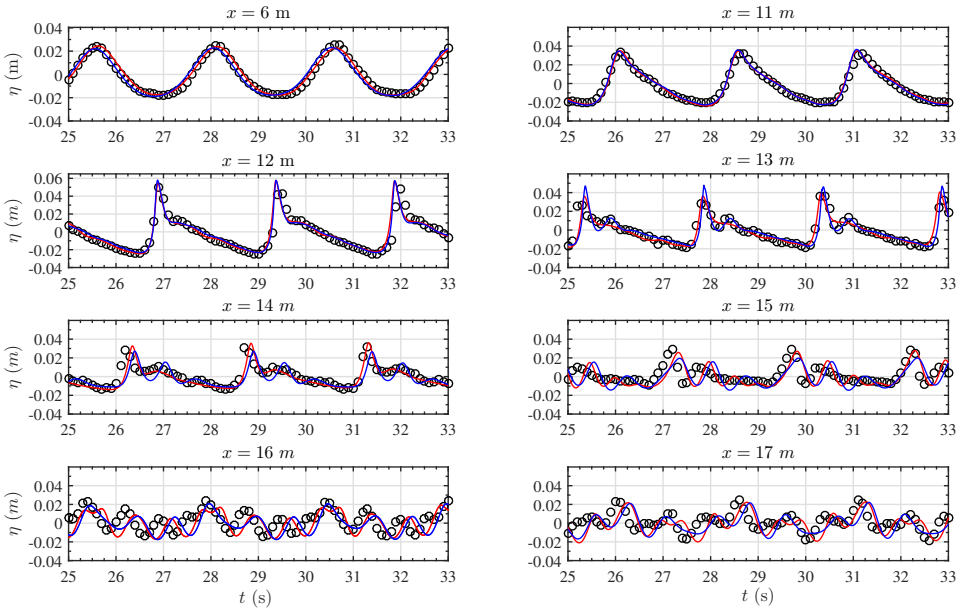

Figure 2.10: Comparison of the temporal evolution of the free surface at the gauge locations from the Beji & Battjes (1993) test case for regular plunging waves (circles) with Mis-b005 (red solid line) and NWT-b005 (blue solid line).

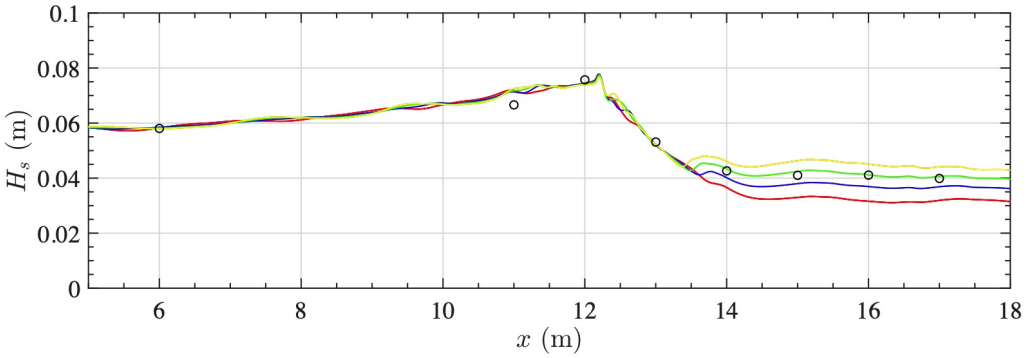

Figure 2.11: Spatial evolution of the significant wave height H_s for the BB-regular experiments (circles) and simulations with the Mis-b005 model using different breaking termination criteria $B_{\text{off}} =$: (red) 0.2, (blue) 0.25, (green) 0.30, and (yellow) 0.35.

in the frequency range $[0.25f_p,\ 5f_p]$, obtained from an FFT of the experimental free surface elevation measurements at the wave gauge located at $x = 6\ m$. Once again, $B_{\text{off}} = 0.30$ is used in the model.

The simulation is run for 600 s or 240 peak periods, and breaking of the steepest waves were observed over the bar crest, as in the experiments where they were plunging breakers. To compare the simulated and experimental results, several wave statistics are computed based on the time series of free surface elevations at the wave gauges. These quantities are the significant wave height (H_s), the asymmetry (As), a measure of left-right differences in a wave, the skewness (Sk), a measure of deviation in crest-trough shape, and the kurtosis (Ku), a measure of the tailedness of a distribution relative to the normal distribution, defined as follows

$$H_s = 4\sigma^{1/2} \tag{2.18}$$

$$As = \langle \mathbb{H}(\eta - \langle\eta\rangle)^3\rangle/\sigma^{3/2} \tag{2.19}$$

$$Sk = \langle(\eta - \langle\eta\rangle)^3\rangle/\sigma^{3/2} \tag{2.20}$$

$$Ku = \langle(\eta - \langle\eta\rangle)^4\rangle/\sigma^2 - 3 \tag{2.21}$$

where $\sigma = \langle(\eta - \langle\eta\rangle)^2\rangle$ is the free surface variance, $\langle\ \rangle$ the time averaging operator, i.e, $\langle f\rangle = \frac{1}{t_f - t_i}\int_{t_i}^{t_f} f(t)dt$, and $\mathbb{H}$, the Hilbert transform. For example, a linear Gaussian sea state would have $As = 0$, $Sk = 0$, and $Ku = 0$.

Fig. 2.12 shows that there is a good agreement between the simulated and measured wave statistics for all wave characteristics. More specifically, Fig. 2.12a shows that H_s increases up to the onset of wave breaking at $x \simeq 12$ m, then decreases during breaking over the bar crest ($12 < x < 14$ m), and remains roughly constant for $x > 14$ m. Fig. 2.12b shows that wave asymmetry is maximum at breaking onset ($x \simeq 12$ m) and decreases during wave breaking. Finally, Figs. 2.12c,d shows that the skewness and kurtosis, which quantify the wave nonlinearity, gradually increase during shoaling and breaking, and then decrease during deshoaling, after the bar. Both of these statistics agree better with the experiments than the results reported by Simon et al. (2019), who

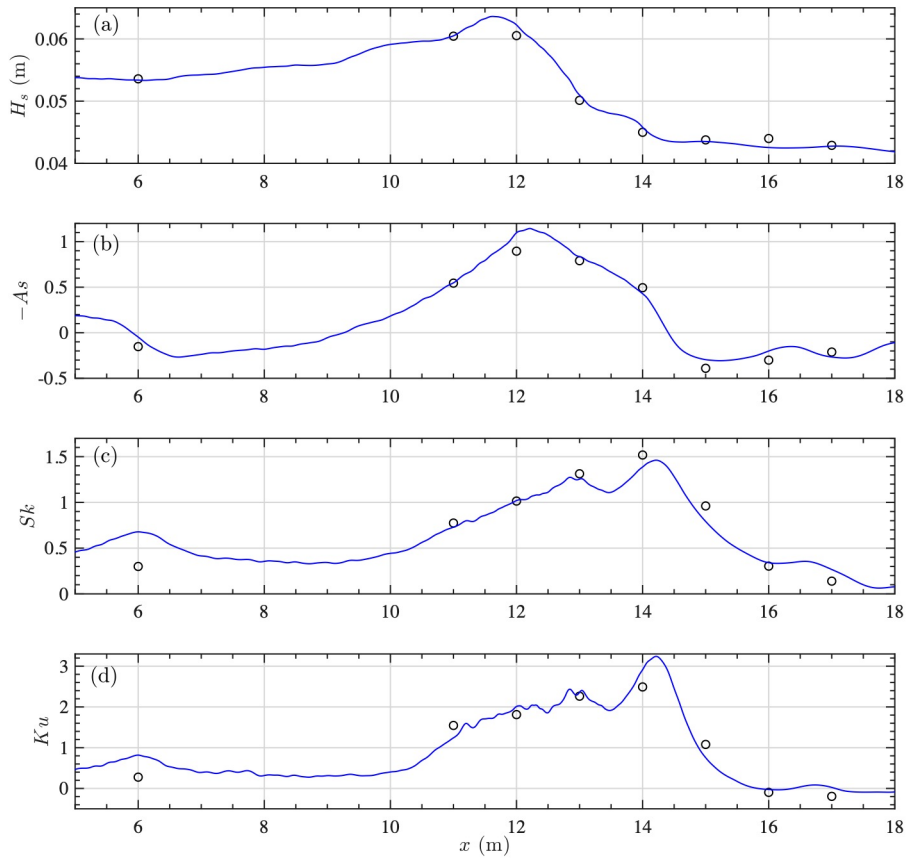

Figure 2.12: Spatial evolution of wave statistics computed from the experiments (circles) and simulations with Mis-b005 (solid line) for the irregular wave case of Beji & Battjes (1993) (JONSWAP spectrum with $H_s = 0.049$ m and $T_p = 2.5$ s). Waves break over the bar in the model and in the experiments (plunging breakers).

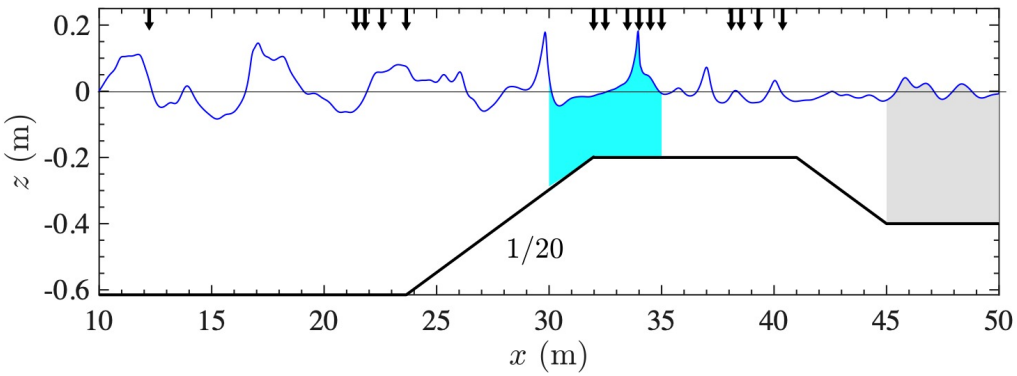

Figure 2.13: Set-up for simulations with Misthyc of Adytia et al. (2018) experiments for irregular waves propagating over a bar ($H_s = 0.2$ m and $T_p = 2.5$ s), with arrows showing the location of the 15 wave gauges. The cyan shading shows the breaking region from onset to termination, and the gray shading indicates the absorbing beach region.

also simulated this test case using Misthyc with the HJ dissipation and an eddy viscosity model (Kurnia & van Groesen 2014) in combination with several breaking onset criteria that were not based on B.

2.4.2.5 Irregular waves breaking over a bar - Adytia et al. (2018)

Adytia et al. (2018) also performed experiments with irregular waves propagating and breaking over a submerged bar with a different geometry than BB's (referred to as AH). Irregular incident waves were generated with $H_s = 0.2$ m and $T_p = 2.5$ s, in a constant depth $h_0 = 0.615$ m. Fig. 2.13 shows the Misthyc model set-up, with the bar having a 1/20 offshore slope with the toe located at $x = 23.65$ m and extending up to $x = 31.98$ m, followed by a constant depth crest with $h = 0.2$ m, to $x = 41$ m. Time series of the free surface elevation were measured at 15 wave gauges, with the locations indicated with arrows in Fig. 2.13. As in the BB-irregular test case, the free surface elevation measured at the gauge located at $x = 11.5$ m is used to calculate the incident waves conditions for the simulation (based on a FFT).

The simulation is run for 500 s or 200 peak periods, and breaking onset occurs at $x_b \in [30,\ 32]$ m. The same wave statistics as in the previous application are computed here based on experimental measurements and simulations with the Misthyc model, using $b = 0.05$. These are shown in Fig. 2.14 where, overall, there is a good agreement between the experiments and simulations. Fig. 2.14a shows that H_s gradually increases over the offshore slope of the bar until wave breaking begins over the bar crest, then decreases in the breaking region ($30 < x < 35$ m), and finally remains constant for $x > 35$ m to the end of the bar crest. A similar trend is observed in asymmetry as in the BB-irregular test case in Fig. 2.14b: an increase up to the onset of breaking, a decrease in the breaking region, and a roughly constant value afterwards. Although the variation of skewness and kurtosis are reproduced better in the breaking region compared to Simon et al. (2019), some differences are seen in the post-breaking region (see Figs. 2.14c,d).

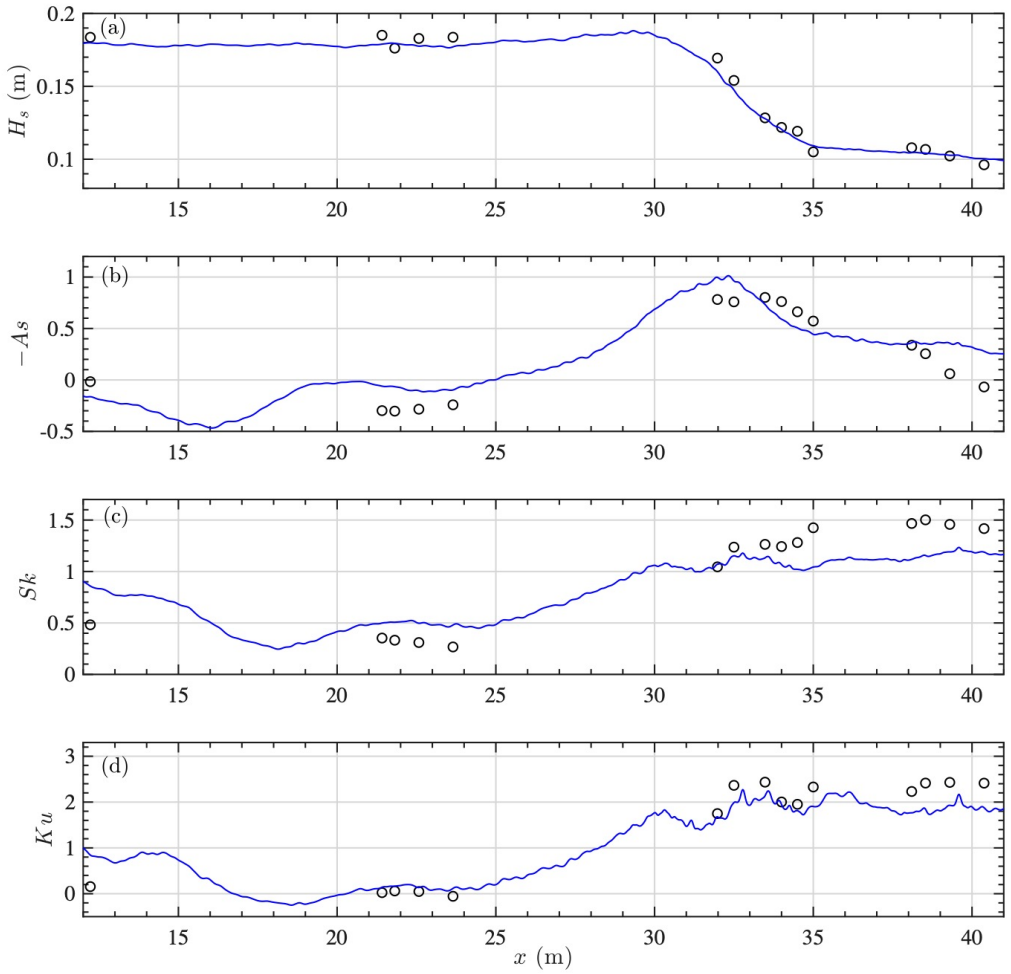

Figure 2.14: Spatial evolution of wave statistics computed based on results of experiments (circles) and simulations with Mis-b005 (solid line) for the irregular wave case of Adytia et al. (2018) ($H_s = 0.2$ m and $T_p = 2.5$ s); waves break over the bar in the model and in the experiments.

2.5 Discussion

In the previous section, the results of simulations using one or both FNPF models with the newly proposed breaking onset/termination and dissipation parameterizations were presented, for standard experimental benchmarks from the literature (referred to as HS, BB, TK and AH) featuring regular or irregular waves propagating and breaking over several mild beach slopes and bars. In each case, the type of breaking (spilling-S or plunging-P) was reported in the experiments, as well as the measured breaking index value $\kappa_{be} = (H_b/h_b)_e$ for some cases. Overall, the simulation results agreed well with the experimental data, confirming that the breaking onset criterion ($B = 0.85$) proposed by Barthelemy et al. (2018) is accurate, and wave elevation and kinematics at breaking onset and during breaking are accurately simulated in the models using the absorbing pressure and the proposed parameterizations of the energy dissipation rate.

Table 2.3 summarizes, for the periodic wave cases reported in the HS, BB-regular and TK studies, the incident wave and bathymetric parameters specified in the models and experiments: (H_0, T), offshore slope S, and wave characteristics simulated at breaking onset (T_b, c_b, κ_b). Note the breaking period used in the definition of γ, $T_b < T$ is based on the breaking crest geometry, following Derakhti et al. (2020). In addition to the test cases described in detail in Section 2.4.2, additional simulations were performed for periodic wave cases from two more studies by Narayanan & McCalpin (1997) (NM) and Blenkinsopp & Chaplin (2007) (BC), whose parameters and results are also summarized in Table 2.3. For each case, the Table also lists the value of Battjes' surf similarity parameter (or Iribarren number), $\xi_0 = S/\sqrt{H_0/L_0}$, where L_0 is the incident wavelength in deep water, $L_0 = gT^2/(2\pi)$ (Battjes 1974). Battjes showed that periodic waves shoaling over a plane slope break as spilling breakers for $\xi_0 \leq 0.5$ and as plunging breakers for $0.5 < \xi_0 \leq 3.3$. In all of the experiments reported in Table 2.3, waves broke either as spilling or plunging breakers, except in one case (c: S/P-BC) where both were observed. In most cases, the ξ_0 value is consistent with the observed type of wave breaking, despite some of these experiments being performed over a bar and not just a plane slope. Consistent with Battjes's work and predictions based on the surf similarity parameter for periodic depth-limited breakers, the models predicted a breaking index $\kappa_b \in [0.7,\ 1.2]$ for the tests considered here. In the next section, the dependence of the breaking strength b predicted using the HJ model on the instantaneous $\kappa \simeq 2F$ values in the breaking area is examined.

2.5.1 HJ model breaking strength

For the HJ model, the instantaneous breaking strength parameter b can be computed in each case using Eq. (2.13) and expression of ϵ in Eq. (2.15), assuming $\Pi_b = \epsilon$. As shown in Eq. (2.14), assuming small amplitude waves (i.e., a small F) yields $b \simeq 2\mu F^3$ with $F = ga/c_\ell^2 \simeq a/d$ and $c_\ell \simeq \sqrt{gd}$ in shallow water. Since waves tend to not be symmetric about the mean water level, this equation underestimates the product $h_c h_t$ in Eq. (2.13), and therefore overestimates the non-dimensional breaking strength compared to using the complete formula. Therefore, the value predicted this way represents an upper bound, i.e., $b_{max} = 2\mu F^3$. Now, noting that in Eq. (2.13)

Label	Name	H_0 (cm)	T (s)	slope S	T_b (s)	c_{lb} (m/s)	κ_b	κ_{be}	γ	ξ_0
a	M-S-HS	9.50	1.0	1/34.26	0.78	1.03	0.73	0.78	0.77	0.118
b	M-S-TK	12.50	2.0	1/35	1.33	1.26	0.81	0.82	0.80	0.202
c	N-S/P-BC	10.05	1.0	1/10	0.75	1.06	0.69	0.87	1.01	0.394
d	N-S-NM	12.00	2.0	1/34.66	1.23	1.31	0.84	-	1.12	0.208
e	N-P-NM	12.00	5.0	1/34.66	1.54	1.24	1.09	-	1.54	0.520
f	M-S-BB	4.40	2.5	1/20	0.82	0.89	0.79	-	1.30	0.744
g	N-P-TK	12.80	5.0	1/35	1.71	1.27	1.09	1.21	1.65	0.499
h	N-P-BC2	9.72	1.42	1/10	1.04	1.07	0.95	0.91	1.43	0.569
i	M-P-BB	5.40	2.5	1/20	0.99	0.92	0.92	-	2.47	0.672
j	N-P-BC1	7.82	2.0	1/10	1.64	1.04	1.17	0.84	1.52	0.894

Table 2.3: Periodic wave breaking test cases and their parameters. Each test case name has 3 parts: (1) the model used, M-Misthyc, N-NWT; (2) type of breaking reported in experiments, S-Spilling, P-Plunging; and (3) the experiment: (slope) HS-Hansen & Svendsen (1979), TK-Ting & Kirby (1994), NM-Narayanan & McCalpin (1997) and BC-Blenkinsopp & Chaplin (2007), and (bar) BB-Beji & Battjes (1993).

we always have, $h_c h_t < (d+2a)^2 = (1+2F)^2 d^2$, replacing the latter value in the equation yields a lower bound of the breaking strength, i.e., $b_{min} = b_{max}/(1+2F)^2$. As the energy dissipates during the breaking process, the relative depths under the crest and trough, h_c and h_t, change, and therefore the exact value of b will vary, roughly bounded by these approximations, until the breaking termination criterion is met.

Fig. 2.15 shows the breaking strength b computed with the Misthyc model, using the HJ parameterization, as a function of $\kappa(t) = H/d \simeq 2F$, for the HS, TK, and BB-regular periodic wave experiments, as well as its approximate lower and upper bounds, $b_{min} = (\mu/4)\kappa^3/(1+\kappa)^2$ and $b_{max} = (\mu/4)\kappa^3$, respectively. Breaking onset is at the right side of the figure, where the largest values of b, κ and F occur and, moving to the left of the figure, the waves propagate through the breaking region as a function of time, with breaking termination occurring near the bottom left. The model results for b are in the range $[0.01,\ 0.1]$ and fall mostly within its previously defined lower and upper bounds, estimated based on F values. As expected, at breaking onset, $\kappa_b = H_b/h_b$ is in the range $[0.7,\ 1.2]$ (Table 2.3).

These observations, as well as the good agreement between the simulations and experimental observations for a variety of benchmark cases, confirm the relevance of modeling the energy dissipation rate for depth-induced breaking waves as analogous to that of a hydraulic jump (or bore), with a single calibration constant $\mu = 1.5$ (Svendsen et al. 1978 and Stive 1984; Eq. (2.13)). Furthermore, unlike in earlier studies that used a variety of case specific breaking criteria and related energy dissipation rates, good agreement with all experiments reported here for spilling and plunging breaker cases was achieved using universal breaking onset and termination criteria based on B and a dissipation rate based on the HJ analogy. Fig. 2.15 also shows that the time-averaged breaking strength, based on all simulated cases, is $b \simeq 0.05$, as tested in several simulations in Section 2.4.2. And although the actual b value differs substantially from this av-

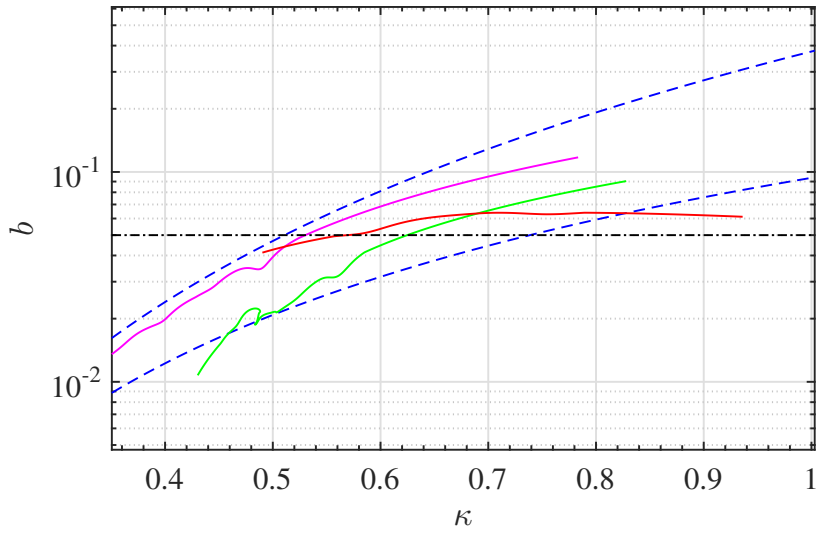

Figure 2.15: Evolution of the instantaneous breaking strength b calculated with the HJ model during breaking simulations with Misthyc for the (Table 2.3): (a) HS (solid magenta), (b) TK (solid green), and (i) BB-regular (solid red) periodic spilling/plunging breaking wave experiments, as a function of $\kappa = H/d$. The dashed blue curves represent the lower (b_{min}) and upper (b_{max}) bounds estimated for b, and the horizontal dash-dotted black line is $b = 0.05$.

erage near breaking onset and termination, as seen in earlier results, there were no significant differences in the results obtained with a constant $b = 0.05$ or varying b value throughout breaking within the accuracy/variability of most experiments, and both approaches agreed similarly with the experiments for the 5 considered benchmark cases.

2.5.2 Breaking onset kinematics

Fig. 2.16 shows the time evolution of the B value up to breaking onset ($B = 0.85$), as computed in simulations of the 10 experimental cases listed in Table 2.3. As expected from the parameterization of b as an increasing function of $\gamma \propto dB/dt$, defined in Eq. (2.17) (Fig. 2.3), dB/dt is observed to be larger at breaking onset for plunging breakers than for the spilling breakers. This observation appears to be independent from the type of bathymetry that caused waves to break. For instance, BB and TK conducted S and P breaker experiments on barred and sloped bathymetries, respectively, and dB/dt is larger for P than for S breakers in all cases. Blenkinsopp & Chaplin (2007) conducted three types of experiments, for strongly P (BC1), P (BC2), and S/P (BC) breakers and, among these, dB/dt is largest for BC1 and lowest for BC, as would be expected.

For the cases shown in Table 2.3, the S breakers, with $\xi_0 < 0.7$ have $\gamma < 1.3$ and the P breakers, have $\xi_0 > 0.5$ and $\gamma > 1.4$. Hence, consistent with the value of dB/dt at breaking onset, γ values may also distinguish S from P breakers. However, a more accurate estimation of this threshold γ value should be based on a larger number of test cases.

$\Delta x\ (m)$	$\Delta t\ (s)$	$(t_f - t_b)/T$	$\epsilon_b = \int_{t_b}^{t_f} \Pi_b dt\ (m^4/s^2)$
0.0385	0.02	0.58	0.049
0.0385	0.01	0.70	0.0491
0.0256	0.013	0.68	0.050
0.0192	0.01	0.67	0.0476
0.0154	0.008	0.55	0.0439
0.0128	0.006	0.56	0.0437

Table 2.4: Sensitivity of the breaking model to the discretisation for the TK test case using the Misthyc model. Here, $t_f - t_b$ is the duration of breaking, T, the time period, and ϵ_b the total energy dissipated per unit length of a quasi-steady breaking crest.

The computation of breaking onset B is sensitive to small changes in u and c. Thus, a high-order interpolation scheme was used to track wave crests, but errors may still appear as a function of the discretization, which may delay or advance the onset of breaking, thus affecting the energy dissipation. These effects were evaluated by simulating the TK test case with six increasingly refined grids listed in Table 2.4. For the time duration of breaking, results yield a standard deviation of $0.062T$, where $T = 2\,\mathrm{s}$, and for the resulting total energy dissipated per unit length of the breaking crest (ϵ_b), the standard deviation is $0.0025\,\mathrm{m}^4/\mathrm{s}^2$, that is, less than $0.05\epsilon_b$. In both cases, the observed values for the two finer discretizations are nearly constant, indicating convergence.

2.5.3 Breaking termination conditions

For waves breaking on a plane beach (such that depth always decreases as waves propagate into shallower water), as described in Svendsen et al. (1978), from breaking onset shoreward, the breaking dissipation can occur up until waves run up the dry upper slope. However, the FNPF setup used here does not model wave run-up or bottom friction, which becomes significant near the shoreline. Using a similar model set-up, simulations in previous work on plane beaches did not use a breaking termination criterion. For example, in Fig. 9a from Grilli, Horrillo & Guignard (2020), the wave height decreases from the onset up to the shallowest depth. For the cases on a plane slope, this is also seen in Fig. 10 of Simon et al. (2019), where the same variation in H_s is observed. Finally, Papoutsellis et al. (2019) also mention that for the spilling breaker case of Ting & Kirby (1994), they terminate breaking inside the sponge layer.

In contrast, for waves breaking over a bar, which is followed by deshoaling over the shoreward slope of the bar, a breaking termination criterion $B_{\text{off}} = 0.30$ was used in all of the present applications. As shown in Fig. 2.11, this value appears to be optimal for reproducing the experimental results. Waves breaking on a bar may terminate breaking over the crest or on the shoreward slope of the bar. Here, the choice of termination criterion is important since the wave evolution depends strongly on it.

To the authors' knowledge, a universal breaking termination criterion does not exist. Alternative

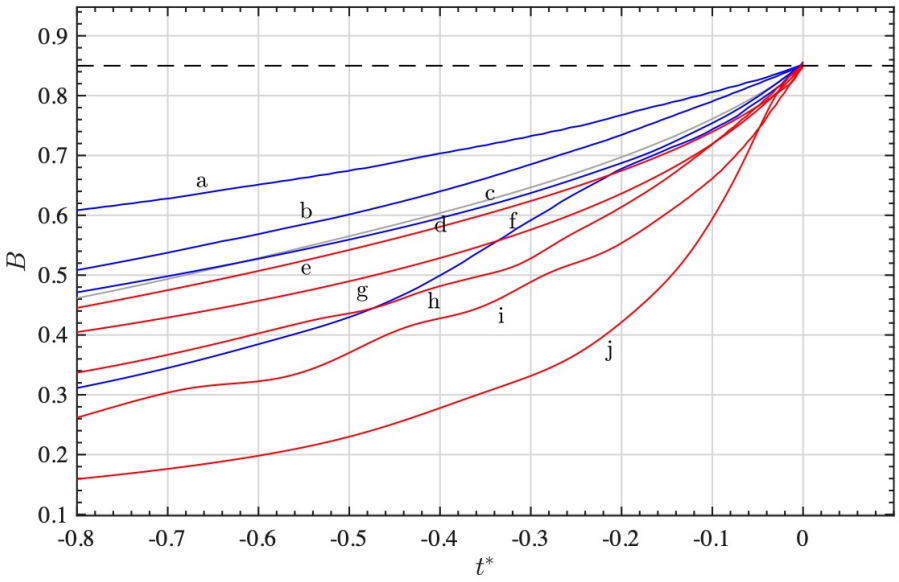

Figure 2.16: Evolution of $B = u/c$ as a function of non-dimensional time $t^* = (t - t_b)/T_b$, referred to the time of breaking onset, up to breaking onset ($B = 0.85$; horizontal dashed line), computed for a wave crest evolving over sloping bathymetries in the experimental test cases listed in Table 2.3. Red lines for P-cases and blue lines for S-cases have larger and smaller values of dB/dt at breaking onset, respectively.

ideas have been tested, such as a termination criterion based on the slope of the free-surface (e.g., Simon et al. 2019). Another possibility is a time-based criterion. Derakhti, Banner & Kirby (2018) noted that the active breaking period $\tau \approx 0.75T_b$, and so this could also be tested in future applications.

2.6 Conclusions

A unified method of modeling depth-limited wave breaking dissipation in FNPF models was demonstrated, building on the work of Guignard & Grilli (2001) and Grilli, Horrillo & Guignard (2020), who proposed making the energy dissipation rate analogous to that of a hydraulic jump. Two different FNPF models were applied here: Misthyc (Yates & Benoit 2015) and a BEM-NWT (Grilli et al. 1989, Grilli & Subramanya 1996). The detection of breaking onset in the models was based on the universal criterion $B = u/c = 0.85$, first proposed by Barthelemy et al. (2018) for deep and intermediate water cases, and validated by Derakhti et al. (2020) in shallow water. Similar to earlier work such as Grilli, Horrillo & Guignard (2020) or Simon et al. (2019), we show that simulation results based on this approach agree well with experimental measurements for a variety of standard shallow water breaking cases from the literature, for both regular and irregular wave trains and different bathymetries.

Using the hydraulic jump (HJ) analogy originally proposed by Svendsen et al. (1978) and Stive (1984) for spilling breakers, the non-dimensional breaking strength b, is found in most cases,

including both spilling or plunging breakers, to have a fairly narrow range of variation centered on 0.05. However, consistent with the recent parameterization of b proposed by Derakhti, Banner & Kirby (2018), Derakhti, Kirby Jr, Banner, Grilli & Thomson (2018), proportional to dB/dt at the onset, the instantaneous value of b resulting from the HJ analogy is much larger at breaking onset, and then decreases throughout the breaking region. Recalling that the HJ dissipation rate is related to the relative wave height κ, or wave Froude number F, with $\kappa = H/d \simeq 2F$ in shallow water and for the depth-limited breaking waves tested here, $\kappa_b \in [0.7,\ 1.2]$, consistent with Battjes' predictions based on the surf similarity parameter (Battjes 1974). This implies that for waves in this parameter range, b would always have a similar order of magnitude. With this rationale, simulations of spilling and plunging depth-limited breaking waves were performed using a constant breaking strength $b = 0.05$. The simulated results using a constant b or the HJ model with a time-varying b agreed similarly with the experimental measurements, within the range of experimental uncertainty. Although in very complex cases there may be waves in an irregular wave train requiring larger or smaller b values, the constant b value provides results with a similar level of uncertainty or accuracy as the HJ model.

There are some weaknesses in this current approach that must be resolved in order to obtain a fully general method. While concentrating on the wave breaking criterion and dissipation rate, the breaking termination criterion has not yet been thoroughly investigated, which should be a point for further research. For the cases shown here, wave breaking on a slope were not terminated until the shallowest depth in the model domain (or the absorbing beach) were reached, whereas wave breaking on a bar was terminated at a value $B_{\text{off}} = 0.30$, which was found to yield results in good agreement with experiments. Since the energy dissipation rate $\Pi_b = \epsilon$ of breaking waves depends on the fifth power of wave celerity, when this parameterization is used in the constant strength model, an accurate tracking of wave crest locations as a function of time $x_c(t)$ and the calculation of the time derivative $dx_c/dt = c$ are important for accurate simulations. With the method used here to compute c (see Appendix), some spurious oscillations are still observed when taking the derivative of the crest position, which results in small oscillations of $\Pi_b = \epsilon$ and thus wave heights in the breaking region. Another issue is the accurate real-time identification of wave crests/troughs in irregular sea-states. In situations where small breaking waves ride on top of larger waves, the estimation of the spatial extent of dissipation could be misinterpreted, which could cause instabilities.

By using a breaking dissipation rate $\Pi_b = \epsilon$ proportional to a constant b, instead of using the HJ analogy, the need to compute the local geometric characteristics of waves required in the HJ dissipation Eq. (2.13) is eliminated (e.g., water depth under the trough, etc.), and the dissipation can simply be related to the crest kinematics. This simpler formulation clearly will yield its greatest advantages when applying the model in three-dimensions, where the identification of local wave parameters, even the crest location, is challenging. Derakhti, Kirby Jr, Banner, Grilli & Thomson (2018) also showed that a constant b might be expected in shallow water based on results of a Navier-Stokes model. The present modeling approach with the constant strength b and dissipation rate $\Pi_b = \epsilon$ parameterization could be generalized to intermediate or deep water cases, by using the $b(\gamma)$ breaking strength model proposed by Derakhti, Banner & Kirby (2018),

who found that the value of b in deep or intermediate water (which is clearly not constant) could be related to the kinematics of the wave as well, specifically to dB/dt and a relevant breaking period T_b at breaking onset. Some additional work may be required, however, to implement the deep-water parameterization, as b obtained from a 3D finite volume NS solver, in which energy is dissipated within the domain volume, may not have the same distribution or effect in a FNPF model, where the energy dissipation is applied to the surface and only acts on the potential part of the flow.

In considering the kinematics of the shallow water breaking waves simulated here, the value of γ appears to provide a parameter to distinguish spilling and plunging breakers, with a threshold value around $1.3 - 1.4$. For waves shoaling on a plane slope, this may be loosely related to Battjes' surf similarity parameter and may be of interest for applications beyond the scope of those envisioned here, such as of identifying breaker types from existing models that are unable to simulate the breaking process.

Appendix 1: Calculation of wave crest kinematics

The instantaneous location of wave crests is first roughly estimated on the 2D-FNPF models' free surface, by finding local maxima. (The crests with wave height, $H < 0.05d$, where d is the depth at the wavemaker, are discarded, as these are mostly flat and the calculation of c gets very noisy.) Then, four model points surrounding each wave crest location are identified with elevation, particle velocity, and location (η_i, u_i, x_i) $(i = 1, 2, 3, 4)$ and mapped to a local coordinate $\xi \in [-1,\ 1]$. Cubic shape functions (Eq. 2.22) are used to interpolate $\eta(\xi)$ between these points.

$$\begin{aligned} N_1(\xi) &= \frac{1}{16}(1-\xi)(9\xi^2-1) \\ N_2(\xi) &= \frac{9}{16}(1-\xi^2)(1-3\xi) \\ N_3(\xi) &= \frac{9}{16}(1-\xi^2)(1+3\xi) \\ N_4(\xi) &= \frac{1}{16}(1+\xi)(9\xi^2-1) \end{aligned} \tag{2.22}$$

The wave crest location is then estimated based on the ξ_c value at which $d\eta/d\xi = 0$ (Fig. 4.1). Therefore, the horizontal location of a local crest in the global coordinate is calculated as

$$x_c = x_1 N_1(\xi_c) + x_2 N_2(\xi_c) + x_3 N_3(\xi_c) + x_4 N_4(\xi_c), \tag{2.23}$$

and the horizontal particle velocity at the crest, u as

$$u = u_1 N_1(\xi_c) + u_2 N_2(\xi_c) + u_3 N_3(\xi_c) + u_4 N_4(\xi_c). \tag{2.24}$$

Prior to calculating c, $x_c(t)$ is smoothed by second-order exponential smoothing (Guthrie 2020),

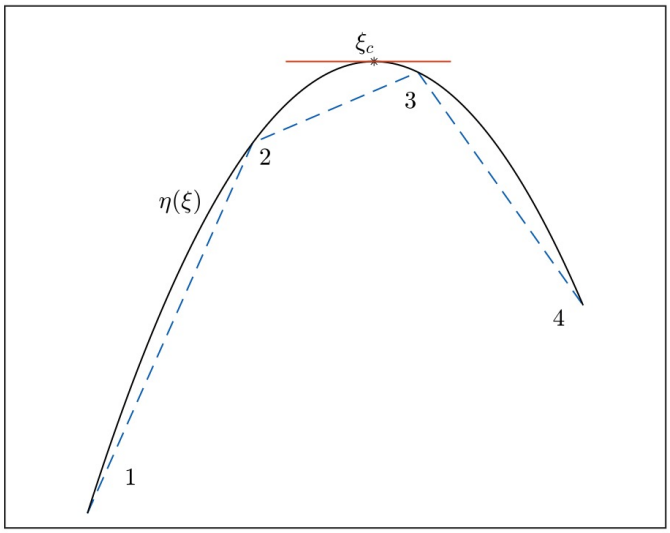

Figure 2.17: Sketch showing the calculation of a local wave crest location between discretization points on the simulated free surface.

described as follows, denoting X_c^t as the smoothed horizontal crest location at time $t = 0$,

$$\begin{aligned} X_c^0 &= x_c^0 \\ s^0 &= x_c^1 - x_c^0 \end{aligned} \tag{2.25}$$

For $t > 0$,

$$\begin{aligned} X_c^t &= \alpha x_c^t + (1-\alpha)(X_c^{t-1} + s^{t-1}) \\ s^t &= \beta(X_c^t - X_c^{t-1}) + (1-\beta)s^{t-1}, \end{aligned} \tag{2.26}$$

where $(\alpha,\ \beta)$ based on some preliminary tests are taken as $(0.05,\ 0.01)$.

Wave celerity of a crest at a time t, $c(t)$ is then calculated by a linear fit to the smoothed data in the interval $[X_c^{t-n}, ..., X_c^t]$, such that $n\Delta t < 0.04T$, where Δt is the discretization in time and T is a representative wave period. In the test cases presented this study, $n = 8$. The location of a crest X_c^t at the previous time i.e, X_c^{t-1} is determined by comparing all the crests at $(t-1)^{th}$ time step to that of X_c^t such that $X_c^t - X_c^{t-1} < m\Delta x$, where $m \in [10,\ 20]$ and Δx, the discretization in space (Note, Δx and Δt in the test cases here are chosen such that a crest horizontally does not advance more than a few Δx). This gets challenging for irregular test cases when small waves are present on top of longer waves, for the cases seen here, Δx and m are small enough such that crests are correctly tracked. To compute γ, the discrete values of $B = u/c$ at the crest, when in the range $[0.82,\ 0.85]$, are then linearly fit to obtain $dB/dt|_{B=B_{th}}$.

Acknowledgements

This research was produced within the framework of Energy4Climate Interdisciplinary Center (E4C) of IP Paris and Ecole des Ponts ParisTech. This research was supported by 3rd Programme

d'Investissements d'Avenir [ANR-18-EUR-0006-02]. This action benefited from the support of the Chair « Challenging Technology for Responsible Energy » led by l'X – Ecole Polytechnique and the Fondation de l'Ecole Polytechnique, sponsored by TotalEnergies.

SG is gratefully acknowledging support from the US National Science Foundation grant #OCE-19-47960. The authors thank Dr. S. Husrin for providing laboratory data from the DFG-TAPFOR project, of irregular breaking waves. The authors also thank Luc Pastur (ENSTA Paris) and Christophe Peyrard (EDF R&D LNHE) for helpful discussions.

CRediT authorship contribution statement

Sunil Mohanlal: Methodology, Writing – original draft, Validation, Formal analysis, Visualization. **Jeffrey C. Harris:** Methodology, Writing – review & editing, Supervision, Formal analysis, Funding acquisition. **Marissa L. Yates:** Methodology, Writing – review & editing, Supervision, Formal analysis, Funding acquisition, Software. **Stephan T. Grilli:** Methodology, Writing – review & editing, Formal analysis, Software.

Chapter 3

Steepness-limited wave breaking model

Le déferlement des vagues à cambrure limitée est simulé dans un modèle d'écoulement potentiel non linéaire et validé avec des données des essais en laboratoire. Le début de déferlement est basé sur le rapport de la vitesse horizontale des particules à la crête u, par rapport à la vitesse de phase c, $B = u/c > 0.85$. Un modèle de dissipation de déferlement, dans lequel le paramètre d'intensité du déferlement non-dimensionnel est prédit sur la base de la cambrure des vagues linéaires, est utilisé. Un nouveau modèle de dissipation variable en fonction du temps est testée, et le critère de fin de déferlement est étudié.

3.1 Introduction

In deep-water conditions, where wave propagation is not influenced by bathymetric effects, the phenomenon of wave shoaling does not exist. The manifestation of breaking waves in shallow conditions, as observed in Chapter 2, was attributed to this phenomenon. Unlike in shallow water where wave celerity is primarily governed by the water depth ($c = \sqrt{gd}$), in deep water, the wave celerity is primarily governed by its wave period (or frequency), given by $c = g/(2\pi f)$. In deep-water seas, irregular waves are generally observed, which can be described as a superposition of monochromatic waves of different frequencies and wave heights. Therefore, there exist some sea states where several of these monochromatic waves positively superimpose (addition of amplitudes of the individual waves) reaching larger wave heights, which may eventually become unstable and break.

In laboratory conditions, deep-water breaking events are often studied by generating a chirped wave packet (focused waves). A chirped wave packet, meaning a group of waves of different frequencies, is generated by a wavemaker, in an order such that high-frequency waves (lower phase speed) are generated first, followed by low-frequency (higher phase speed) waves. The intention is for the faster waves to eventually catch up with the slower waves, resulting in a positive combination of the individual wave amplitudes. This superposition in space and time is controlled by the phase angle of the individual input waves.

In this Chapter, a dissipation model designed for steepness-limited breaking waves is presented. The breaking onset is based on the criterion $B = 0.85$, as in the depth-limited wave breaking model (Chapter 2). The proposed dissipation model is based on determining the breaking strength (b) with respect to the input maximum linear wave steepness (S) proposed by Romero et al. 2012, who obtained this empirical relation by examining several focused breaking waves. A termination criterion is calibrated based on the free surface comparisons from NWT and experiments. The proposed dissipation model is validated with the experimental data collected by Lili Kimmoun from a wave flume at the Ecole Centrale Marseille (ECM).

3.2 Experimental setup

The wave flume at ECM (Fig. 1.6) has a constant water depth of $h = 0.667\ m$. In contrast to the conventional flap-type wavemaker, where the axis of rotation is fixed at the bottom, the wave flume at ECM employs a unique configuration with the axis of rotation positioned $0.4\ m$ below the bottom of the wave flume (see Fig. 3.1 for a detailed schematic of the flap), and a wall at $x = 12.535\ m$. Focused waves are generated by the wavemaker based on a discrete Ricker spectrum, (which corresponds to a modified second derivative of the Gaussian function, as the exponent, $m < 2$) of 2^{12} components given by,

$$s(\omega) = H\sqrt{T}e^{-\omega^m T}[1 - a(\omega^m T - 1)],\ a = \frac{1}{\omega_p^m T - 2} \tag{3.1}$$

where $\omega_p = 2\pi/T_p$ is the peak angular frequency, H is a design wave height, and m and T are spectral design parameters. This spectrum is also used in the works of Kimmoun et al. 2010, Lubin et al. 2019, and Steer et al. 2021. From this spectrum, the angular displacement of the flap is calculated as,

$$\theta(t) = \sum_j \frac{s(\omega_j)}{C(\omega_j)} \sin(\omega_j t - k_j x_f) d\omega \tag{3.2}$$

where x_f is the focusing distance from the wavemaker, k_j is the wave number calculated from the linear dispersion relation, $\omega_j = g k_j \tanh(k_j d)$, and $C(\omega)$ is the linear transfer function given by Kimmoun et al. 2010,

$$C(\omega) = \frac{2\sinh(kd)}{kd + \sinh(kd)\cosh(kd)} \left(\sinh(kd) + \frac{1 - \cosh(kd)}{k(d+l)} \right) \tag{3.3}$$

where l is the distance between the axis of rotation and the actual bottom. A Ricker spectrum and its corresponding angular displacement are shown in Fig. 3.2.

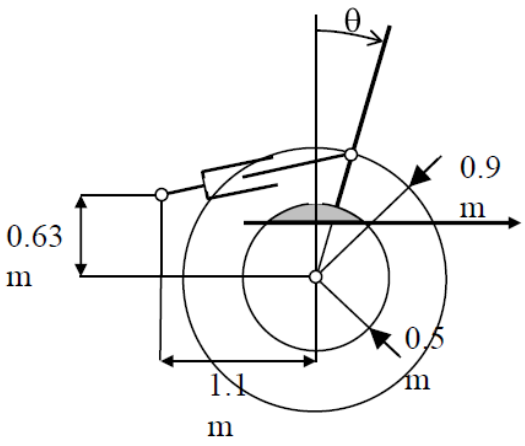

Figure 3.1: Schematic of the flap at the wave flume at ECM (Source: Lili Kimmoun).

To record the experimental data, 6 resistive and 3 capacitive gauges are placed in the flume (shown qualitatively in Fig. 3.3, and tabulated in Table 3.1) with a sampling frequency of 300 Hz. Particle Image Velocimetry (PIV) (see Kimmoun & Branger 2007) and videos of the breaking waves are also recorded.

3.3 Implementations in the numerical model

Due to the need to model the unique kind of wavemaker described in the previous section, the NWT is utilized in this study, as it can model any type of wavemaker motion, by knowing its geometry and kinematics. However, it is also possible to use the Misthyc model in this study in an approximate way by first determining all the wave components from the angular motion of the flap and the transfer function (Eq. 3.3), and then linearly superposing these components over a short distance from free surface close to the wavemaker (called the generation zone) or

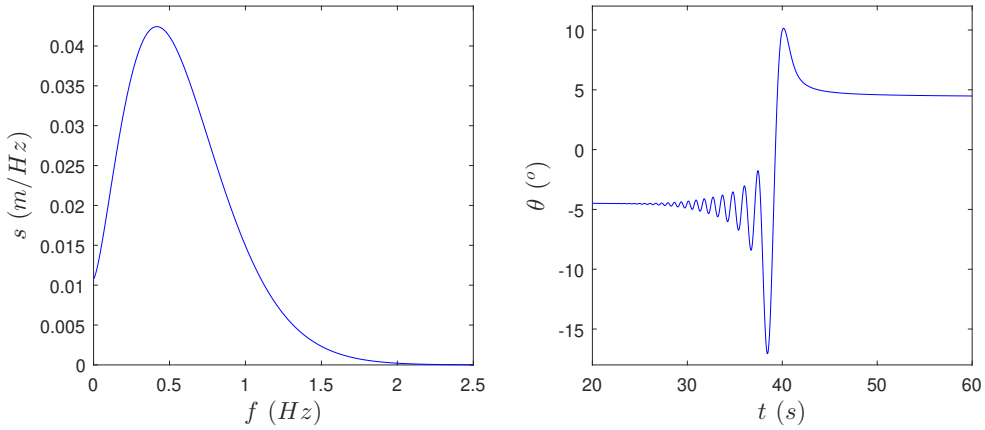

Figure 3.2: A Ricker spectrum (left) and the resulting angular displacement (right) of the flap wavemaker with spectral parameters, $H = 0.2593\ m$, $T = 0.2285$, $m = 1.42$, $\omega_p = 2.61\ rad/s$, and $x_f = 7.5\ m$. Note, in the experiments, for $t > 42\ s$, i.e., the point after which the angular displacement is constant, a sinusoidal ramp in time is prescribed to bring the angular displacement to 0.

N^o	Distance from wavemaker (m)	Type
1	1.21	Resistive
2	5.91	Resistive
3	6.81	Resistive
4	8.03	Resistive
5	8.51	Resistive
6	8.83	Capacitive
7	9.62	Capacitive
8	10.30	Resistive
9	11.32	Capacitive

Table 3.1: Wave gauge location and type in the ECM wave flume (represented by arrows in Fig. 3.3).

by imposing the fluid motion on the vertical boundary as a Dirichlet or Neumann boundary condition.

3.3.1 Modeling the flap wavemaker

A flap as a wavemaker boundary is modeled in the NWT as described by Grilli & Horrillo 1997. The boundary value for the solution of $\nabla^2\phi = 0$, $\frac{\partial\phi}{\partial n}$ and for the solution of $\nabla^2\phi_t = 0$ (solved to get the 2^{nd} order term in the Taylor expansion, for time marching), $\frac{\partial^2\phi}{\partial t\partial n}$, are calculated as

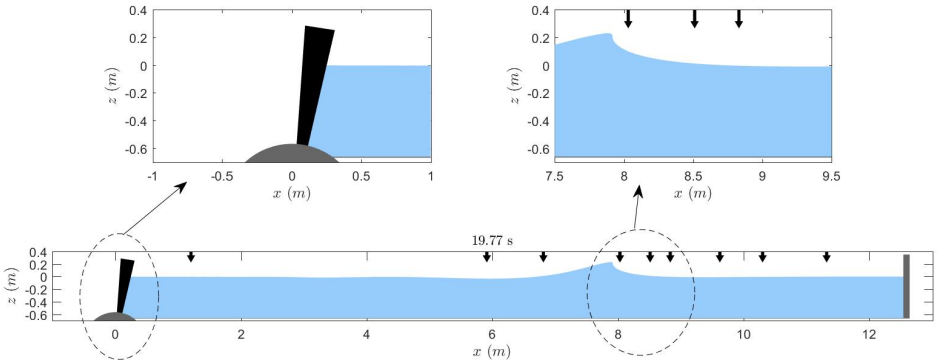

Figure 3.3: A schematic of the numerical wave flume for the focused wave breaking experiments, with a zoomed view of the wavemaker and the focusing region at the top. The arrows on the top of the flume indicate the wave gauge locations (values are given in Table 3.1). A wall is located at the right end of the tank.

follows,

$$\frac{\partial \phi}{\partial n} = r_g \frac{\partial \theta}{\partial t} \tag{3.4}$$

$$\frac{\partial^2 \phi}{\partial t \partial n} = r_g \frac{\partial^2 \theta}{\partial^2 t} + \frac{\partial \theta}{\partial t}\left[r_g \frac{\partial^2 \theta}{\partial^2 s} - \frac{\partial \theta}{\partial s}\right] \tag{3.5}$$

where n, s are the normal and the tangential directions respectively and r_g is the distance between wavemaker nodes and the axis of rotation. The time derivatives of angular displacement are analytically calculated from Eq. 3.2. In Fig. 3.3, an arc (gray bump) connecting the flat bottom and the flap is also seen. This curved Section is considered an impermeable wall, where the normal derivative of the potential, $\frac{\partial \phi}{\partial n}$, is set to zero. To prevent node clustering or stretching, the nodes along this curved arc are regridded equidistantly at each time step, as in Grilli & Subramanya 1996.

3.3.2 Wave breaking model

The construction of the wave breaking model follows a similar approach as described in Section 2.3. The wave breaking onset is based on the criterion $B = u/c = 0.85$, and the termination criterion is calibrated by comparing the free surface elevations measured in the experiments and simulated in the NWT. The notable difference with the depth-limited dissipation model, is in the determination of the breaking strength, b. This modification arises from the consideration that the former method relies on the wave height and water depth ratios, which are not applicable to deep water waves.

Romero et al. 2012 proposed empirical curves for predicting the breaking strength as a function of the maximum input linear wave steepness, $S = \sum_i a_i k_i$, where a_i is the wave amplitude and k_i,

the wave number of the i^{th} component of a focused wave by studying a large set of experimental observations. Two curve fits, one with power $5/2$ and the other with power 3 (Fig. 3.4) were chosen to be consistent with the inertial scaling and measurements of Drazen et al. 2008. Their proposed breaking strength (b_S) is calculated here by,

$$b_S = 0.4(S - 0.08)^{5/2} \tag{3.6}$$

For the range of S of the test cases see here, the difference in b_S with the other formula is less than 5%. This breaking strength is utilized to calculate a damping pressure accounting for wave breaking in the vicinity of the breaking crest, as detailed in Section 2.3.2.1, using the same approach as for depth-limited waves. The specific criteria for terminating wave breaking is discussed in Section 3.4, following the same approach as in Chapter 2.

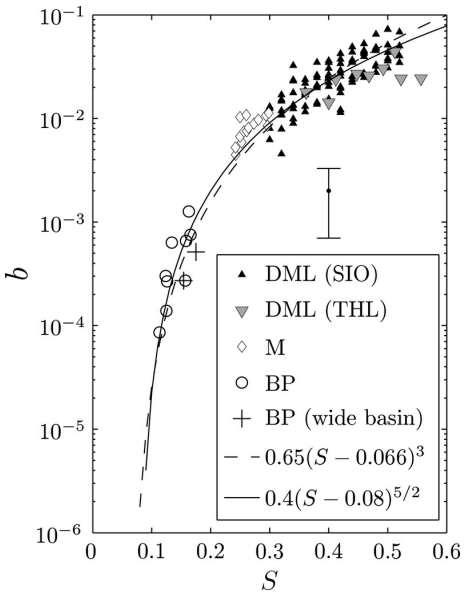

Figure 3.4: Laboratory observations of the dissipation strength b as a function of the predicted maximum linear wave steepness S of the focusing wave (Source: Romero et al. 2012)

3.4 Results

For a Ricker spectrum with parameters $T = 0.2285$, $m = 1.42$, $T_p = 2.4\ s$, three cases with $H = 0.2377\ m$ and $x_f = 7.8\ m$ (denoted as $F1$), $H = 0.2485\ m$ and $x_f = 7.5\ m$ (denoted as $F2$), and $H = 0.2593\ m$ and $x_f = 7.8\ m$ (denoted as $F3$) are simulated. The numerical domain runs for $0 \leq x \leq 12.535\ m$, with $\Delta x = 0.01\ m$, $\Delta t = 0.01\ s$ up to the instant of the maximum angular displacement of the flap, and then $\Delta t = 0.003\ s$ is imposed, to ensure numerical stability close to the wavemaker. At the wall at the right end of the wave flume, the absorbing piston is turned off, and the absorbing beach co-efficient is set to zero, to have a reflecting wall to reproduce the experimental setup (for more information on the absorbing piston and absorbing beach implemented, see Grilli & Horrillo 1997).

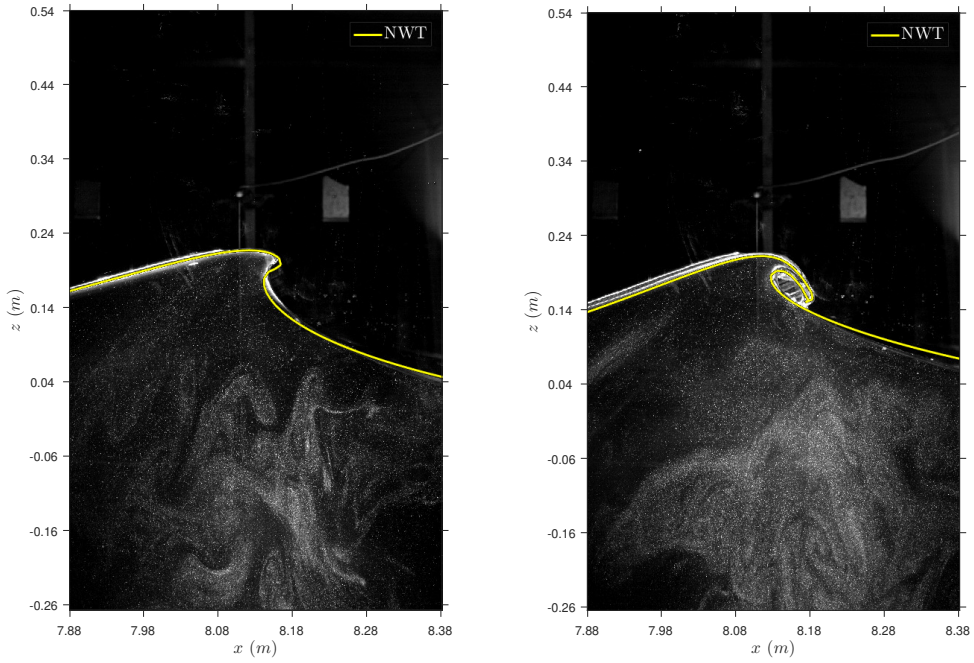

Figure 3.5: Free surface comparison from the experiments and NWT with breaking pressure turned off at an overturning instant ($B > 0.85$) with input conditions, $H = 0.2593\ m$, $x_f = 7.8\ m$ (left) and $H = 0.2485\ m$, $x_f = 7.5\ m$ (right)

Fig. 3.5 presents a comparison between the experimental and NWT free surface profiles at two instances of overturning for the test cases $F3$ (left) and $F2$ (right). The qualitative comparison reveals satisfactory agreement between the two. From a numerical perspective, it is crucial to start wave breaking dissipation prior to free surface overturning, as applying dissipation after this point can lead to numerical instabilities. Thus, it is anticipated that the dissipation in the numerical model should commence before the free surface starts to overturn. From Fig. 3.6, the free surface elevation for the three cases ($F1$, $F2$, $F3$) at the moment of breaking onset is observed, indicated by $B = 0.85$. In all three cases, this moment corresponds to the point where the free surface becomes nearly vertical. Hence, this criterion serves as a reliable predictor of breaking onset.

In Fig. 3.7, a comparison is presented between the time series of free surface elevation at the 9 wave gauge locations obtained from the experiments and the NWT for the test case $F1$. At $x = 1.21\ m$, the gauge close to the wavemaker, the input unfocused chirped wave group is seen for $t < 18\ s$. The wave elevation is then 0 up to $t = 25\ s$, as the flap is almost stationary at this time. Free surface elevations are seen for $t > 25\ s$ due to the reflected waves propagating from the right wall. At the gauges $x = 5.91\ m$ and $x = 6.81\ m$ a partially focused wave (for $t < 20\ s$) is observed, becoming completely focused (with maximum wave elevation) around the gauge at $x = 8.03\ m$. The breaking onset was observed at $x = 7.78\ m$, and the dissipation continued until $x = 8.60$, for a termination criterion of $B_{\text{off}} = 0.4$ (optimal value, discussed in the following paragraph). Overall good agreement is seen with the experiments for the wave

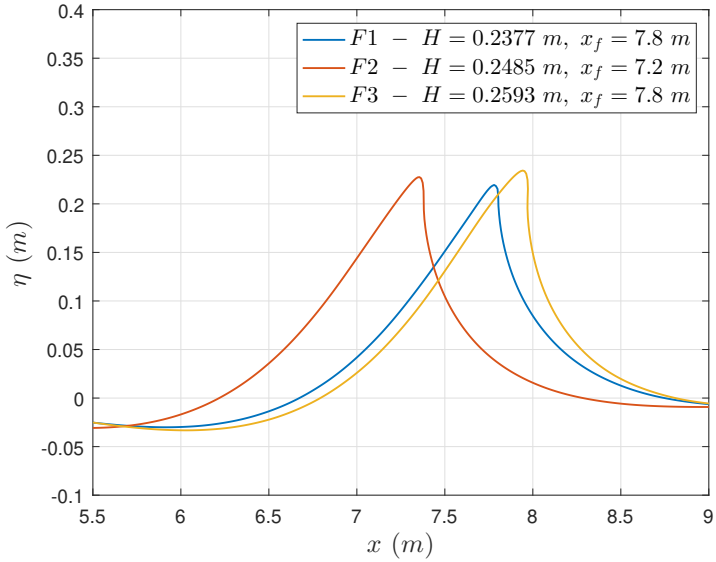

Figure 3.6: The free surface elevation at the instant of breaking onset ($B = 0.85$) for three test cases with different input conditions.

elevations close to the wavemaker, the reflecting wall, and in the breaking region (the gauge at $x = 9.62$ m).

B_{off}	$\overline{\eta^2}\ (cm^2)$		
	$F1$	$F2$	$F3$
Measured	26.04	38.21	45.87
0.10	19.54	32.54	34.71
0.20	23.21	34.39	40.71
0.30	25.54	36.33	44.21
0.40	27.04	37.28	45.41
0.50	27.79	36.98	47.04

Table 3.2: Quantitative comparison of $\overline{\eta^2}$ of the breaking crest from the NWT with different B_{off} and experiments.

To determine the optimal termination criterion, the three test cases, $F1$, $F2$, and $F3$, were run with different termination thresholds, $B_{\text{off}} = 0.1,\ 0.2,\ 0.3,\ 0.4,\ 0.5$. With $B_{\text{off}} = 0.1$ the dissipation is applied for a longer duration as compared to $B_{\text{off}} = 0.5$. The breaking crest at the termination in all these cases was seen before the gauge at $x = 9.62\ m$. Therefore, the wave elevations passing through the gauge at $x = 9.62\ m$ are dependent on how long the dissipation lasted (therefore, the dissipation energy). This information is utilized to compare the free surface elevation at this location with the experiments to see which criterion minimizes the errors. To

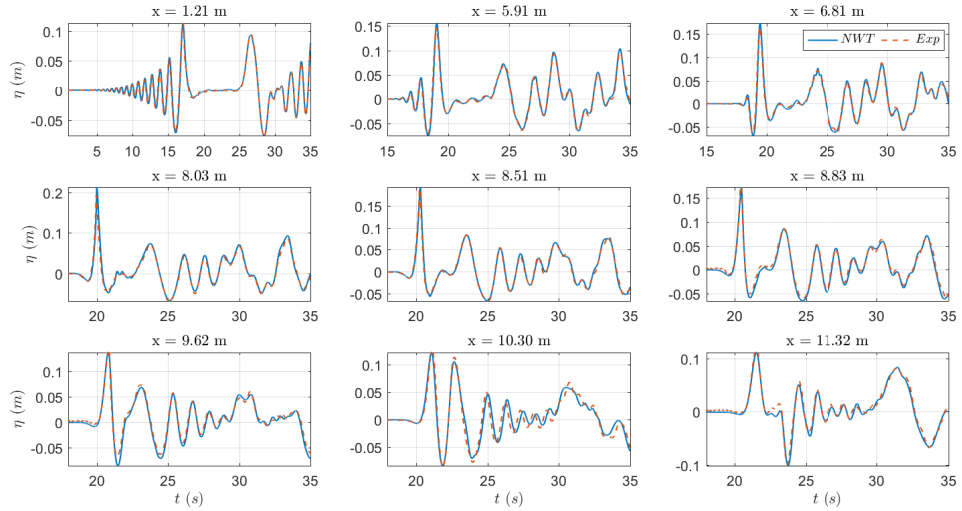

Figure 3.7: Time series comparison of the free surface elevation from the experiments (dashed line) and the NWT (solid line) at the 9 wave gauge locations for the test case $F1$ ($H = 0.2377\ m$, $x_f = 7.8\ m$). Wave breaking crest seen at $x \in [7.78,\ 8.60]\ m$, and $t \in [19.85,\ 20.36]\ s$ as modeled with the initiation and termination criteria.

determine the optimal magnitude of B_{off}, a quantity is calculated as follows,

$$\overline{\eta^2} = \frac{1}{T_p} \int_t^{t+T_p} \eta^2 dt \tag{3.7}$$

where η is the elevation at the gauge at $x = 9.62\ m$, T_p is the peak period (here, always 2.4 s) and t is the instant the breaking wave crest reaches this gauge. This quantity is calculated for 5 different B_{off} values and tabulated in Table 3.2, along with the experimental measurements. For $B_{\text{off}} = 0.1$, a larger amount of energy is dissipated relative to $B_{\text{off}} = 0.5$, leading to a relatively larger decrease in free surface elevation caused by the application of wave breaking, leading to smaller $\overline{\eta^2}$. From Table 3.2, $B_{\text{off}} = 0.4$ is chosen to provide a more accurate prediction compared to the experimental results.

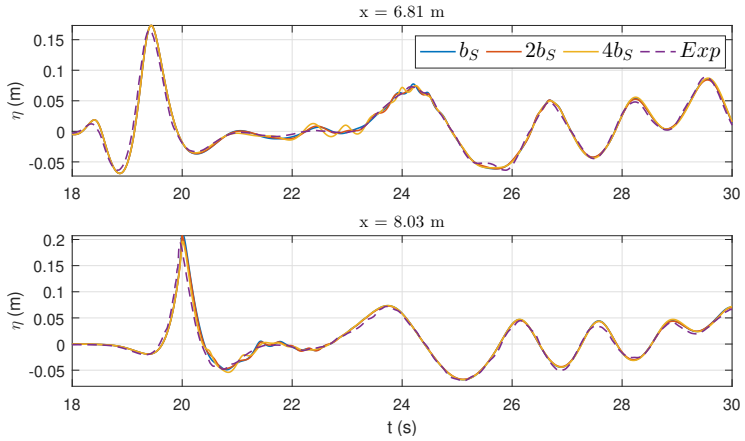

Figure 3.8: Comparison of the free surface elevation for the test case $F1$ at two gauges (at $x = 6.81$ m and $x = 8.03$ m) from the experiments (dashed lines) and the NWT (solid lines) with different breaking strengths, with b_S, the value predicted by Romero et al. 2012.

The empirical breaking strength, as proposed by Romero et al. 2012, was obtained through a curve fitting process using experimental data points. Fig. 3.4 illustrates the distribution of this data, where it can be observed that there is noticeable variability (note that the y-axis is presented in a logarithmic scale). Therefore, the sensitivity of the dissipation strength b is investigated, considering values within the same order of magnitude as the prediction from Romero et al. 2012 (Eq. 3.6). In Fig. 3.8, a comparison of the free surface elevation at the gauge at $x = 6.81\ m$ with the experiments and NWT with different breaking strengths for the test case, $F1$ is seen. For this case, with $b < b_S/2$, the damping pressure is insufficient to prevent the overturning of the free surface. When $b > 2b_S$, the application of the damping pressure becomes abrupt, resulting in oscillations on the free surface.

Fig. 3.9 displays the plot of the instantaneous power dissipation resulting from wave breaking. This variation is proportional to $c(t)^5$, where $c(t)$ is the instantaneous phase speed ($\Pi_b = bc(t)^5/g$). Qualitatively the dissipation is seen to be larger around the onset of wave breaking and gradually decreases until the termination. This pattern of variation is similar to what has been observed in the study by Iafrati 2011.

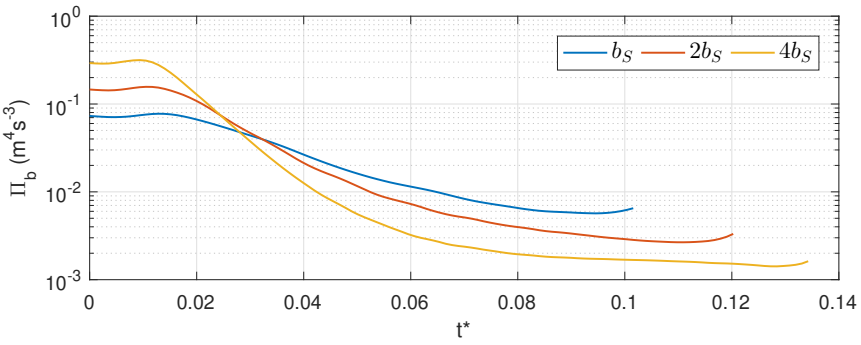

Figure 3.9: The evolution of the instantaneous breaking strength with $t^* = (t - t_b)/T_p$, where t_b is the time instant of the breaking onset in the NWT for three breaking strengths (b_S is the value predicted by Romero et al. 2012).

3.5 Conclusions and perspectives

A parameterized method to model steepness-limited breaking waves based on the universal breaking onset criterion proposed by Barthelemy et al. 2018 and Derakhti et al. 2020 is presented. The breaking strength is determined using the empirical curve provided by Romero et al. 2012, which estimates the breaking strength based on the maximum linear wave steepness (S) of the input waves. From this breaking strength, an instantaneous power to be dissipated is calculated that is proportional to $c(t)^5$. This power is then modeled as a damping pressure acting across the breaking crest (Section 2.3.2.1). The proposed model is validated with the wave flume experiments conducted at Ecole Centrale Marseille, by Lili Kimmoun. These experiments involve the generation of focused breaking waves using a Ricker spectrum of varying maximum wave height and focusing distance.

The NWT is seen to accurately model overturning waves until the overturning jet hits the free surface, a fully reflecting wall, and the desired type of wavemaker motion. The criterion $B = 0.85$ seems like an appropriate criterion for the onset of breaking waves, as it corresponds to the moment when the free surface becomes nearly vertical. In the NWT, regriding is necessary to redistribute nodes equidistant from each other, as the nodes cluster at the crest as they steepen (Grilli & Subramanya 1996). In the breaking test cases shown here, the frequency of regriding was chosen such that the waves overturned by setting $b = 0$ (i.e., zero energy dissipation). This is to ensure that the breaking model is unaffected by regriding.

An alternative approach to determine the breaking strength for deep-water, focused breaking cases could be the use of the empirical curve proposed by Derakhti, Banner & Kirby 2018 with high-fidelity model simulation data. This empirical curve predicts the breaking strength based on the time rate of change of B at the onset, non-dimensionalized with a period calculated at the onset (γ, for the definition, see Eq. 2.17). Unlike the method employed in this study, this approach only requires knowledge of wave kinematics at the onset to predict the breaking strength. This is very useful when determining the input wave conditions are complicated, for example, when

looking at irregular waves. An attempt was made to implement this approach but was unsuccessful as the computation of γ was found to be very sensitive to the discretization. In the calculation of γ from a Navier-Stokes model, as in Derakhti, Banner & Kirby 2018, the discretization in time is orders of magnitude smaller than that used in the NWT. Therefore, it is not practical to employ such a fine level of discretization solely for the purpose of computing γ. There is an attempt being made currently to have accurate calculations of γ at a typical resolution of potential flow models in Ducrozet et al. 2023.

There are areas for improvement in order to develop a more comprehensive model for steepness-limited breaking waves. The current termination criterion is calibrated based on specific cases, and further investigation using a wide range of scenarios is required to establish general conclusions. Additionally, the time variation of the instantaneous power dissipation should be compared with experimental data or validated using Navier-Stokes models to assess the general validity and applicability of the proposed variation. These questions need to be addressed to have a unified steepness-limited dissipation model.

Chapter 4

3D extension of the 2D unified depth-limited breaking model

by S. Mohanlal, J. Harris, M. Yates, and S. Grilli
(Article in preparation)

Nous introduisons une nouvelle méthode pour simuler la dissipation d'énergie résultant du déferlement des vagues à profondeur limitée dans un modèle tridimensionnel (3D) d'écoulement potentiel non linéaire. La méthode combine un critère universel de début de déferlement avec la simulation de la dissipation d'énergie induite par le déferlement, en utilisant un paramètre d'intensité du déferlement non-dimensionnel. Le modèle 3D-FNPF utilisé dans cette recherche résout l'équation de Laplace à l'aide d'une équation intégrale aux limites basée sur la deuxième identité de Green. La détection du déferlement imminent d'une vague est réalise avec un critère universel de début de déferlement basé sur la ratio de la vitesse horizontale des particules à la crête à la vitesse de la phase de la crête. La parametrisation de la dissipation des ondes par déferlement s'effectue en trois étapes. Tout d'abord, d'intensité du déferlement par dissipation non-dimensionnelle est calculée sur la base d'un précédent modèle unifié 2D de dissipation à profondeur limitée. Deuxièmement, la puissance instantanée à dissiper est calculée fonction de l'intensité de déferlement et la vitesse de phase et prend la forme d'une pression d'amortissement sur la crête de la vague déferlante. Le processus de dissipation est arrêté par un critère calibré par une comparaison des simulations de la position de la surface libre avec des données expérimentales de la littérature. Le modèle proposé est appliqué à des vagues régulières avec du déferlement glissant et plongeant sur une barre submergée 3D et une bosse elliptique focalisante. Des travaux futurs étendront ce modèle aux vagues déferlantes 3D irrégulières.

Abstract

Extending an earlier two-dimensional (2D) implementation, a novel method is introduced for both detecting the onset of wave breaking and simulating the resulting energy dissipation in limited water depth, in a three-dimensional (3D) fully nonlinear potential flow (FNPF) model. Breaking onset is identified using a universal criterion, based on the ratio of the horizontal particle velocity at the crest to the crest phase velocity. The breaking-induced energy dissipation is based on the non-dimensional breaking strength parameter and is implemented in the model as an absorbing surface pressure. The 3D-FNPF solves Laplace's equation using a higher-order boundary element method based on Green's second identity and marches the solution forward in time. The implementation of wave dissipation due to breaking is carried out in three steps: (i) a non-dimensional breaking strength parameter is calculated based on a previous 2D unified depth-limited dissipation model; (ii) the instantaneous power to be dissipated is computed using this parameter and energy dissipation is modeled as a damping pressure specified in a region around the breaking crest; and (iii) the dissipation process of each breaking wave is terminated using a criterion calibrated through a comparison of the free surface elevation with experimental data from the literature. The new 3D model is experimentally validated for regular spilling and plunging breaking waves propagating over a 3D submerged bar and an elliptical shoal. Future work will extend this model to irregular 3D breaking waves.

4.1 Introduction

With the recent surge of activity in the offshore energy sector and in the design and construction of large fixed or floating ocean structures exposed to storm waves in intermediate or even shallow water, there is an increasing need for a better understanding of sea state evolution at large spatial and temporal scales and wave-structure interactions at small scales. It is crucial to accurately estimate the kinematics and dynamics of sea states to respond to the specific requirements of a range of applications in this domain, in particular, for the design of structures exposed to breaking waves. Filipot et al. 2018, for instance, presented measurements of the characteristics of breaking waves impacting a lighthouse in extreme sea states, to help optimize design conditions for marine renewable energy converters.

Due to the computational complexity of performing Large Eddy Simulation (LES) (Deardorff 1970, Lubin et al. 2011, 2006) or, Direct Numerical Simulation of the Navier-Stokes (NS) equations (Lubin et al. 2003, Moin & Mahesh 1998), numerical models used to simulate ocean waves typically make simplifying assumptions of the physics, for specific flow properties or regimes, for example by assuming inviscid flow. Additionally, wave models are often classified by on their representation of the free surface boundary conditions and dimensionality, into (i) two-dimensional (2D) horizontal, depth-averaged, such as weakly or fully nonlinear Boussinesq/Serre–Green–Naghdi (Bonneton, Barthélemy, Chazel, Cienfuegos, Lannes, Marche & Tissier 2011, Kirby 2016, Wei et al. 1995); or (ii) 2D vertical or three-dimensional (3D) fully nonlinear potential flow (FNPF) models, such as based on a Higher-Order Spectral (HOS; Ducrozet

et al. 2007, 2017, West et al. 1987) or a Boundary Integral Equation method (BIE; Dold & Peregrine 1985, Fochesato et al. 2007, Grilli et al. 2001, 1989, Guyenne & Grilli 2006, Newman & Lee 2002, Nimmala et al. 2013). For practical applications to nearshore wave propagation, most recent models of the first type (Kazolea & Ricchiuto 2018, Kennedy et al. 2000, Shi et al. 2011) thus use semi-empirical dissipation terms to represent the effects of bottom friction and wave breaking, the latter triggered using a breaking criterion (see, for a large scale practical application Grilli, Westcott, Grilli, Spaulding, Shi & Kirby 2020). Although there were some early attempts to proceed similarly with models of the second type (Grilli et al. 2003, Guignard & Grilli 2001), significant work has recently been focused on extending the range of applications of FNPF/HOS models beyond their physical limits, by including parameterized modeling of wave breaking dissipation (Ducrozet et al. 2017, Mohanlal et al. 2023, Papoutsellis et al. 2019, Seiffert & Ducrozet 2018, Seiffert et al. 2017, Simon et al. 2019, Wang et al. 2022).

In all of these models, the wave breaking parameterization follows a general approach. It begins with defining the onset of wave breaking, followed by estimating the magnitude of energy to be dissipated, and concludes with a termination criterion. Regarding breaking onset, many different criteria have been proposed, often limited to specific depth (e.g., shallow, intermediate, or deep water) regimes (see, for a review Derakhti et al. 2020), for instance, based on a maximum breaking index (Grilli et al. 1997), wave slope (Guignard & Grilli 2001, Simon et al. 2019), or steepness (Miche 1944). More recently, Barthelemy et al. 2018 and Derakhti, Banner & Kirby 2018 have shown that a universal onset criterion for wave breaking in deep or intermediate water can be defined as the ratio of the horizontal particle velocity u to the phase speed c of a crest, reaching $B = u/c = B_{th} = 0.85$, Derakhti et al. 2020 further showed that the same criterion applies to shallow water breaking. This universal criterion was shown to be robust for simulating 2D spilling and plunging breaking waves in 2D-HOS (Seiffert & Ducrozet 2018, Seiffert et al. 2017) and 2D-FNPF (Mohanlal et al. 2023) simulations. Note, Hasan et al. 2019 performed HOS simulations of focused breaking waves in intermediate water and reported that some non-breaking crests were found with $B \in [0.9 - 0.92]$. However, their model was not strictly fully-nonlinear due to the limited HOS expansion (with $M = 5$) that may not represent u at the crest as accurately as in the Eulerian-Lagrangian FNPF or NS models used to develop the B criterion (Barthelemy et al. 2018, Derakhti, Banner & Kirby 2018, Derakhti et al. 2020).

Early parameterizations proposed for the wave breaking energy dissipation rate were based on experimental measurements for spilling wave breakers over mild slopes (Stive 1984, Svendsen et al. 1978), which were idealized as "inverted hydraulic jumps". This dissipation rate was used to successfully simulate spilling breakers in 2D-FNPF models by using a calibrated absorbing surface pressure (Grilli, Horrillo & Guignard 2020, Guignard & Grilli 2001, Papoutsellis et al. 2019, Simon et al. 2019). Kennedy et al. 2000 proposed a parameterization of the energy dissipation based on the eddy viscosity for depth-integrated models, which was then extended to simulate breaking waves in 2D-FNPF models (Papoutsellis et al. 2019, Simon et al. 2019).

Finally, Derakhti, Banner & Kirby 2018 developed a parameterization of the energy dissipation for deep and intermediate water steepness-limited breaking waves by performing simulations with a NS model (Derakhti et al. 2016), and, more recently, they extended this parameterization

to shallow water breaking (Barthelemy et al. 2018, Derakhti et al. 2023, Derakhti, Kirby Jr, Banner, Grilli & Thomson 2018, Derakhti et al. 2022).

The 3D implementation of this parameterization presents some practical difficulties and, hence, has received less attention in current research, although there have been some earlier attempts (Mivehchi 2018, Mivehchi et al. 2017). The identification of wave crests and the accurate computation of their phase speed by direct tracking in 2D horizontal wave fields is complicated (e.g., when small waves travel on large ones or due to discretization errors), except when simplifying assumptions are introduced, such as using the linear dispersion relation and applying a Hilbert transform (Hasan et al. 2019, Mivehchi 2018, Papoutsellis et al. 2019, Stansell & MacFarlane 2002). Additionally, except for the universal empirical parameterization proposed by Derakhti, Banner & Kirby 2018 based on high-fidelity NS simulations, there is currently a lack of simple, but physics-based, models to estimate the rate of energy dissipation in 3D breaking waves (e.g., derived from experimental measurements or theoretical formulations) given the kinematics prior to breaking onset. In recent depth-integrated 3D models (Shi et al. 2011), the dissipation in 3D breaking waves was represented by detecting breaking onset when the ratio of free surface elevation to water depth exceeded 0.8, then using a TVD (Total Variation Diminishing) algorithm and switching the Boussinesq equations to the Nonlinear Shallow Water Equations. Earlier work showed that the resulting numerical dissipation is a reasonable approximation of the wave breaking dissipation (Tonelli & Petti 2009, 2010); however, this assumes that broken waves behave like a moving hydraulic jump (or bore) and, hence, is really only applicable to shallow water breaking. A similar dissipation model is used in Judge et al. 2019. Another non-physical but ad-hoc approach is used in OceanWave3D (Pierella et al. 2021) to prevent instabilities caused by impending breaking waves by applying a filter to smooth the free surface. While this method is numerically very simple and efficient, it lacks physical justification.

Another difficulty in using the B criterion, as already pointed out in 2D-FNPF simulations (Mohanlal et al. 2023), is that the applied absorbing pressure has to be terminated after a certain duration that, in principle, should represent the duration of each wave breaking event. Although some ad-hoc criteria (e.g., Papoutsellis et al. 2019, Simon et al. 2019) have been proposed for simple 2D breaking, at present, there is a lack of sufficient knowledge of the duration of wave breaking events, particularly in 3D, to define accurately a termination criterion (e.g., based on wave kinematic properties, similar to the onset criterion). Mohanlal et al. 2023 used the parameter B to both initiate ($B > 0.85$; following Barthelemy et al. 2018, Derakhti et al. 2020) and terminate (B_{off}) the application of wave breaking dissipation using the absorbing pressure, and for their test cases, the optimal termination criterion was $B_{\text{off}} = 0.3$ for a bar and $B_{\text{off}} = 0$ for a beach slope. Another potential criterion, based on the wave breaking duration τ, was proposed by Derakhti, Banner & Kirby 2018. Based on simulations using an LES model (in this case applied to focused wave trains), they estimated $\tau = 0.75T_b$, where T_b is the wave period calculated at breaking onset.

Building on past work, this study focuses on implementing a general parameterized wave-breaking model applicable to depth-limited wave breaking detection and dissipation in an existing 3D-FNPF model (Harris et al. 2022). Following the approach used in 2D (Mohanlal et al.

2023), breaking onset is determined using the universal B-criterion (Derakhti et al. 2020), in which the wave phase speed is now computed by tracking the movement of 3D wave crests in both space and time. Breaking termination is qualitatively calibrated for each test case to best match experimental data at selected measurement points (as done in 2D; Mohanlal et al. 2023). The computation of the dissipation strength and instantaneous power dissipated is based on a 3D extension of the method described in Mohanlal et al. 2023, which is based on the ratio of wave height to water depth of the braking waves. The proposed model is validated using experimental measurements of both spilling and plunging breaking waves propagating over a 3D submerged bar (Kamath et al. 2022) and an elliptical shoal (Vincent & Briggs 1989).

4.2 Numerical wave tank

The model used and extended in this study is referred to as a 3D Numerical Wave Tank (NWT) based on FNPF theory, following the formulation initially proposed by Grilli et al. 2001 and recently reformulated and extended by Harris et al. 2022. The model simulates irrotational and inviscid flows that are described by a scalar potential ϕ, such that the velocity $\boldsymbol{u} = \nabla\phi$ (where bold letters signify a vector of 3 components along the x, y, and z directions). With this formulation, the conservation of mass is expressed by Laplace's equation governing the potential,

$$\nabla^2\phi = 0 \tag{4.1}$$

in the fluid domain Ω with boundary Γ.

In the NWT, Eq. 4.1 is transformed into a BIE expressed on the domain boundary (Γ), which is discretized at a set of collocation points $\boldsymbol{x_i}$ ($i = 1, ..., N_\Gamma$),

$$\alpha(\boldsymbol{x}_i)\phi(\boldsymbol{x}_i) = \int_\Gamma \left\{ \frac{\partial\phi}{\partial n}(\boldsymbol{x})G(\boldsymbol{x}-\boldsymbol{x}_i) - \phi(\boldsymbol{x})\frac{\partial G}{\partial n}(\boldsymbol{x}-\boldsymbol{x}_i) \right\} \mathrm{d}\Gamma, \tag{4.2}$$

with α, the interior solid angle (in steradians) made by the boundary at $\boldsymbol{x}_i$, $\mathbf{n}$ the outwards normal vector to the boundary at point $\mathbf{x}$, and G the 3D free space Green's function, $G(x-x_i) = 1/(4\pi r_i)$, in which the distance $r_i = |\boldsymbol{x} - \boldsymbol{x_i}|$.

The kinematic and dynamic free surface boundary conditions are expressed in a semi-Lagrangian frame of reference, for which the (single-valued) free surface nodes are fixed in the horizontal directions as follows (Harris et al. 2022),

$$\frac{\delta\eta}{\delta t} = \frac{\partial\phi}{\partial z} - \frac{\partial\phi}{\partial x}\frac{\partial\eta}{\partial x} - \frac{\partial\phi}{\partial y}\frac{\partial\eta}{\partial y} \tag{4.3}$$

$$\frac{\delta\phi}{\delta t} = -g\eta - \frac{1}{2}|\nabla\phi|^2 + \frac{\partial\eta}{\partial t}\frac{\partial\phi}{\partial z} - \frac{P_b}{\rho} \tag{4.4}$$

where η is the vertical position of the free surface, P_b is an absorbing surface pressure that is non-zero for breaking waves, and ρ is the water density. A third-order Runge-Kutta explicit scheme

is used to integrate Eq. 4.3 and 4.4 in time as follows (Harris et al. 2022),

$$\begin{aligned} f^{(1)} &= f^{(n)} + \Delta t(\delta_t f^{(n)}) \\ f^{(2)} &= \frac{3}{4} f^{(n)} + \frac{1}{4}(f^{(1)} \Delta t(\delta_t f^{(1)})) \\ f^{(n+1)} &= \frac{1}{3} f^{(n)} + \frac{2}{3}(f^{(2)} \Delta t(\delta_t f^{(2)})) \end{aligned} \tag{4.5}$$

where f denotes η or ϕ, and Δt is the time step. The discretization is space and time is kept constant throughout the simulation. Similar to the 2D-NWT of Grilli & Horrillo 1997, regular stream function waves are generated in the NWT at a wavemaker boundary and dissipated in an absorbing beach at the far end of the domain. Due to instabilities seen at the wavemaker and free surface intersection for the test cases considered here, a ramp in space of absorbing pressure from Harris et al. 2022 is applied for one wavelength of the free surface from the wavemaker boundary with the reference velocity equal to the instantaneous stream function wave vertical velocity.

In its most recent implementation (Harris et al. 2022), the 3D-BIE model incorporates a parallelized solver based on a Fast Multipole Method (FMM). This method solves efficiently the Laplace equation at each time step, with a computational complexity of $O(N_\Gamma^{1.2})$, which is significantly lower than that of the optimized iterative solver used in earlier versions of the NWT, which had a computational complexity of $O(N_\Gamma^2)$ (Grilli et al. 2001, Guyenne & Grilli 2006). The more advantageous computational complexity of the FMM solver is achieved by using faster, polynomial approximations of Green's function, where the number of terms decreases with distance based on a cost/accuracy criterion. Note that a less efficient, scalar, FMM implementation of Grilli et al. 2001 model had been proposed by Fochesato & Dias 2006 (see also, Fochesato et al. 2007, Grilli et al. 2010.

In this work, however, the classic (but parallelized) Laplace equation solver is used to avoid potential truncation errors resulting from using the FMM, which could affect the predicted kinematics near the wave crest and thus the breaking dissipation. This will enable focusing on evaluating the wave breaking parameterization in the model. Once the latter is validated, the complete 3D-FMM-BIE solver could be used in future, larger-scale, applications to increase computational efficiency.

4.3 Wave breaking model

In shallow or intermediate water depth, wave breaking can result from bathymetry-induced shoaling (Grilli, Horrillo & Guignard 2020, Mohanlal et al. 2023, Papoutsellis et al. 2019, Simon et al. 2019) and/or directional/frequency wave focusing (Fochesato et al. 2007), leading to a high energy concentration in wave crests at the time of breaking onset (Boettger et al. 2023). Hence, at least initially, wave breaking dissipation is centered around the crests where it is largest. For spilling breakers, this is true throughout the breaking event.

Therefore, as a first step towards implementing wave breaking onset and dissipation in the 3D-NWT, it is necessary to identify the crests within a given wave field and to track them accurately in time in order to calculate their phase speed c (i.e., as the time derivative of the crest displacement), which is required both for calculating the $B = u/c$ criterion and the dissipated power. For the former, the horizontal particle velocity u at the crest must also be computed instantaneously. Then the energy dissipation caused by wave breaking must be estimated for each wavefront/crest identified to be breaking.

The details of the implementation of the wave breaking model in the 3D-FNPF-NWT are given in the following subsections.

4.3.1 Identification of wave crests

In the 2D-FNPF-NWT of Mohanlal et al. 2023, wave crest locations were found by identifying nodes on the free surface with a vertical elevation higher than that of the nodes in the x-direction, the primary direction of propagation, and then fitting cubic polynomials to elements around these nodes and determining the maximum more precisely. Each wave crest time history is then tracked by assuming that the crests move less than Δx (discretization in space) in consecutive time steps. The wave phase speed was then computed as the time derivative of the crest trajectories.

In the 3D-FNPF-NWT, this method is generalized to find the local maxima of bi-cubic local *surface units* that subdivide the typically curved wavefronts. The surface units represent the wavefronts as piecewise-linear segments over which the wave conditions are assumed to be quasi-2D in the direction orthogonal to each segment (Fig. 4.1 (b)). Surface units are defined over the entire free surface Cartesian grid, with dimensions $3\Delta x$ by $3\Delta y$ in the x and y directions, respectively; these dimensions were found to be small enough to assume that wavefronts are linear within each surface unit. At each time step, the surface units relevant to the breaker model are identified (in short- or long-crested wave fields) as those traversed by a wavefront, meaning that they have at least one peak (maximum) in the primary direction of propagation (here, x).

At time step t, n_t linear wavefront segments, or *crest units*, denoted by $\mathcal{L}^t_{\mathcal{C}}$ ($\mathcal{C} = 1, ..., n_t$), are identified in corresponding 4 by 4 node surface units. Crest units are computed in surface units in a curvilinear coordinate system (ξ, χ), as follows (Fig. 4.1): (i) a local interpolation of the surface elevation, $\eta(\xi, \chi)$, is defined based on bi-cubic shape functions; (ii) the wavefront is defined as the locus of points $(x^t_{\mathcal{C}k}, y^t_{\mathcal{C}k})$ ($k = 1, ..., e$) that satisfy $\partial\eta(\xi, \chi)/\partial\xi = 0$, within the intervals $\chi \in [-1,\ 1]$ (in practice, to assess these properties, 11 uniformly spaced points are taken along χ in any given surface unit; see example in Fig. 4.1b); any quantity desired at points $(x^t_{\mathcal{C}k}, y^t_{\mathcal{C}k})$, such as elevation η or particle velocity $\boldsymbol{u}$, is calculated from the bi-cubic shape functions evaluated at these points and the nodal values of the quantity in the corresponding surface unit; (iii) the various crest units identified at a given time are connected to their nearest neighbor to define complete wavefronts. Fig. 4.2 shows an example of assembled wavefronts within a complete wave field, where surface units are represented by dashed rectangles and their corresponding crest units by discrete line segments of dotted points. Appendix 1 provides details on the identification

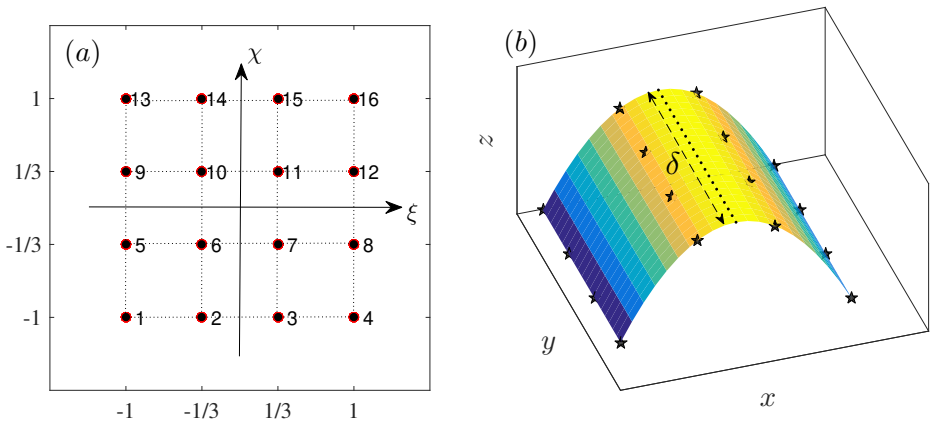

Figure 4.1: (a) Surface unit, with 4 by 4 nodes used to define bi-cubic shape functions in local curvilinear coordinates (ξ, χ). (b) Crest unit (discrete dotted line segment) of length δ identified in global coordinates within a surface unit (nodes denoted by stars), as a set of points $(x^t_{\mathcal{C}k}, y^t_{\mathcal{C}k})$. The color scale represents the free surface elevation.

of surface units and crest units.

4.3.2 Wave particle velocity and celerity along wavefronts

The horizontal particle velocity and phase speed used to estimate the $B = u/c$ criterion are calculated for each crest unit at the mean location (defined by e points) as,

$$u = \sqrt{\left(\frac{\partial\phi}{\partial x}(\overline{x_{\mathcal{C}}}^t, \overline{y_{\mathcal{C}}}^t)\right)^2 + \left(\frac{\partial\phi}{\partial y}(\overline{x_{\mathcal{C}}}^t, \overline{y_{\mathcal{C}}}^t)\right)^2} \tag{4.6}$$

and,

$$c = \sqrt{\left(\frac{d\overline{x_{\mathcal{C}}}^t}{dt}\right)^2 + \left(\frac{d\overline{y_{\mathcal{C}}}^t}{dt}\right)^2} \tag{4.7}$$

respectively, with,

$$\overline{x_{\mathcal{C}}}^t = \frac{1}{e}\sum_{k=1}^{e} x^t_{\mathcal{C}k} \quad \text{and} \quad \overline{y_{\mathcal{C}}}^t = \frac{1}{e}\sum_{k=1}^{e} y^t_{\mathcal{C}k} \tag{4.8}$$

To calculate the time derivatives in Eq. 4.8, the movement of crest units must be tracked in time. First, for each crest unit, a line perpendicular to it is constructed, written as $y = mx + \beta$, with the slope m, and the y-intercept, β, and passing through its mean location $(\overline{x_{\mathcal{C}}}^t, \overline{y_{\mathcal{C}}}^t)$. To determine where a crest unit $\mathcal{L}^{t-1}_l$ from time step $t-1$ moved to at the time step t, firstly, all crest units at time step t ($\mathcal{L}^t_{\mathcal{C}}$) that satisfy $|\overline{y_l}^{t-1} - \overline{y_{\mathcal{C}}}^t|/\Delta x < n$, where $n = 2.8$ (a value slightly less than the approximate span length of a crest unit, 3) are found. Lastly, the closest neighboring crest unit from this list is determined such that the distance between their mean locations ($\sqrt{(\overline{x_{\mathcal{C}}}^t - \overline{x_l}^{t-1})^2 + (\overline{y_{\mathcal{C}}}^t - \overline{y_l}^{t-1})^2}$) is minimum. Prior to calculating the phase speed using the time derivatives (i.e., Eq. 4.7), to treat sawtooth oscillations, an exponential smoothing

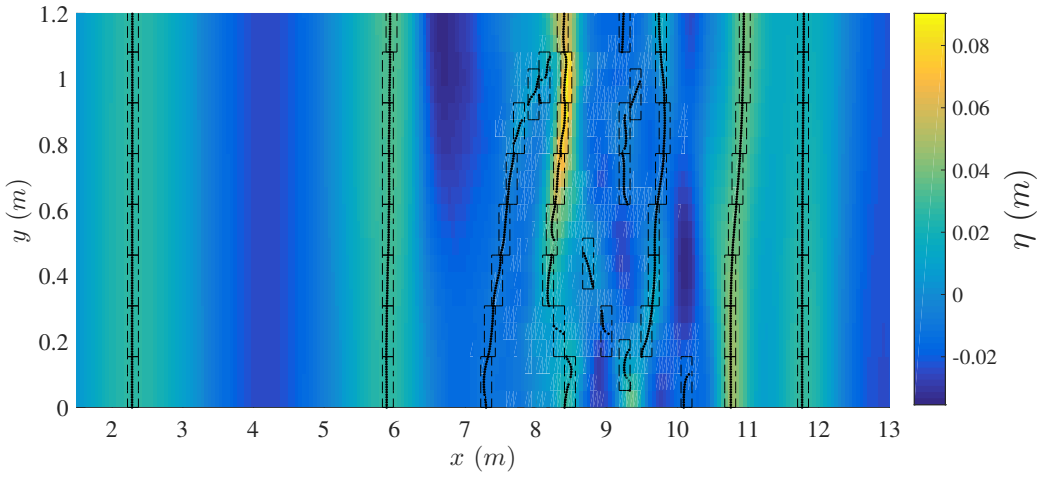

Figure 4.2: Free surface elevation (in color) showing wavefronts/crests (in yellow tones) of regular waves propagating over a submerged bar (note, the scales in x and y are different). Surface units are denoted by dashed rectangles were identified using Algorithm 1 and their corresponding crest unit as a set of points (x^t_{Ck}, y^t_{Ck}) marking the discrete linear wavefront are denoted by dots.

is applied on both $\overline{x_C}^t(t)$ and $\overline{y_C}^t(t)$, as detailed in Mohanlal et al. 2023.

Wave crests reaching breaking onset are identified with the universal criterion $B = 0.85$ (Derakhti et al. 2020).

4.3.3 Rate of energy dissipation and energy absorption in the model

The standard parameterization of the power dissipated per unit of crest length (W/m), or rate of energy dissipation in breaking waves (J/(m.s)) is,

$$\Pi_b(t) = b\frac{\rho c^5}{g} \tag{4.9}$$

where b is a non-dimensional breaking strength parameter. Thus, for each crest unit identified to be breaking at time t in the 3D-NWT, Eq. 4.9 is used to specify the instantaneous power to be dissipated.

To estimate the parameter b, Derakhti, Banner & Kirby 2018 ran a series of NS simulations of breaking waves in deep and intermediate water depth, proposing that on average over the breaking event, $\overline{b} = 0.034\,(\gamma - 0.30)^{2.5}$, where $\gamma = T_b\frac{dB}{dt}$ when $B = 0.85$, and the breaking wave period, $T_b = L_b/c_{lb}$, with c_{lb} the linear wave celerity at breaking and L_b a relevant breaking wavelength. In this formulation, $\frac{dB}{dt}$ represents the rate at which the breaking onset threshold is reached, which they found was higher for plunging breakers than for spilling breakers, as expected. For shallow water waves, however, Derakhti et al. 2023, Derakhti, Kirby Jr, Banner, Grilli & Thomson 2018, Derakhti et al. 2022 found that, for $\gamma > 1.3$, $\overline{b}$ reached a nearly constant value ($\overline{b} \simeq 0.034$).

Mohanlal et al. 2023 used a 2D-NWT to simulate 2D shallow water, depth-limited breaking waves (dissipating energy with a hydraulic jump analogy) and compared their results with experiments for a range of regular and irregular wave cases, reached a conclusion consistent with these findings. They found that waves with a wave height nearly equal to the local water depth at the onset of breaking, $H/d \approx 1$, would dissipate with $b \approx 0.1$. This dissipation resulted in the decay of the wave height across the surfzone, until the termination of breaking occurred for $H/d \approx 0.4$ with $b \approx 0.01$. Supplementing their simulations with earlier findings in Battjes 1974, Dean & Dalrymple 1991, Mei 1989 that depth-limited breaking waves at the onset have $H/d \in [0.7,\ 1.2]$, Mohanlal et al. 2023 concluded that on average for depth-limited breaking waves, $\overline{b}$ should be on the same order of magnitude. With this rationale, the value $\overline{b} = 0.05$ was selected, and simulations of several depth-limited wave breaking test cases were compared with experiments from breaking onset up to termination, showing that this provided satisfactory results. With a constant b value, the estimation of the power dissipated in breaking waves is simplified and becomes independent of the wave parameters, which are challenging to estimate for irregular waves, particularly in 3D (except for the instantaneous wave celerity $c(t)$) which can be obtained in the 3D model as detailed above (Eq. 4.7). Therefore, in the applications of the 3D model presented hereafter, which all fall within the same shallow water breaking regime, a constant value of $\overline{b} = 0.05$ is used.

In the 3D-FNPF model, the instantaneous power to be dissipated, once estimated, is used to calibrate the absorbing surface pressure (as in Grilli, Horrillo & Guignard 2020, Guignard & Grilli 2001), extended here to a 2D surface around the breaking crest, as follows,

$$P_b(x,y,t) = \nu(t)\,\frac{\partial \phi}{\partial n}(x,y,t) \qquad \forall (x,y) \in \Gamma_b \tag{4.10}$$

where $\nu(t)$ is an absorbing function defined such that the rate of work produced by the pressure against the wave motion, $P_b\,\partial_n\phi$, integrated over the breaking wave surface, is equal to the instantaneous rate of energy dissipation (dissipated power) across the span δ of the crest unit, $\Pi_b\,\delta$.

$$\nu(t) = \frac{\Pi_b(t)\,\delta}{\int\int_{\Gamma_b} (\partial_n\phi)^2 \sqrt{1+(\partial_x\eta)^2+(\partial_y\eta)^2}\,dx\,dy}. \tag{4.11}$$

The breaking region Γ_b of a crest unit is determined as follows: (i) the end points of the crest unit of a breaking crest are identified (points $(x^t_{\mathcal{C}1}, y^t_{\mathcal{C}1})$ and $(x^t_{\mathcal{C}e}, y^t_{\mathcal{C}e})$, e.g., Fig. 4.3), and from these points, the normal directions on either end of the wavefront are computed ($\boldsymbol{n}_1$ and $\boldsymbol{n}_2$; with $\boldsymbol{n}_1 = -\boldsymbol{n}_2$, e.g., Fig. 4.3); (ii) moving along the x-direction from $(x^t_{\mathcal{C}1}, y^t_{\mathcal{C}1})$ by an interval of Δx and from $(x^t_{\mathcal{C}e}, y^t_{\mathcal{C}e})$ by an interval of $-\Delta x$, nodes with y value closest to normals are identified, this is repeated until nodes that satisfy $|\partial_n\phi| < \varepsilon\,|\partial_n\phi|_{max}$, where $\varepsilon \ll 1$ (here $\varepsilon = 10^{-2}$) are obtained, denoted by points a and b (e.g., Fig. 4.3); and (iii) the nodes inside the rectangle formed by the two opposite vertices a and b cover the breaking region, Γ_b of the respective crest unit, over which the absorbing pressure defined in Eqs. 4.10 and 4.11 is applied. For instance, for a sinusoidal crest, as $\epsilon \to 0$, the breaking region becomes the entire region between the preceding and the following trough. For the discretization chosen here, the extent of the breaking region is

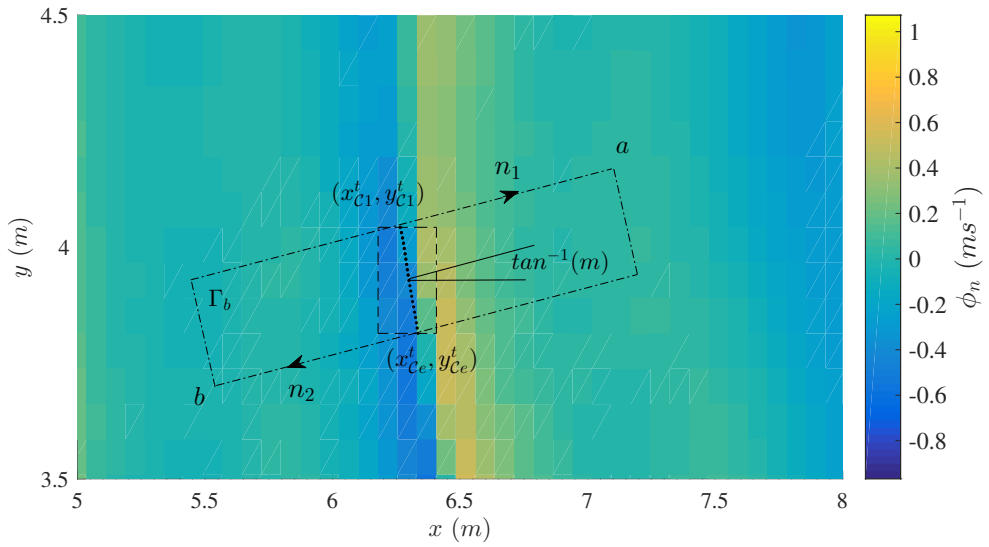

Figure 4.3: Calculation of the breaking area Γ_b in the 3D model, for a surface unit (rectangle with dashed lines) identified as breaking, with a crest unit marked by dotted points. The region Γ_b of the free surface identified for applying the damping pressure P_b (Eqs. 4.10 and 4.11) is defined as the region enclosed by the dashed-line rectangle. The color scale corresponds to the normal particle velocity at the free surface.

not very sensitive to ϵ. Fig. 4.4 shows an example of the breaking regions identified in a simulated wave field corresponding to the regular breaking test case of Vincent & Briggs 1989 for periodic waves propagating over a semi-elliptical shoal. This dissipation model was found to be unstable for linearly-interpolated BEM elements, hence cubic B-spline elements are used to discretize the boundary (Harris et al. 2022).

4.3.4 Termination of breaking event

For each identified wave breaking event, the energy dissipation is interrupted in the model using a breaking termination criterion. Unlike the onset criterion, however, there is not yet a known universal termination criterion. Following Mohanlal et al. 2023 for 2D breakers, the parameter B is used here to specify a termination threshold B_{off}, which is calibrated for each test case presented in this study. Additionally, for comparison, the breaking duration proposed by Derakhti, Banner & Kirby 2018 is also reported for these specific cases.

4.4 Results

In the following, the 3D-FNPF-NWT using the new breaking onset and dissipation model is validated with measurements from two sets of laboratory experiments performed for regular long-crested waves propagating over a 3D submerged bar or a semi-elliptical shoal. In all cases, the simulated time series of the free surface elevation are compared with the experimental measure-

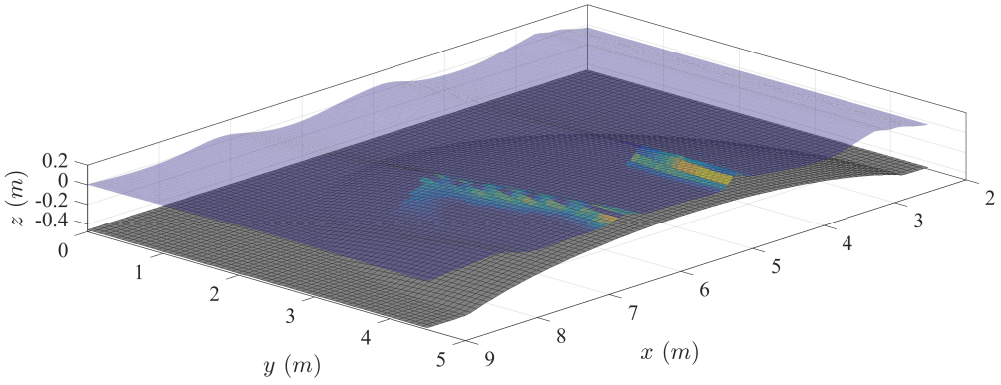

Figure 4.4: Example of the breaking regions identified at arbitrary time t for the simulated wave field corresponding to the regular breaking test case of Vincent & Briggs 1989 for periodic waves propagating over a semi-elliptical shoal (shown at the bottom in the figure), with the wavemaker located at $x = 0$. The color scale indicates the magnitude of the instantaneous energy dissipated per unit area, $P_b\phi_n$, in the breaking regions.

ments acquired using wave gauges.

4.4.1 Regular wave propagation over a 3D submerged bar

Kamath et al. 2022, Roy 2018 studied the lateral energy transfer across the wavefront occurring in periodic waves propagating over a submerged bar with a side slope. They performed 18 experiments in a 18.3 m long, 1.237 m wide, and 1.2 m tall tank equipped with a flap wavemaker at one extremity, for non-breaking and breaking periodic waves propagating over a 3D submerged bar with $1 : 6.933$ front and back slopes, and a $1 : 0.963$ lateral slope on one side (Fig. 4.5), for 3 water depths (0.52, 0.55, and 0.58 m) and a range of wave heights (0.019-0.1 m) and periods (1.21-3.93 s). In each experiment, free surface elevation time series were measured at 20 locations as shown in Fig. 4.5.

In this application, three experiments were simulated, all with a depth at the wavemaker $h = 0.58$ m (C series), for: ($C1$) non-breaking waves of height $H = 0.031$ m and period $T = 2.869$ s; ($C4$) spilling breaking waves with $H = 0.052$ m and $T = 1.817$ s; and ($C6$) plunging breaking waves with $H = 0.095$ m and $T = 1.282$ s (see Table 4.1). For these test cases, the 3D-NWT had dimensions: $0 \leq x \leq 20$ m (with the toe of the bar located at $x = 3.459$ m) and $0 \leq y \leq 1.237$ m, and was discretized with $\Delta x = \Delta y = 0.0515$ m, which yielded, $L/\Delta x \approx 120$, 75, and 50 (where L is the wavelength at the wavemaker) for the non-breaking, spilling breaking, and plunging breaking cases, respectively. Additionally, the vertical and temporal resolution were $\Delta z = 0.096$ m and $\Delta t = 0.01$ s, respectively. An absorbing beach was specified at the far end of the NWT, at $12.5\,\mathrm{m} \leq x \leq 20\,\mathrm{m}$ ($\approx 1.5L$, $2L$ and $3L$ for test cases $C1$, $C4$, and $C6$, respectively).

Non-breaking case $C1$: Fig. 4.7 compares simulated and measured time series of free surface elevation for case $C1$ at three selected wave gauge locations (#1, #17, and #20), for 5 wave periods

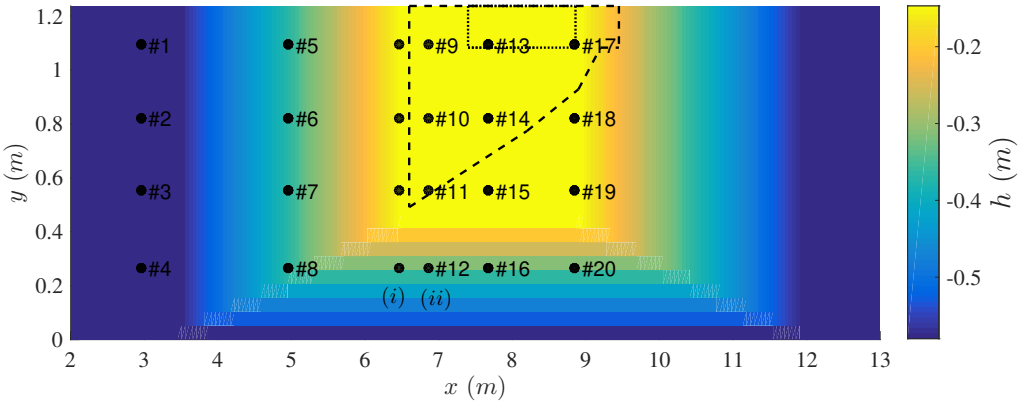

Figure 4.5: Bathymetry and location of the 20 wave gauges in the simulations and experiments of Kamath et al. 2022 (note: for gauges #9-#12, the array was moved to measure the waves before they became unstable during breaking events, such that column (i) was used for test cases $C1$ and $C6$, and column (ii) for $C4$). The flap wavemaker is located at $x = 0$. Polygons enclose the approximate region where breaking crests were identified in the NWT simulations, from breaking onset up to termination, for $C4$ (dotted) $C6$ (dashed)

Test case	H (m)	T (s)	S	$\Delta x = \Delta y$ (m)	Absorbing beach $L/\Delta x$
$C1$ (Non-breaking)	0.031	2.869	0.011	0.0515	120
$C4$ (spilling)	0.052	1.817	0.029	0.0515	75
$C6$ (plunging)	0.095	1.282	0.074	0.0515	50

Table 4.1: Test cases of Kamath et al. 2022 simulated using the 3D-FNPF-NWT: Wave parameters and NWT spatial discretization and absorbing beach length. In all cases, the still water depth was $h = 0.58$ m.

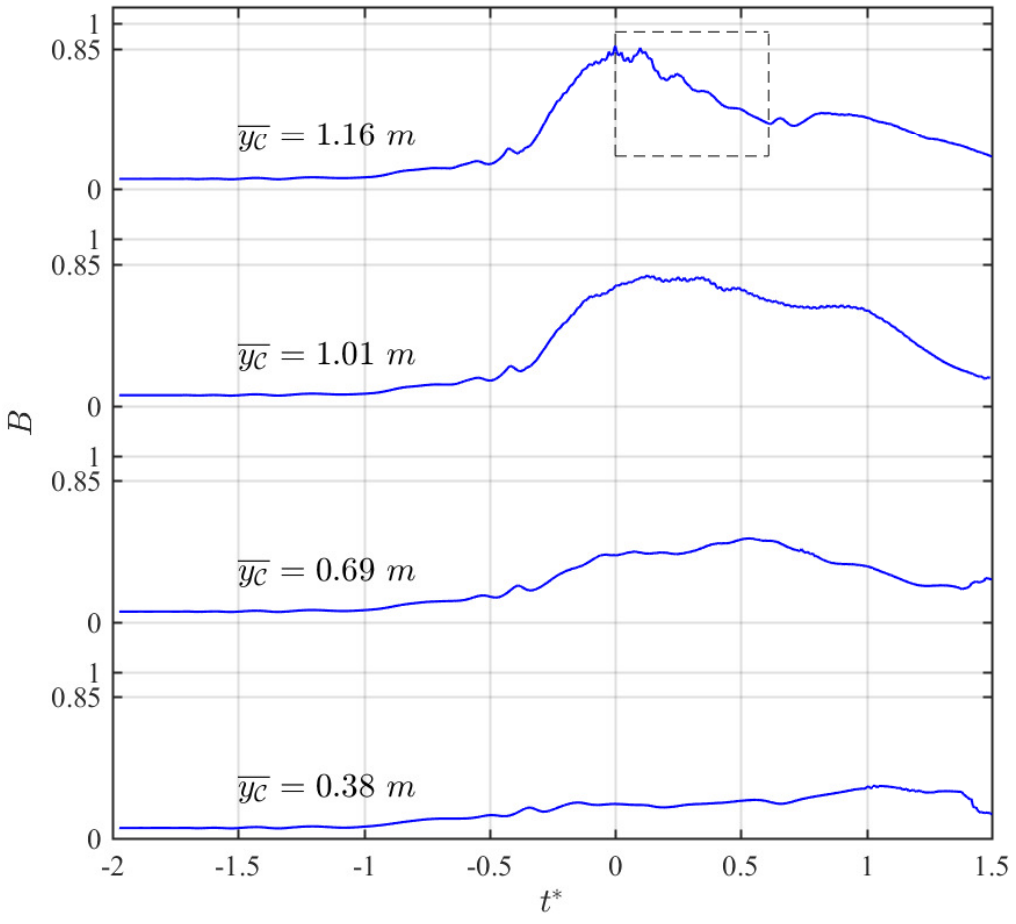

Figure 4.6: Evolution of the breaking onset criterion B, as a function of $t^* = (t - t_O)/T_b$, where t_O is the instant of breaking of the crest unit located at $\overline{yc} = 1.16$ m for the spilling breaking test case $C4$. The dashed rectangle encloses the breaking crest units.

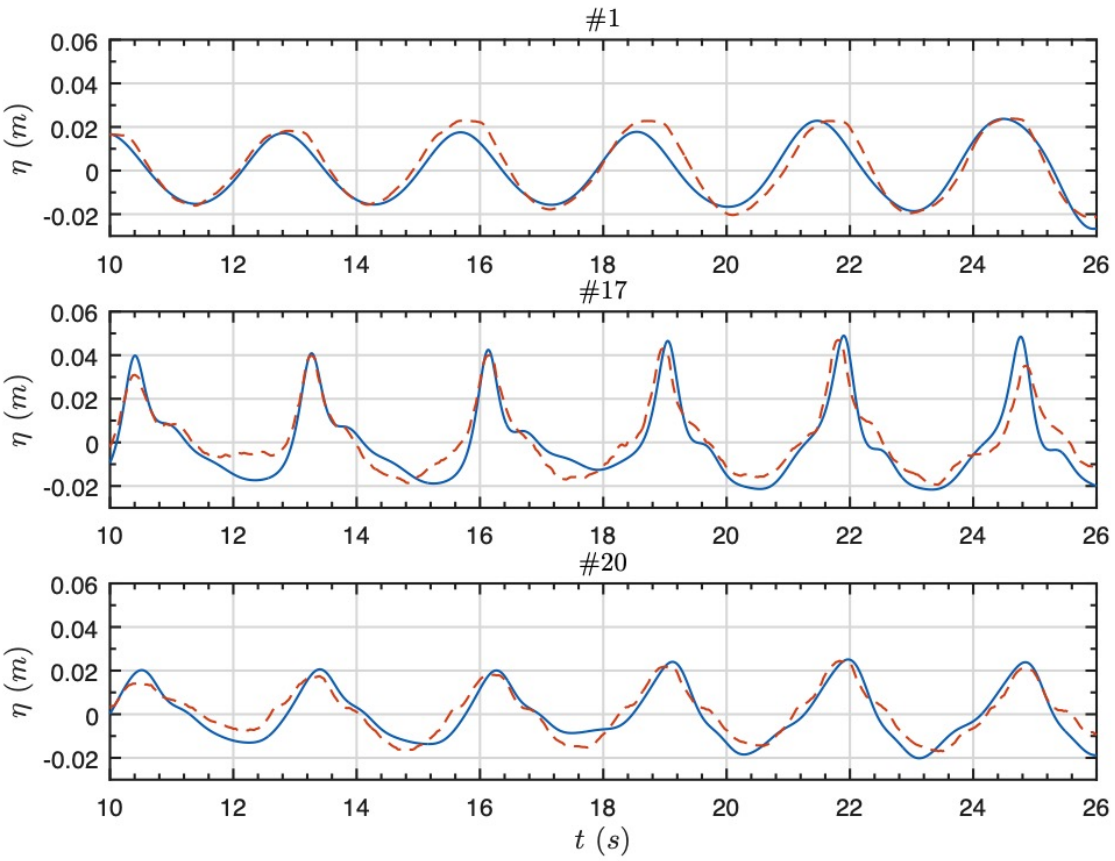

Figure 4.7: Propagation of periodic waves over a 3D bar for the non-breaking test case, $C1$ (Kamath et al. 2022). Time series of the free surface at selected gauge locations in (dashed red line) experiments; and (solid blue line) NWT simulations.

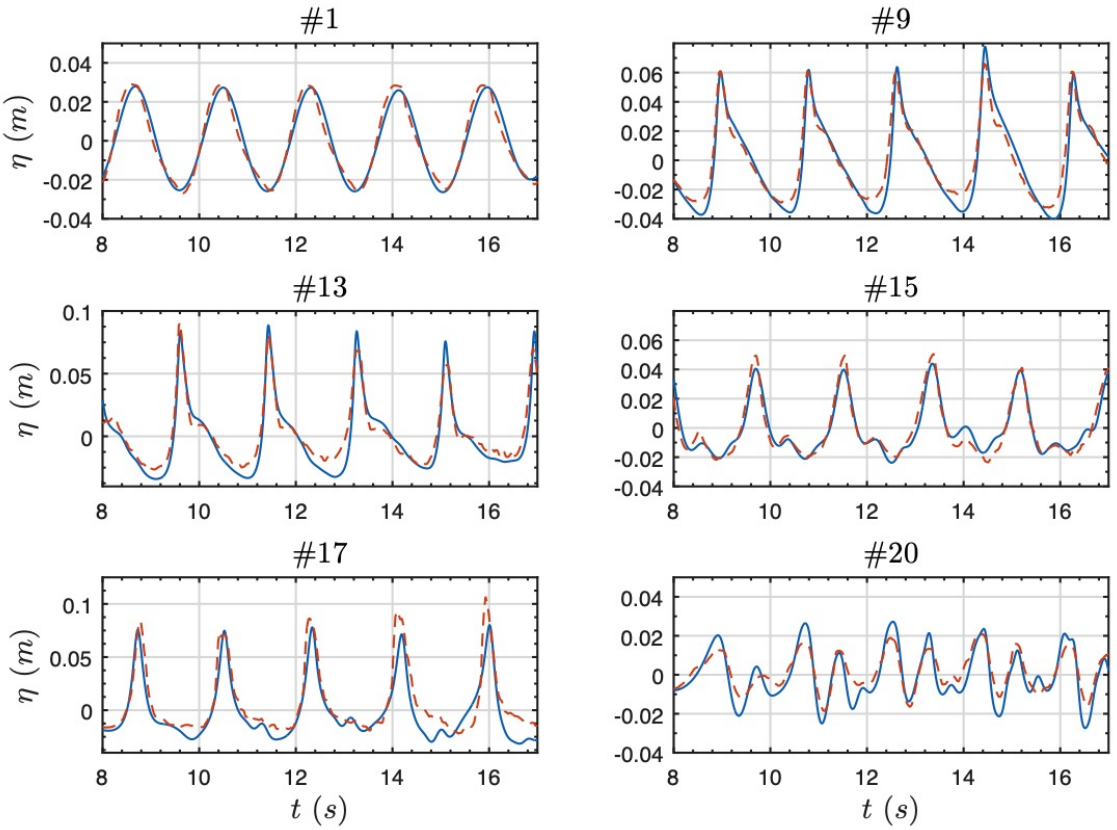

Figure 4.8: Propagation of periodic waves over a 3D bar for the spilling-breaking test case, $C4$ (Kamath et al. 2022). Time series of the free surface at 3 selected gauges for the experiments (dashed line) and the 3D-NWT simulations (solid line).

after reaching quasi-steady state in the NWT. Regular periodic incident waves (#1) propagate in constant depth up to $x = 3.459$ m, then shoal along the bar front slope (for $y > 0.417$ m), growing steeper and increasingly more asymmetric. In the shallowest region over the bar (#17), the wave height reaches a maximum that is about twice the incident wave height. The same regular waves also propagate along the lateral slope (for $y < 0.417$ m) but they are less steep (#20) than the waves over the bar crest since the water is deeper. A maximum value of the breaking onset criterion $B \approx 0.22$ was computed in these simulations, which is significantly below the threshold and hence the breaking dissipation was never activated, in agreement with the experiments where breaking was not observed.

Overall, in the results of Fig. 4.7, considering the small amplitude of waves and experimental errors, good agreement is observed between the simulated and experimental results. Note that in Fig. 5 of Kamath et al. 2022, they also compared their simulations using REEF3D with the experimental results for this case and, their results show similar agreement with the experiments as the results obtained here with the 3D-NWT.

Spilling breaker case $C4$: In Case $C4$, the incident wave steepness (H/L) increases to 0.029, and spilling breaking was observed at the crest of the bar in the experiments. From Fig. 4.6, the

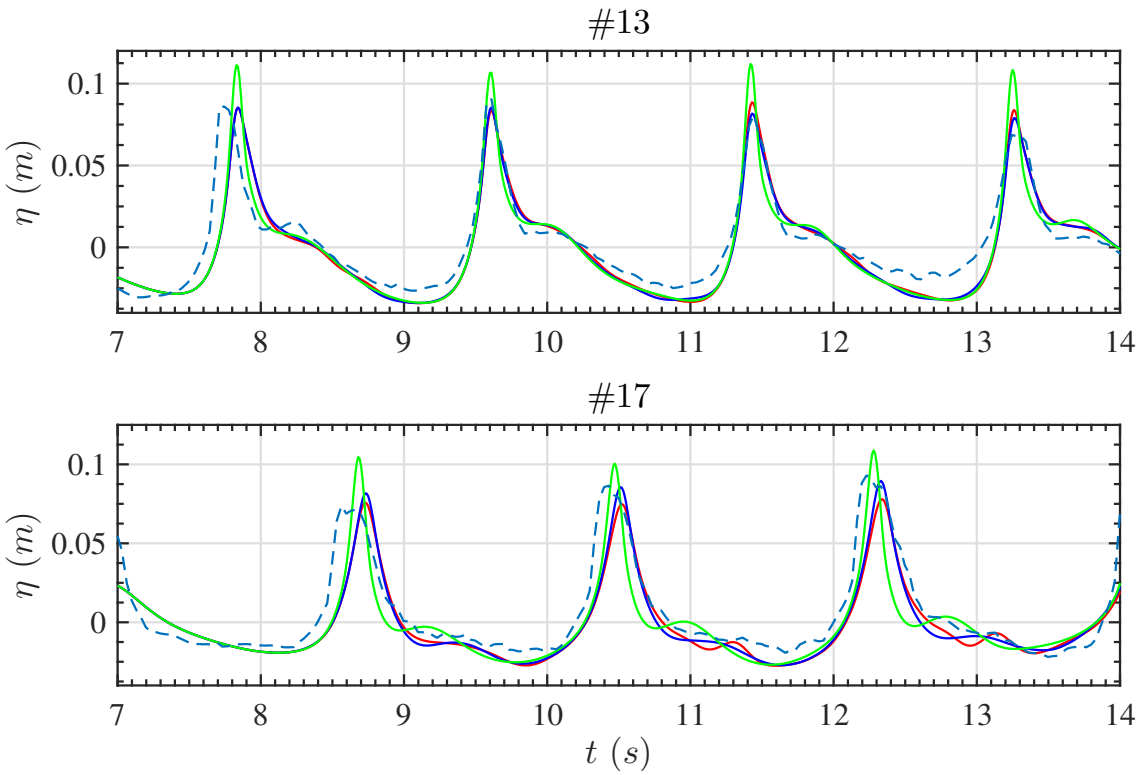

Figure 4.9: Propagation of periodic waves over a 3D bar for the spilling-breaking test case, $C4$ (Kamath et al. 2022). Time series of the free surface at 3 selected gauges for the experiments (dashed line) and NWT simulations with the breaking model deactivated (i.e., $b = 0$; solid green), and activated (i.e, $b = 0.05$) with $B_{\text{off}} = 0.3$ (solid blue) and $B_{\text{off}} = 0.4$ (solid red).

temporal evolution of B in the NWT domain shows that it remains constant in the uniform depth region and starts increasing as the waves shoal up the bar. Breaking onset occurs at $x = 7.3$ m, after the third array of wave gauges, as observed in the experiments, and $y > 1.08$ m, over the shallowest part of the submerged bar. Once wave breaking is initiated, the absorbing pressure P_b is applied in the NWT, and B gradually decreases until the breaking termination criterion $B_{\text{off}} = 0.3$ is met. For the non-breaking crests (i.e., $y < 1.08$ m; see Fig. 4.6), B reaches a maximum $B \approx [0.3,\ 0.8]$), then remains roughly constant and lower than B_{th} over the top of the bar ($6.46 \leq x \leq 8.9$ m), before decreasing again over the back slope of the bar ($x > 8.9$ m).

After reaching a quasi-steady state in the NWT, a comparison of the simulated and measured time series of the free surface elevation for 5 wave periods shows overall good agreement (Fig. 4.8, at 6 selected wave gauge locations (#1, #9, #13, #15, #17, and #20). In the simulations, wave breaking onset occurs at gauge #9, at $x = 7.4$ m and $y > 1.08$ m and continues up to just before gauge #17 ($x \approx 8.86$ m) (see Fig. 4.5). As in case $C1$, incident regular waves (#1) shoal up over the bar, resulting in steeper and more asymmetric waves over the top of the bar (#9, #13, #17), with less steep waves close to the lateral slope (#15). Nonlinear waves that propagate laterally from the top of the bar to the side slope release their bound higher-order harmonics, causing additional shorter-period oscillations (#20), which are mostly reproduced in the simulations, even if small differences are noticeable in the wave amplitudes. Overall, good agreement is observed between the simulated and measured free surface elevations, in particular in the area with breaking waves (e.g., gauges #13, #17), with a slight difference in the wave amplitudes for gauges that are farther downstream (e.g., #20). This may be a sign that wave reflection in the physical tank was larger than in the NWT, where long absorbing beaches ($2L$ for case $C4$) were used in the simulations without attempting to calibrate their length using the observations. Note that, although they did not show the results for the case $C4$, Kamath et al. 2022 compared their simulations using REEF3D with the experimental results for a different spilling-breaking case ($C3$ in Fig. 7 of their paper) and, when accounting for the scale of their figure, a similar agreement is achieved with the 3D-NWT.

To test the sensitivity of the simulation results to the breaking termination criteria B_{off}, along with $B_{\text{off}} = 0.3$, an additional simulation was run with $B_{\text{off}} = 0.4$ (Fig. 4.9). Comparing the time series of the free surface elevation at gauges #13 and #17 with the experimental data, a similar agreement was obtained using either B_{off} value. For this test case, in the NWT, choosing $B_{\text{off}} = 0.3$ yields a breaking duration, $t_b = 0.85$ s. For comparison, the breaking duration parameter proposed by Derakhti, Banner & Kirby 2018, τ, with T_b (see for definition Derakhti, Banner & Kirby 2018) was calculated at breaking onset at $y = 1.237$ m. For test case $C4$, this yields $\tau = 1.26$ s, which is longer than the duration estimated in the 3D-NWT. Fig. 4.9 also shows results for the same case and gauges, when the wave breaking model is deactivated ($b = 0$) i.e., having an absorbing pressure $P_b = 0$. In this case, the wave crest elevations are over-predicted by about 30% compared to the experiments.

Plunging breaker case $C6$: In test case $C6$, the incident wave steepness increased to 0.074, and plunging breaking was observed in the experiments. After a quasi-steady state is reached in the NWT, a comparison of approximately 4 wave periods of the simulated and measured time series

of the free surface elevation at 6 selected wave gauge locations shows only small differences (Fig. 4.10). Breaking onset occurs just after the gauges #9, #10, and #11 ($x \approx 6.6$ m and $y > 0.49$ m; see Fig. 4.5), in agreement with the observations of the experiment that breaking occurred after the third array of wave gauges, and continues until slightly beyond gauge #17 ($x \approx 9.3$ m) (see, Fig. 4.5). As in case $C4$, $B_{\text{off}} = 0.3$ is taken here which yields a duration of wave breaking of $t_b = 2.23$ s. From the free surface elevation at the onset at $y = 1.237$ m, the breaking wave period $T_b = 1.03$ s, or $\tau = 0.77$ s. Thus, for this plunging breaking test case, the wave breaking duration proposed by Derakhti, Banner & Kirby 2018 estimates a shorter breaking duration than using the B_{off} threshold. As in the previous test cases, regular incident waves shoal and break on top of the bar, but since the incident waves are steeper, wave breaking occurs more violently in experiments, as plunging breakers. The comparison of the NWT results with the experiments is good for the first couple of wave periods and then larger differences appear, especially at the gauges closer to the walls, as seen in the previous test case. Overall, the agreement stays quite reasonable. Note again that, although they did not show the results of case $C6$, Kamath et al. 2022 compared their simulations using REEF3D with the experimental results for a similar plunging-breaking case ($C5$ in Fig. 9 of their paper) and, when accounting for the scale of their figure, similar agreement is achieved with the 3D-NWT. Both models show larger differences with the experimental measurements at downstream gauges, in particular closer to walls. As with the previous test case, this might be due to the presence of wave reflections in the physical wave tank, and the difference in the input wave generation method employed in the physical wave tank compared to the numerically precise stream function wave generation utilized in simulations.

To evaluate how well the experimental wave shape and nonlinear features are reproduced in the simulations, the significant wave height H_s and skewness Sk are computed from the free surface elevation time series as follows,

$$H_s = 4\sigma \tag{4.12}$$

$$Sk = \langle (\eta - \langle \eta \rangle)^3 \rangle / \sigma^3 \tag{4.13}$$

where $\sigma^2 = \langle (\eta - \langle \eta \rangle)^2 \rangle$ is the free surface variance and $\langle\ \rangle$ denotes the time averaging operator, applied over a selected time interval. The spatial distribution of H_s and Sk is computed for a duration of 5 wave periods for this test case (Fig. 4.11). Over the top of the bar and prior to breaking, the waves are expected to be highly asymmetric, with near vertical front faces. A decrease in H_s and Sk is observed in the breaking region from the onset ($x = 6.6$ m and $y > 0.49$ m) up to termination ($x = 9.3$ m) due to the energy absorption that attenuates the waves.

Fig. 4.12a and b show the evolution of H_s and Sk for the spilling ($C4$) and plunging ($C6$) breaking cases, respectively, along line $y = 0.822$ m, which passes through gauges $\#2$, $\#6$, $\#10$, $\#14$ and $\#18$. H_s and Sk increase up to breaking onset, as waves shoal on the front slope of the bar and decrease during breaking over the bar. Overall, satisfactory agreement is observed between the simulated and measured wave statistics at the five wave gauges. Additional experimental measurements are needed to analyze further the differences in the simulations and experiments, in particular to validate the presence of oscillations in wave height and skewness after $x = 10$ m

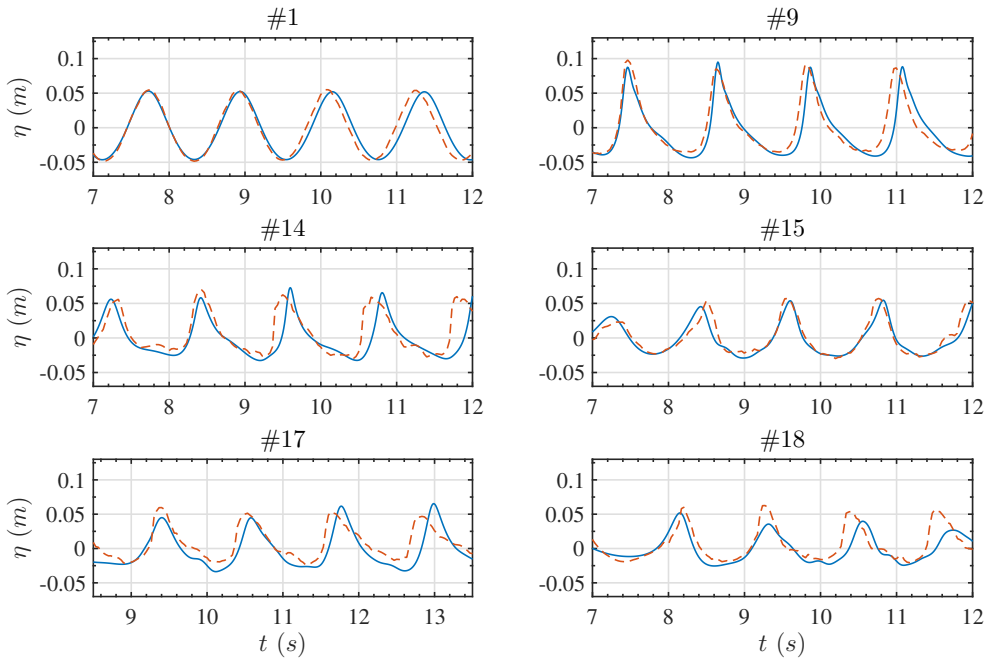

Figure 4.10: Propagation of periodic waves over a 3D bar for the plunging-breaking test case, $C6$ (Kamath et al. 2022). Time series of the free surface at selected gauges for the experiments (dashed line) and NWT simulations (solid line).

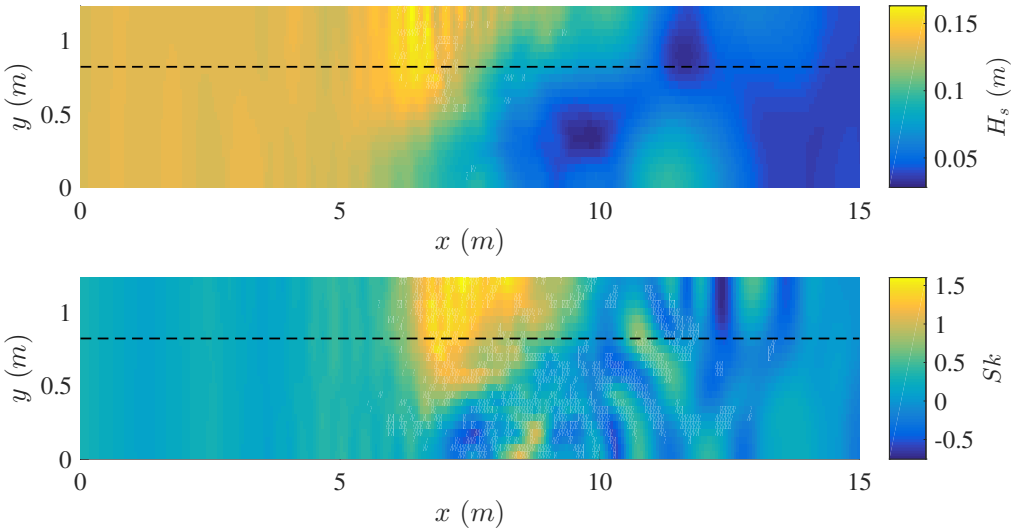

Figure 4.11: Propagation of periodic waves over a 3D bar for the plunging-breaking test case, $C6$ (Kamath et al. 2022). Spatial distribution of H_s and Sk computed from simulation results for a duration of 4 wave periods after a steady state is reached. The two quantities are plotted along the dashed line in Fig. 4.12 (b). Absorbing beach is present for $x \geq 12.5\,\mathrm{m}$.

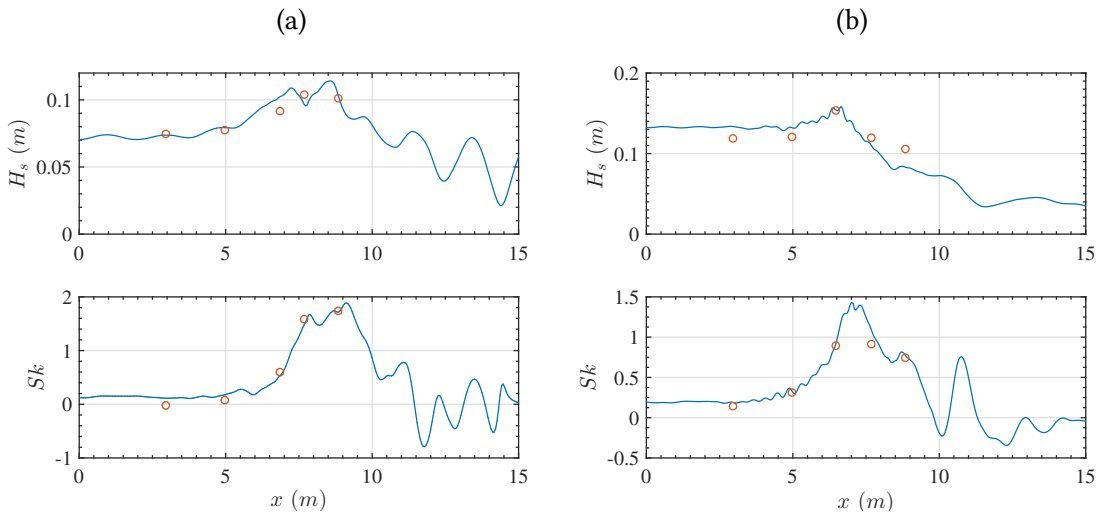

Figure 4.12: Propagation of periodic waves over a 3D bar for test cases (Kamath et al. 2022) : (a) $C4$ spilling breaking; and (b) $C6$ plunging breaking. Comparison of the spatial evolution of H_s and Sk along line $y = 0.822$ m in the NWT (solid line) and in the experiments (circles). Note: results in (b) correspond to Fig. 4.11. Absorbing beach is present for $x \geq 12.5$ m.

in case $C4$ (Fig. 4.12a) and the location of the local maxima in skewness for case $C6$ (Fig. 4.12b). Additional measurements after wave breaking are also needed to evaluate more quantitatively the optimal value of B_{off}.

Finally, Fig. 4.13 shows a quantitative comparison of the NWT results with the experimental measurements, for all the gauges, for the non-breaking, spilling, and plunging-breaking test cases $C1$, $C4$, and $C6$, respectively. Overall, a satisfactory agreement is observed with the experiments, except for a few gauges downstream and close to the walls for reasons explained in the previous spilling breaking test case.

4.4.2 Regular waves propagating over an elliptical shoal

Vincent & Briggs 1989 conducted a series of 17 experiments with monochromatic and irregular waves, both non-breaking and breaking propagating over an elliptical shoal, in a 35 m wide and 29 m long wave tank (see Fig. 4.14). Here, a regular breaking wave test case is simulated in the 3D-NWT, for which long-crested waves were generated in the x direction, in a depth of $h = 45.72$ cm, with $H = 13.5$ cm and $T = 1.3$ s (test case M3). For waves generated perpendicular to the wavemaker, both the shoal geometry and the wave field are symmetric about $y = 13.72$ m. Thus, half of the physical domain is represented in the NWT (numerical domain) for computational efficiency (see Fig. 4.14). Nine wave gauges measured the free surface position along Transect 4, which is located 3.05 m after the shoal, parallel to the wavemaker. The NWT is discretized with $\Delta x = \Delta y = 0.1259$ m, which yields $L/\Delta x \approx 20$ (where L is the wavelength at the wavemaker), $\Delta z = 0.076$ m, and $\Delta t = 0.021$ s. The domain extends from $0 \leq x \leq 17.5$ m and $0 \leq y \leq 13.72$ m, with the center of the shoal located at $x = 6.39$ m and $y = 13.72$ m. An absorbing beach is specified for $15.0\ m \leq x \leq 17.5$ m ($\approx L$ in length).

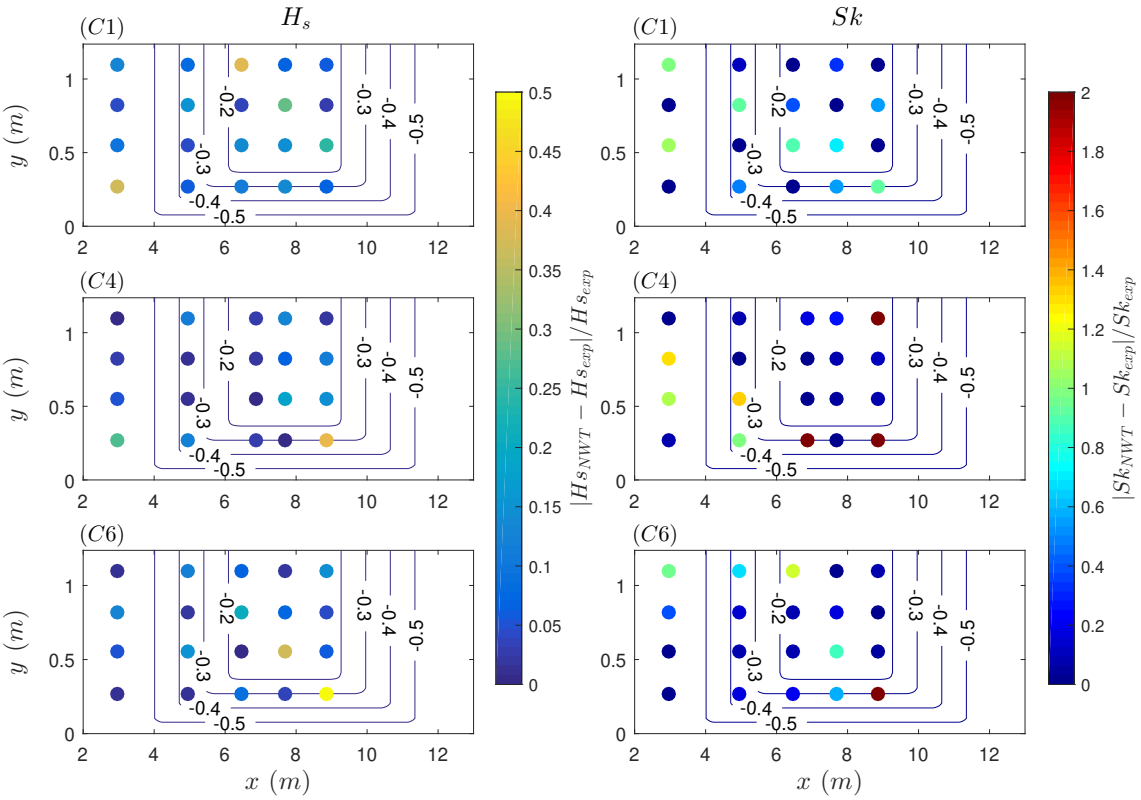

Figure 4.13: Relative difference of simulated wave statistics, H_s and Sk calculated for the test cases $C1$ (non-breaking), $C4$ (spilling breaking), and $C6$ (plunging breaking) from Kamath et al. 2022 with respect to the experiments and the bathymetric contour.

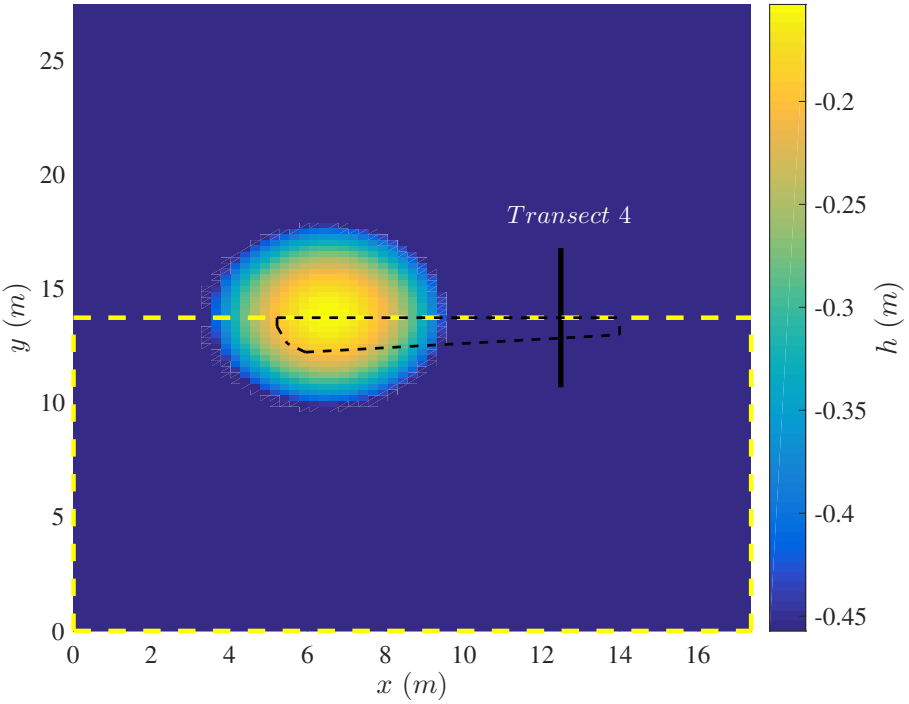

Figure 4.14: Bathymetry of the experiments of Vincent & Briggs 1989 for waves propagating over an elliptical shoal, with the wavemaker located at $x = 0$. Transect 4 (black solid line) marks the location of the wave gauge array in the experiments for this wave breaking test case. The dashed yellow rectangle indicates the computational domain used in the 3D-NWT. The region enclosed by black dashed lines indicates approximately where wave breaking crests were identified in the NWT simulations with $B_{\text{off}} = 0.05$.

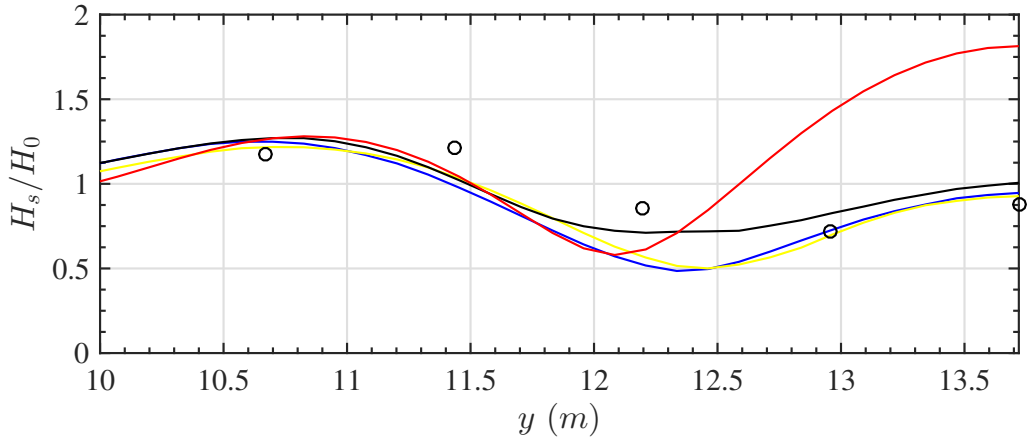

Figure 4.15: Simulation of periodic waves shoaling and breaking over a semi-elliptical shoal (Vincent & Briggs 1989). Comparison of the simulated (solid lines) and measured (circles) spatial evolution of H_s (averaged over 4 quasi-steady wave periods) along Transect 4 (Fig. 4.14) for different breaking termination criteria in the NWT: $B_{\text{off}} = 0.05$ (blue), 0.075 (yellow), 0.10 (black), and 0.30 (red).

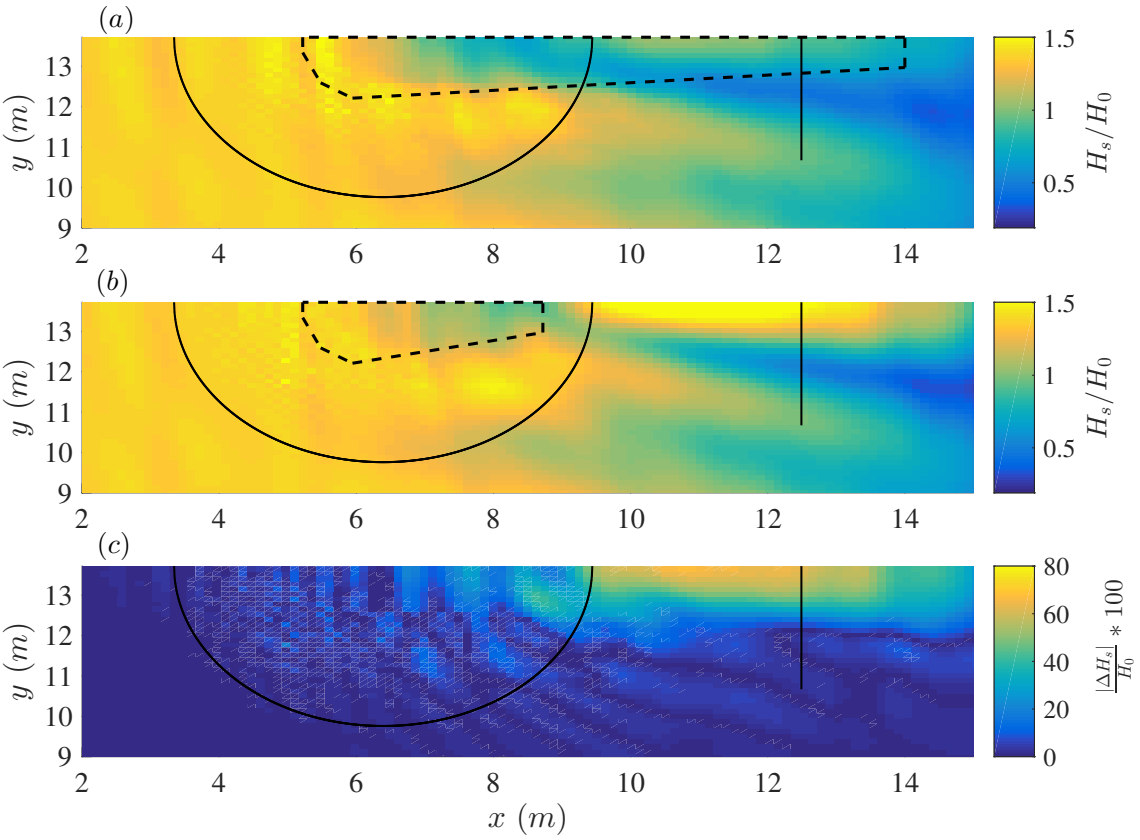

Figure 4.16: Spatial evolution of H_s (averaged over 4 quasi-steady wave periods) from simulations with $B_{\text{off}} = 0.05$ (a) and $B_{\text{off}} = 0.3$ (b). The relative error from the two normalized with H_0 is shown in (c). The semi-ellipse represents the toe of the shoal and the solid line, the measurement location of the wave gauge array in the experiments. The region enclosed by black dashed lines indicates approximately where breaking wave breaking crests were identified in the NWT.

In the simulations, as in the experiments, the regular waves shoal and break over the top of the elliptical shoal, and the wave breaking dissipation continues after the shoal (see black dashed line in Fig. 4.14). A comparison of the significant wave height normalized by the incident wave height at the wavemaker H_s/H_0 (calculated over 4 quasi-steady wave periods) shows good agreement for a range of termination criteria (Fig. 4.15), as long as the value of B_{off} is not too large.

Using the same termination criterion $B_{\text{off}} = 0.3$ as for the breaking cases of Kamath et al. 2022, Fig. 4.15 shows that the wave height is significantly overpredicted along the shoal axis (at $y = 13.72$ m). Thus, three additional termination criteria were tested, with $B_{\text{off}} = 0.05$, 0.075, and 0.1. Choosing a smaller value, $B_{\text{off}} = 0.05$ to 0.1, prolongs the duration of breaking and dissipation in the NWT, resulting in better agreement with the experiments. Fig. 4.16 shows spatial evolution of H_S from the NWT with $B_{\text{off}} = 0.05$ and 0.3 and the percentage difference between the two.

With $B_{\text{off}} = 0.05,\ 0.075,\ 0.1,$ and 0.3, the duration of wave breaking is respectively, $t_b = 4.01\ s,\ 3.34\ s,\ 3.27\ s,\ 2.52\ s$. From the free surface elevation at breaking onset, at $y = 13.72$ m, $T_b = 0.99\ s$, which yields $\tau = 0.74\ s$, which is much shorter than the breaking duration used in the NWT.

	H/d (onset)	H/d (termination)
$C4$ (spilling)	0.89	0.50
$C6$ (plunging)	0.98	0.62
Elliptical shoal	0.85 - 0.93	0.20

Table 4.2: The ratio of wave height to water depth (H/d), computed at breaking onset and termination for the breaking test cases considered in this study, using $B_{\text{off}} = 0.3$ for the submerged bar and $B_{\text{off}} = 0.05$ for the semi-elliptical shoal cases.

4.5 Conclusions and perspectives

Extending earlier 2D work, a novel parameterized method is proposed to model 3D depth-limited breaking wave onset and dissipation in an existing 3D-FNPF BEM numerical wave tank (NWT) (Harris et al. 2022). With this method, incident wavefronts are identified by splitting them into smaller patches whose physical properties are assumed to be approximately constant across their span, which enables considering these individual patches of wavefronts as locally 2D long-crested waves evolving towards breaking. The depth-limited wave breaking dissipation approach validated in a 2D-FNPF model by Mohanlal et al. 2023 is then used to model these piecewise 2D-approximated waves in the 3D-NWT.

The proposed model for parameterized 3D depth-limited wave breaking detection and dissipation is implemented in three steps: (i) detection of breaking onset using the universal criterion $B = u/c = 0.85$, originally proposed by Barthelemy et al. 2018 for deep and intermediate water cases and later validated by Derakhti et al. 2020 in shallow water conditions; (ii) calculation of the energy dissipation using an absorbing surface pressure, based on the assumption that depth-limited breaking waves are typically in a specific range of wave height to water depth ratios and instantaneous non-dimensional breaking strengths; and (iii) use of the parameter B to specify a termination criterion, which is calibrated in each specific test case. In this respect, Table 4.2 compares the wave height to depth ratios at breaking onset and termination, computed for all the breaking test cases examined in this study, using $B_{\text{off}} = 0.3$ for the submerged bar and $B_{\text{off}} = 0.05$ for the semi-elliptical shoal cases. The observed values of H/d mostly fall within the range $\approx [0.3,\ 1.0]$, suggested in Mohanlal et al. 2023 for the applicability of the constant non-dimensional breaking strength parameter, $\overline{b} = 0.05$.

The algorithm proposed in this study is tailored for Cartesian and quadrilateral (BEM) elements. Nevertheless, it has the potential to be adapted to other types of elements by modifying the definition of a crest unit accordingly. A robust boundary discretization method is critical to represent accurately the boundary of the numerical domain in the Boundary Element Method (BEM) used here to solve Laplace's equation, interpolating field variables, and calculating tangential derivatives along the boundary, as these are key to the accurate BEM solution and in the time updating algorithm.

In the NWT simulations, by employing higher-order, cubic B-splines (Harris et al. 2022), the model was found to be stable near and beyond breaking onset, even using a coarse mesh. For

simulations longer than several periods of breaking waves, however, the model became unstable, with the presence of high-frequency short waves that grew into sawtooth instabilities. This could be attributed to both a discretization that is too coarse, and also to the lack of a smoothing function in the model, to smooth variations in the absorbing pressure between the breaking and non-breaking regions. Such smoothing was found to be necessary to perform long simulations in 2D-FNPF-NWT (Mohanlal et al. 2023), and it should be straightforward to implement in the 3D-NWT in future work.

The proposed model is intended to approximate as closely as possible, within the limits of FNPF theory, the physics of breaking waves, in particular the energy dissipation and wave height decay resulting from breaking. In this work, this was achieved with physically-motivated choices of both the onset parameter and the dissipation model. Although the latter, with the choice of $\overline{b} = 0.05$ results from earlier 2D work that was validated with experiments (Mohanlal et al. 2023), the value of the termination criterion, upon which the duration of wave breaking t_b and the application of the absorbing pressure depends, still requires numerical calibration for each bathymetry considered here. If no calibration is possible, from the few 2D (from Mohanlal et al. 2023) and 3D wave breaking experimental test cases simulated, $B_{\text{off}} \in [0,\ 0.3]$ should be reasonable for a range wave conditions and bottom bathymetries (e.g., constant slope, submerged bar, elliptical shoal). However, future work should investigate further the moment of termination of breaking (or duration of breaking) as a function of wave parameters, with the aim of exploring the possibility of establishing a universal criterion for termination based on geometric, kinematic, or dynamic wave properties. Additional experimental measurements may be necessary to facilitate this analysis, with a particular focus on measurements downstream of wave breaking.

The grid resolution in this study was limited by the computational costs associated with the 3D-FNPF model, despite its recent improvement in efficiency (Harris et al. 2022). Several techniques have been developed to enhance the computational efficiency of FNPF models, often at the cost of sacrificing some of the accuracy. These techniques include using simplified Laplacian solvers or adopting weakly nonlinear free surface boundary conditions. For instance, the use of a Fast Multipole Method (FMM) as demonstrated in Harris et al. 2022 enables the faster solution of the Laplacian solver. By utilizing the test cases presented here as benchmarks, the dependence of the breaking model on computationally faster FNPF models can be investigated. This exploration will enable applying the breaking model to irregular waves in larger spatial domains over longer time periods.

Acknowledgment

This research was produced within the framework of Energy4Climate Interdisciplinary Center (E4C) of IP Paris and Ecole des Ponts ParisTech and was supported by the 3rd Programme d'Investissements d'Avenir [ANR-18-EUR-0006-02]. This action benefited from the support of the Chair « Challenging Technology for Responsible Energy » led by l'X – Ecole Polytechnique and the Fondation de l'Ecole Polytechnique, sponsored by TotalEnergies.

SG is gratefully acknowledging support from the US National Science Foundation grant #OCE-19-47960. The authors thank Arun Kamath and Betsy Seiffert for a copy of the 3D bar experimental data. The authors also thank Luc Pastur (ENSTA Paris) and Christophe Peyrard (EDF R&D LNHE) for helpful discussions.

Appendix 1: Identification of surface and crest units

To identify a crest unit i.e., a portion of wavefront represented by a discrete line segment, the set of points shown in Fig. 4.17 are examined. Here, the wave elevation is assumed to be zero at black points and one at a few hollow circles. Using Algorithm 1, $j = 1$ and $i = 2$ initially, and a peak is identified at $j = 1$ and $i = 9$. Then the quadrilateral element R_8 is identified in the surface unit, as well as its neighbors. Since R_8 has only 3 neighbors (R_7, R, R_5), the if statements are exited. Continuing to $j = 2$ and $i = 8$, the element R and its neighbors are identified, which in this case are R_1, ..., R_8. This set of elements (R, R_1, ..., R_8) and their nodes represent the first surface unit where a crest unit is identified. Proceeding to $j = 3$ and $i = 7$, the element R_1 is identified. However, since some of its neighbors are already included in a previous surface unit (in this case, the surface unit with elements R, R_1, ..., R_8), it is not considered to be a separate surface unit. This algorithm is followed until $i = 9$ and $j = 9$. As a result, three surface units are obtained, as shown in Fig. 4.17 with the symbols R, S, and T.

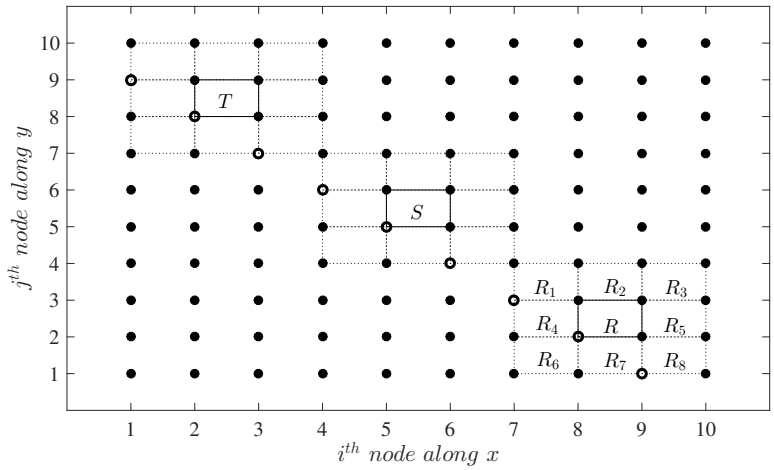

Figure 4.17: Example application of the surface unit identification Algorithm 1 to a set of Cartesian nodes in (x, y), with free surface elevation 0 (solid circles) and 1 (hollow circles). The rectangles with solid lines represent the elements chosen for peak detection, and the rectangles with dotted lines represent their neighboring elements.

Crest units are then calculated by first performing a local bi-cubic interpolation of the surface elevation η within a given 4 by 4 node surface unit, defined in a curvilinear coordinate system (ξ, χ) (Fig. 4.1), based on cubic polynomial shape functions. With $\mu \in [-1, 1]$ denoting either ξ or χ, the latter are standard and defined to satisfy the property: $N_p(\mu_p) = 1$ for $\mu_p = [-1, \ -$

$1/3,\ 1/3,\ 1]$ and $N_p(\mu_q) = 0$ for $p \neq q$ $(p, q = 1, ..., 4)$.

Accordingly, the shape functions and their first derivative are,

$$\begin{aligned}
N_1(\mu) &= \frac{1}{16}(1-\mu)(9\mu^2-1) \quad ; \quad N_1'(\mu) = \frac{1}{16}(-27\mu^2+18\mu+1) \\
N_2(\mu) &= \frac{9}{16}(1-\mu^2)(1-3\mu) \quad ; \quad N_2'(\mu) = \frac{1}{16}(9\mu^2-2\mu-3) \\
N_3(\mu) &= \frac{9}{16}(1-\mu^2)(1+3\mu) \quad ; \quad N_3'(\mu) = \frac{1}{16}(-9\mu^2-2\mu+3) \\
N_4(\mu) &= \frac{1}{16}(1+\mu)(9\mu^2-1) \quad ; \quad N_4'(\mu) = \frac{1}{16}(27\mu^2+18\mu-1)
\end{aligned} \tag{4.14}$$

and,

$$\eta(\xi, \chi) = \sum_{i=1}^{16} N_p(\xi) N_q(\chi)\, \eta_i \tag{4.15}$$

where $p = 1 + (i-1) \mod 4$ (with $\mod$ denoting the modulo operator), $q = \lceil i/4 \rceil$ and η_i denotes the surface elevations at nodes i arranged as shown in Fig. 4.1a.

In the local coordinate system, the crest unit/wavefront is defined as the locus of points (ξ_{Ck}, χ_{Ck}) $(k = 1, ..., e)$ that satisfy,

$$\frac{\partial \eta}{\partial \xi}(\xi, \chi) = \sum_{i=1}^{16} N_p'(\xi_{Ck}) N_q(\chi_{Ck})\, \eta_i = 0 \tag{4.16}$$

where the prime symbols denote the first derivative. In each surface unit, these equations are evaluated over 11 points along χ for $\chi \in [-1,\ 1]$ (this choice of number of points results from a trade-off between accuracy and computational time). In other words, the points (ξ_{Ck}, χ_{Ck}) represent locations where the spatial gradient of the free surface becomes zero in a horizontal direction, indicating the presence of peaks at the free surface. A typical wavefront/crest unit is shown in Fig. 4.1b, and an example of wavefronts assembled at arbitrary time t in a complete wave field is shown in Fig. 4.2. The algorithm implemented to determine surface units and calculate their crest units is summarized in Algorithm 1.

Algorithm 1 The algorithm used to obtain crest units

Create an empty list of crest units $\mathcal{L}^t$
for j = 1 to m-1 **do** ▷ m, the number of nodes along y
  for i = 2 to n-1 **do** ▷ n, the number of nodes along x
    if $\eta(i-1,j) < \eta(i,j) > \eta(i+1,j)$ **then** ▷ is peak?
      Find element R with $\eta(i,j)$ as the bottom-left node elevation
      if R has 8 neighbor elements not considered in $\mathcal{L}^t$ **then**
        Identify the 16 nodes of this surface unit
        Arrange the nodes as shown in Fig. 4.1 (a)
        Do Bi-cubic fit from Eqs. 4.14
        Obtain the set of points $(\xi_{\mathcal{C}k}, \chi_{\mathcal{C}k})$ using Eqs. 4.16
        Add the new crest unit to the list $\mathcal{L}^t$
      end if
    end if
  end for
end for

Chapter 5

Conclusions and perspectives

L'objectif de cette thèse etait de faire progresser les modèles numériques existants utilisés pour simuler les états de la mer à l'échelle d'un parc éolien, en simulant avec précision les vagues déferlantes dans des modèles de type potentiel. Cette thèse présente une modélisation générale et relativement simple de la détection et de la dissipation du déferlement des vagues, à profondeur et à cambrure limitées, y compris les déferlantes déversantes et plongeantes, à la fois en 2D et en 3D. Le modèle proposé est validé par rapport à plusieurs expériences de déferlement de vagues de la littérature. Le critère de terminaison du modèle de déferlement est reconnu comme un aspect qui n'a pas été examiné en profondeur, et une piste potentielle pour son amélioration est proposée. Quelques idées initialement prévues pour être incluses dans cette thèse mais qui n'ont pas été pleinement explorées en raison de contraintes de temps sont examinées et discutées.

5.1 Summary

The rapid expansion of the renewable energy sector in Europe, driven by ambitious targets set by the European Union (EU), to achieve carbon neutrality in the coming decades, has led to an increased focus on offshore wind energy. This particular sector, which involves both floating and fixed wind turbines, has gained considerable attention due to the abundance of coastal areas and vast water-covered regions across Europe. Consequently, extensive research has been conducted to gain a deeper understanding of the evolution of sea states. The objective of this thesis was to advance the existing numerical models used for simulating site-scale sea states associated with offshore wind energy, by accurately simulating breaking waves in numerically simple models (in this study the FNPF models).

Based on driving physics, breaking waves can be classified into two main categories, namely depth-limited waves, which occur due to shoaling, and steepness-limited waves, which result from the concentration of energy at a specific point. In both cases, a parameterized wave breaking model consists of three essential steps. Firstly, the onset of wave breaking, which is the moment when waves are deemed to start breaking, is identified. Next, the amount of energy that needs to be dissipated is calculated. Lastly, a termination criterion is applied to determine when to stop the dissipation process.

In this study, the onset of wave breaking is determined by a universal criterion proposed by Barthelemy et al. 2018 and Derakhti et al. 2020, which states that a crest with a ratio of horizontal particle velocity, denoted as u, to crest velocity, denoted as c, exceeding a critical value of $B = u/c = 0.85$, will break. The study of 2D depth-limited breaking waves demonstrated that this criterion accurately predicted the onset of breaking, closely matching the results of spilling (white foam spilling down the front face of the wave) and plunging (overturning jet on the front face of the wave) breaker experiments reported in the literature. Additionally, for steepness-limited breaking waves, the free surface elevation at the moment of breaking onset corresponded to the instant when the free surface becomes nearly vertical. This is important as starting to apply dissipation after this point can lead to numerical instabilities. Therefore, this criterion serves as a reliable predictor of breaking onset, providing valuable insights into wave behavior.

The dissipation from wave breaking is performed in two steps. First, the non-dimensional breaking strength parameter (b) is computed, which determines the instantaneous power to be dissipated. Secondly, this power is modeled as an absorbing pressure acting across the breaking crest, following the approach described in Guignard & Grilli 2001. In the case of depth-limited breaking, a new model for dissipation strength is proposed. For steepness-limited dissipation, the dissipation strength predicted in Romero et al. 2012, which is a function of the maximum linear wave steepness, is employed.

For 2D depth-limited breaking waves, the non-dimensional breaking strength (b) was determined using the hydraulic jump (HJ) analogy initially introduced by Hansen & Svendsen 1979 and Stive 1984 for spilling breakers. It was observed that the value of b exhibited a relatively narrow range, centered around 0.05, for various types of breaking, including spilling and plunging breakers.

Furthermore, the ratio of wave height to water depth, κ, at the breaking onset was found to fall within the range of $[0.7,\ 1.2]$, consistent with the findings of Battjes 1974; Dean & Dalrymple 1991; Mei 1989 for depth-limited breaking waves in general. By analytically demonstrating that the instantaneous value/magnitude of b predominantly lies within this narrow range under shallow water and mild slope assumptions, a proposition that b maintains a similar order of magnitude for depth-limited breakers in general, is made. Based on this reasoning, simulations of spilling and plunging depth-limited breaking waves were conducted using a constant breaking strength of $b = 0.05$. The simulation results obtained using this constant value for b showed good agreement with experimental measurements, falling within the range of experimental uncertainty.

The proposed 2D unified model for depth-limited breaking dissipation is further extended to 3D depth-limited breaking waves. This extension involves dividing 3D long or short-crested waves into smaller sections of wavefronts, where the physical characteristics remain relatively constant in the spanwise (along-crest) direction. This approach allows us to treat these individual patches of wavefronts as 2D long-crested waves. This approach is tested for laboratory experiments from the literature of spilling and plunging breaking waves over a 3D submerged bar and an elliptical shoal. Good results are obtained in comparison with the experiments.

A flowchart briefly describing the parameterized wave breaking model proposed in this study is as follows,

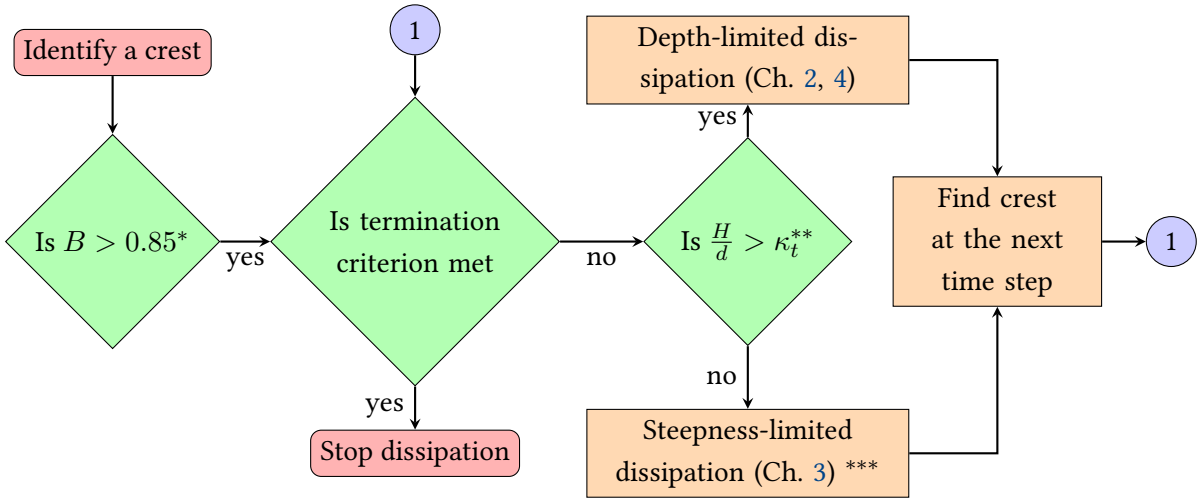

* Barthelemy et al. 2018; Derakhti et al. 2020

** $\kappa_t \in [0.4 - 0.7]$, a threshold set by studying κ at the breaking termination, in Chapter 2

*** assuming that the input linear wave steepness is known or can be estimated

5.2 Perspectives

It is crucial to respect the potential flow validity throughout the domain for the test case that is aimed to be studied, with the exception of regions where breaking waves occur, which are addressed by the developed parameterized models presented here. However, there are instances

where the flow leading to breaking waves may not strictly adhere to the potential flow regime. For instance, in the case of flow over a step, as modeled in the 2D NWT by Grilli et al. 1992, slight overprediction of wave heights was observed. This discrepancy can be attributed to energy dissipation resulting from flow separation over the step and vorticity observed in the experiments which is not accounted for in the NWT. Hence, it is necessary to employ an appropriate numerical model that encompasses the full physics of the specific test case under consideration. Among such phenomena of interest for coastal applications include the modeling of runup and breaking waves in the presence of currents.

The breaking strength (b) for steepness-limited breaking waves is determined based on the input maximum linear wave steepness using the empirical curve proposed by Romero et al. 2012. This approach is suitable for simulating laboratory test cases where the input conditions are known, as demonstrated in Chapter 3. However, when dealing with irregular sea conditions, it becomes impractical to determine b using this method. Therefore, alternative empirical laws are needed to estimate b, such as the one proposed by Derakhti, Banner & Kirby 2018, who provide an empirical curve for b with respect to the wave conditions at the onset of breaking.

For the cases in Chapter 2, for depth-limited breaking waves, the parameter γ (representing an intensity of breaking onset) seemed to be larger for plunging breakers relative to spilling breakers, with the separation threshold of $\gamma \in [1.3 - 1.4]$. However, to establish a general value to be used, a broader range of test cases needs to be explored in further research.

In all the tested cases, the termination of wave breaking was determined by comparing simulated and measured free surface elevation as a function of the parameter, B. For breaking waves over a bar, the optimal value of B_{off} was found to be 0.3. On a slope, the breaking dissipation continued until the end of the slope. In the case of focused waves, the optimal value of B_{off} was 0.4. It is evident that the criterion B cannot be universally applied as a termination criterion. To explore the possibility of establishing a universal termination criterion based on geometric, kinematic, or dynamic wave properties, one may investigate the wave conditions at the moment of breaking termination for all the calibrated cases in this study.

The thesis aimed to develop a modeling approach for simulating breaking waves for offshore applications at site-scale domains. In the case of two-dimensional scenarios, two irregular sea states on larger domains, such as a domain size of $60\ m$ for simulating the test case of Adytia et al. 2018, were examined. However, for three-dimensional cases, the analysis was limited to regular breaking test cases simulated over a short time period. This constraint was attributed to the time-consuming nature of the NWT. Therefore, to study irregular breaking waves in large domains, a more efficient wave model is necessary. This could involve either enhancing the performance of the 3D NWT or considering a relatively simpler model that can provide faster results.

5.2.1 Periodic breaking waves with runup

In experiments involving periodic waves breaking over a sloping beach (e.g., Hansen & Svendsen 1979; Ting & Kirby 1994), as the waves approach the shore, they undergo shoaling, causing them to break on the sloping beach. This breaking action continues as the water depth gets more and more shallow. Eventually, a phenomenon known as runup takes place. Runup refers to the process where the waves rush up the beach, resulting in a rise in water level above the level of still water.

However, as seen in Chapter 2 for the test cases of Hansen & Svendsen 1979 and Ting & Kirby 1994, once the water depth reaches a certain shallow threshold, the simulated bathymetry transitions into deeper depths and eventually levels off at a constant depth where waves are absorbed. This approach is adopted as experimental measurements of surface elevation beyond this threshold shallow depth are not available. Thus the modeling of wave runup is not necessary in this context.

The modeling of runup for solitary waves on steep slopes has been addressed in the work of Grilli & Svendsen 1990*a*. Here an attempt was made to extend this modeling approach to incorporate runup for periodic breaking waves on relatively gentler slopes in the NWT. The tip of the free surface and the bottom of these cases make very sharp angles that can lead to numerical instabilities. To overcome this issue, a new method was implemented to distribute nodes near the intersection of the free surface and bottom. At each time step, the spatial distribution of nodes close to these intersections followed a geometric progression, with the smallest distance occurring near the tip of the intersection, as shown in Fig. 5.1.

Fig. 5.2 shows the free surface and the bottom for the Hansen & Svendsen 1979 breaking test case, for four different time instants, each two wave periods apart. The model is stable for a few wave periods, however, as the runup distance keeps increasing, the model becomes unstable due to the sharp corner at the free surface and the bottom intersection (Fig. 5.2, bottom-right). It is challenging to determine precisely when the breaking dissipation process becomes less dominant and the influence of bottom friction (which is not included in the FNPF models used here) becomes more significant. Also, the wave crests become very coarse close to the tip and the identification of crests and troughs here gets complicated. Therefore, an approach could be to decide on a critical depth or depth-to-wavelength ratio, after which it is assumed that the dissipation is dominated by the bottom friction and model this dissipation for the entire free surface from this point up to the tip.

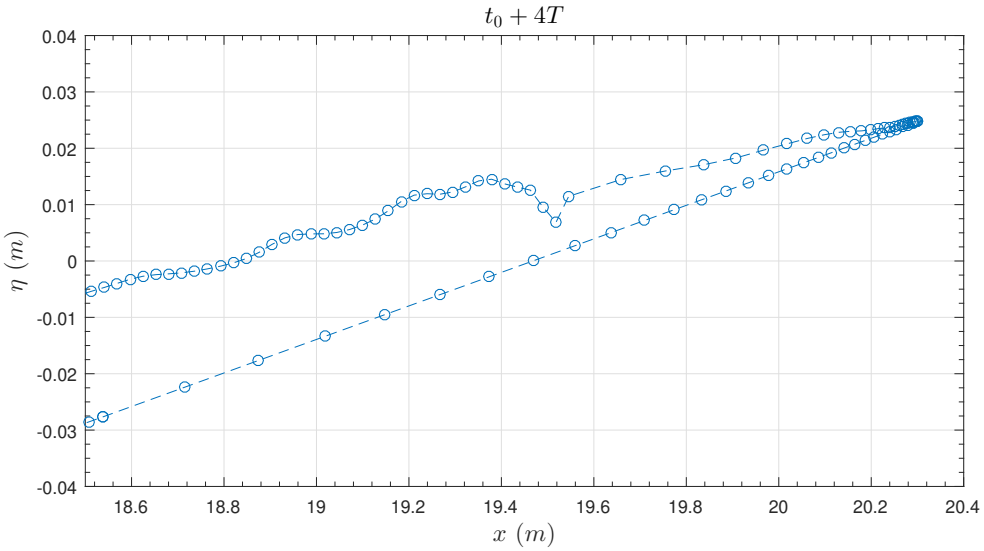

Figure 5.1: A close-up of the periodic wave breaking test case of Hansen & Svendsen 1979 at the runup. Circles indicate the position of nodes.

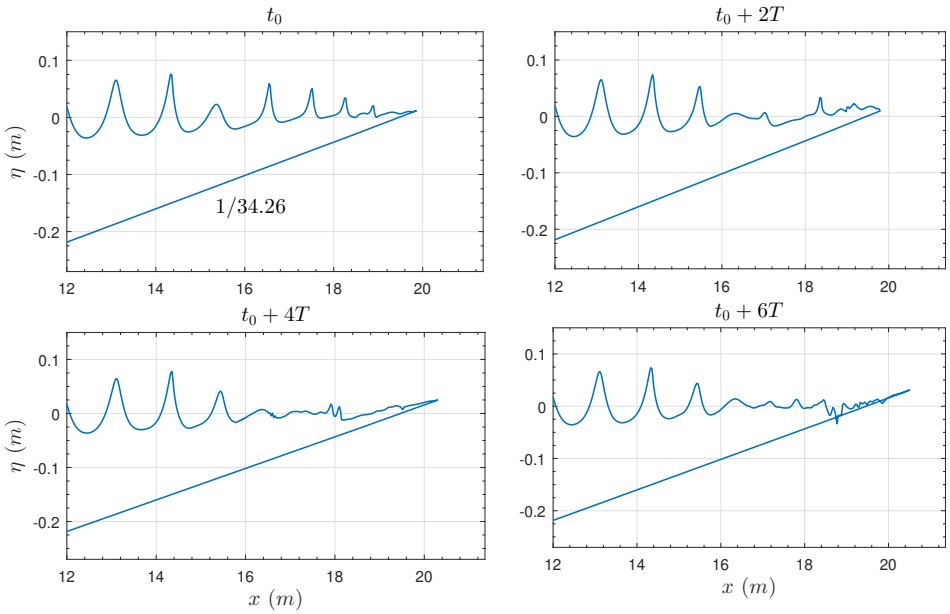

Figure 5.2: The periodic wave breaking test case of Hansen & Svendsen 1979, with runup for four different time instants.

5.2.2 3DWaveBI

One of the objectives of this thesis set in the beginning was to conduct experiments involving regular and irregular waves breaking on a scaled-down $(1/40)$ model of a dune, with and without the presence of a fixed monopile. The chosen bathymetry represents a simplified dune profile,

consisting of a gentle upslope, a region of constant depth, and a relatively steep downslope. Two different upslope ratios, namely 1/25 and 1/12 (Fig. 5.3), were selected for this investigation. The height of the dune, measured from the base of the downslope to the shallowest depth was $0.5\ m$. A monopile was installed at the shallowest depth (the black circle in Fig. 5.3). The water depths at the wavemaker were to be taken as $0.8\ m$ and $0.7\ m$ for performing various regular and irregular (JONSWAP) test cases. The constructed bathymetry of this dune is shown in Fig. 5.4.

The planned measurements comprised recording free surface elevations at 18 gauge locations, capturing videos of the wave field using a high-resolution overhead camera (12 MP) to identify regions with breaking waves, employing a side view camera with a high acquisition frequency to observe the wave shape upon impact on the monopile, and recording forces of breaking waves imparted on the monopile at a high frequency ($1\ kHz$).

Upon construction of the bathymetry, two interns, Arthur Guidel and Gabriel Dreysse, recorded a data set for the first run for an irregular JONSWAP spectrum for a few minutes. From the following day until the present moment, a problem encountered with the wavemaker is being resolved, rendering it impossible to proceed with any additional experiments. As a result, the experiments remain indefinitely postponed.

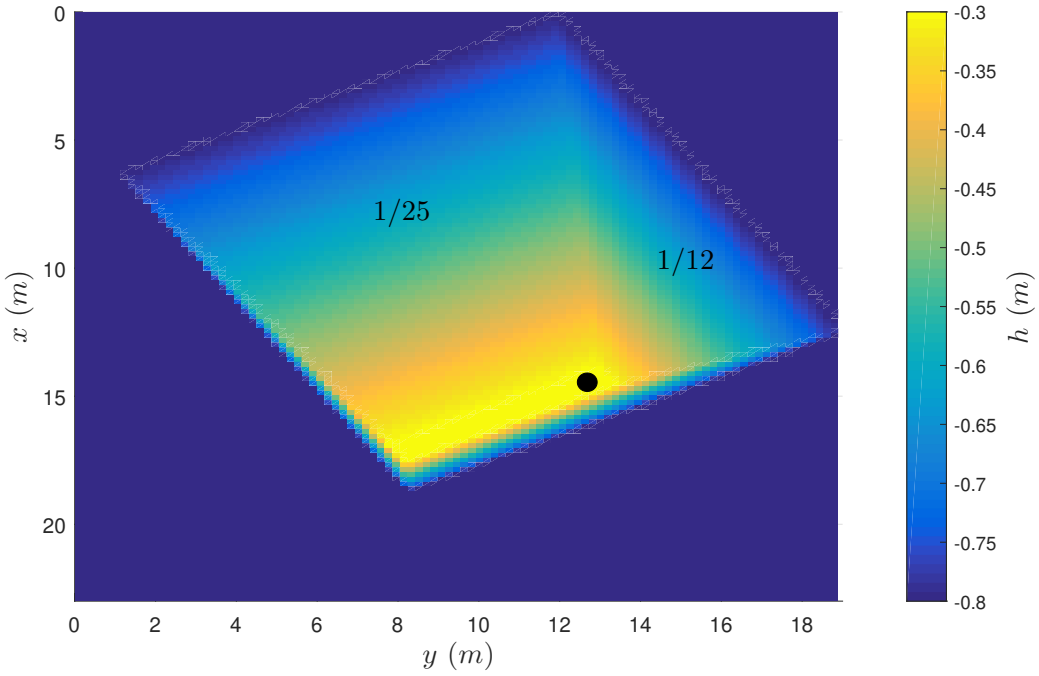

Figure 5.3: Schematic of the bathymetry at Chatou used in the NWT with the black circle representing the location of the monopile, wavemaker at $x = 0$.

On the numerical side of this objective, a periodic test case was run in the NWT to understand and get a first estimation of where breaking regions might be seen in the wave tank. A sufficiently large wave was selected, ensuring that it would break on the dune. In Fig. 5.5, the bathymetry in

Chatou along with a wave field from the periodic wave at an instant of breaking is shown. Three crest units near the top of the bar were identified as breaking, and the corresponding region where a damping pressure due to breaking is applied is visualized using a colormap indicating the quantity $P_b\phi_n$ (integrated over the breaking region gives the total energy dissipated), where P_b represents the damping pressure accounting for wave breaking, and ϕ_n is the normal velocity. Qualitatively, the identified breaking region from simulation (Fig. 5.5) appears to be similar to the one observed in an experimental test shown in Fig. 5.6 (note: the input conditions are not the same for the two cases).

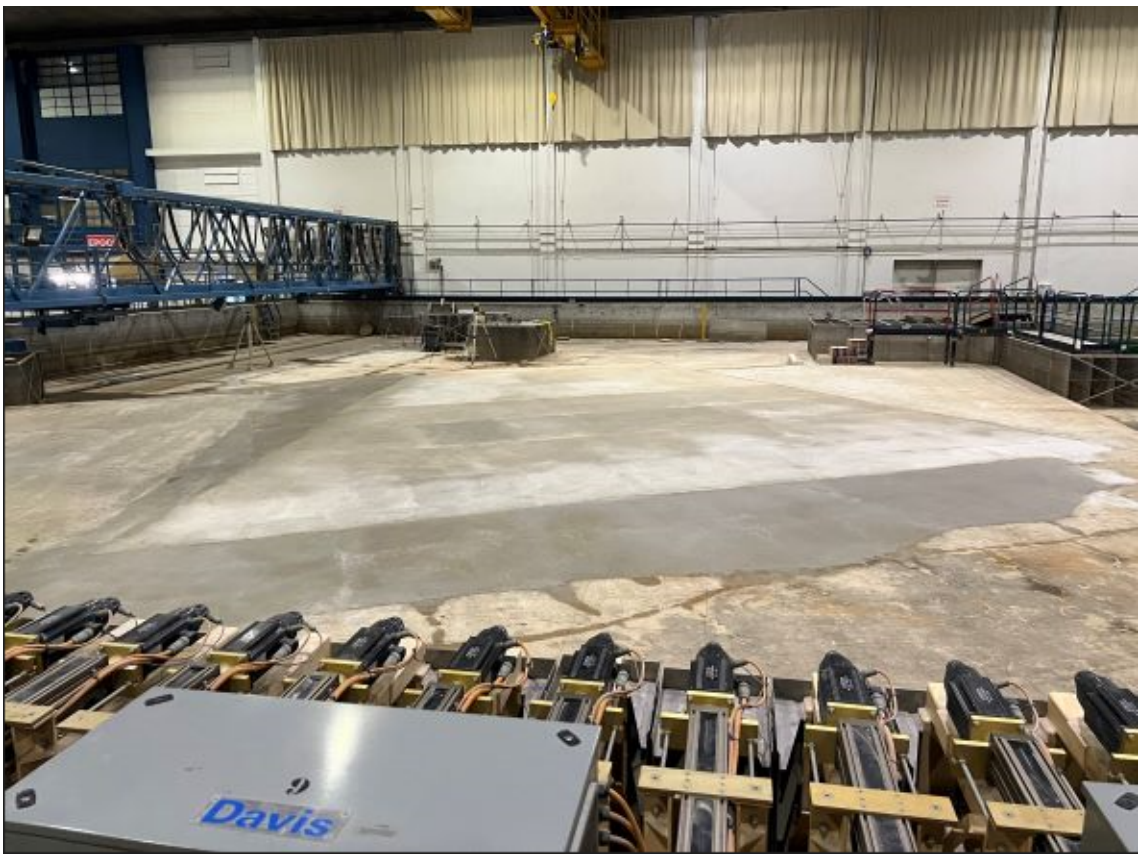

Figure 5.4: The constructed bathymetry as part of 3DWaveBI, in the wave tank at Chatou. Wavemaker paddles can be seen at the bottom of the picture.

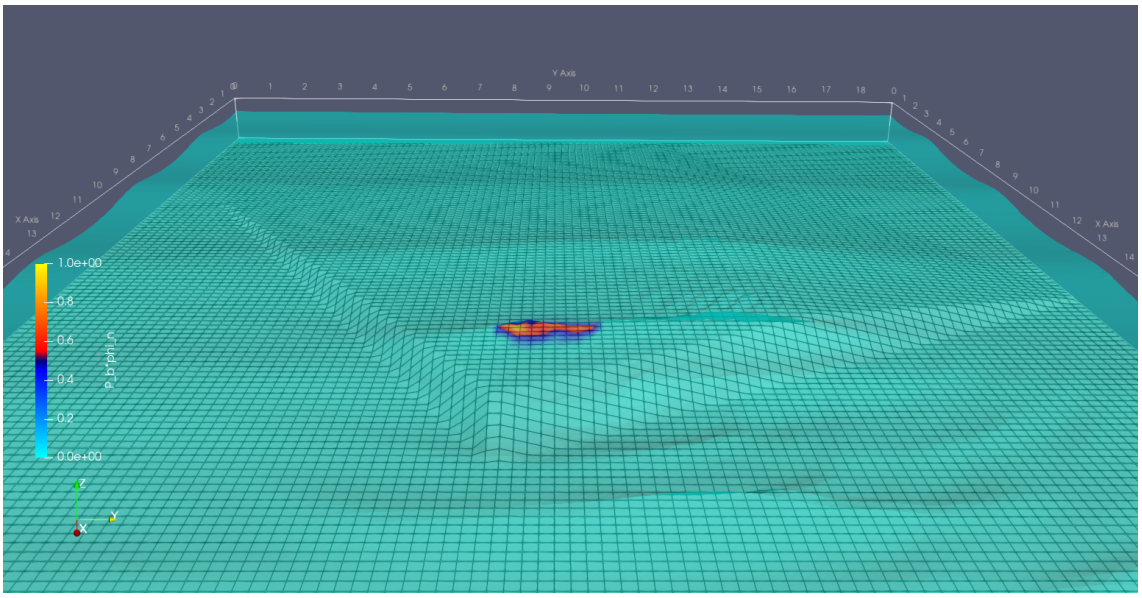

Figure 5.5: 3DWaveBI bathymetry (wavemaker at $x = 0$) with a wavefield from a periodic wave breaking on the bar (with an Iribarren number, $\xi_0 = 0.25$, for a $1/25$ slope, corresponding to a spilling type breaker) from the NWT results. The colored quantity is $P_b\phi_n$ (units in $\mathrm{m}^3\mathrm{s}^3$), where P_b is the damping pressure accounting for wave breaking and ϕ_n is the normal velocity.

5.2.3 Detection of breaking waves

For the planned wave breaking experiments, it was necessary to develop a method to identify the breaking regions in the wave tank. Typically, this would involve detecting the brightest pixels. However, in the facility at Chatou, there were additional bright pixels scattered around due to the presence of bright spotlights on the ceiling (as shown in Fig. 5.6, left). Therefore, a more accurate method was desired to precisely identify the breaking regions.

For this purpose, a set of kernels was designed such that the original images convoluted with these kernels would result in an image that would identify bright spots as only the ones from breaking waves. The first kernel is a 2D normal distribution kernel (Fig. 5.7) of size l (in this case $l = 50$). This operation will lower the magnitude of pixels present in areas where small patches of bright pixels are present. This diffusion will be relatively lower at regions where a cluster of bright pixels is present (i.e., the regions with breaking waves). This image is further convoluted by a series of four edge detection kernels (since an edge detection kernel is direction dependent). For detecting vertical edges from the left to the right of an image, this kernel is, with $\epsilon = 0.1$,

$$\begin{bmatrix} 1 & 0 & -1 \\ 1 & \epsilon & -1 \\ 1 & 0 & -1 \end{bmatrix}.$$

For vertical edges from the right to the left, this kernel is,

$$\begin{bmatrix} -1 & 0 & 1 \\ -1 & \epsilon & 1 \\ -1 & 0 & 1 \end{bmatrix}.$$

Similarly, for detecting horizontal edges from the top to the bottom of an image, this kernel is,

$$\begin{bmatrix} 1 & 1 & 1 \\ 0 & \epsilon & 0 \\ -1 & -1 & -1 \end{bmatrix}.$$

For horizontal edges from the left to the right, this kernel is,

$$\begin{bmatrix} -1 & -1 & -1 \\ 0 & \epsilon & 0 \\ 1 & 1 & 1 \end{bmatrix}.$$

Fig. 5.6, middle, is obtained after the total of 5 convolutions (convoluted one after the other), and scaling the pixels such that the brightest ones remaining are equal to 255. Finally, a threshold (p_{th}) is set (in this case $p_{th} = 250$) above which the pixels are denoted as breaking regions (yellow pixels in Fig. 5.6, right). The calibrated parameters utilized in this study were determined using an initial set of test images. While these parameters could be further optimized by analyzing a larger data set, it should be noted that this method is specifically designed for the problem at hand (bright pixels scattered around due to the presence of bright light spots on the ceiling) and may not be applicable to other types of cases. For a more general approach, one could consider analyzing the images in time.

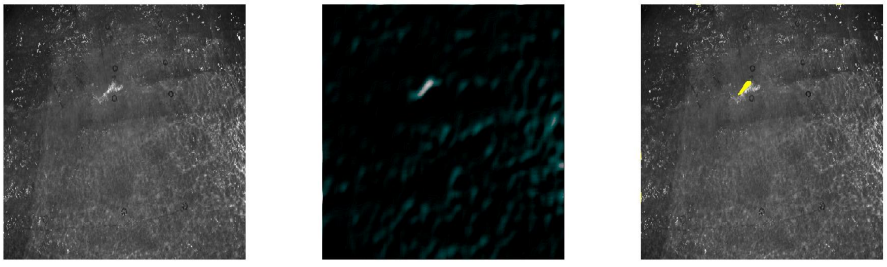

Figure 5.6: Left: an overhead picture of a wavefield (wavemaker located at the bottom of the images). Middle: the final convoluted image. Right: the initial picture with breaking region identified as the yellow colored pixels.

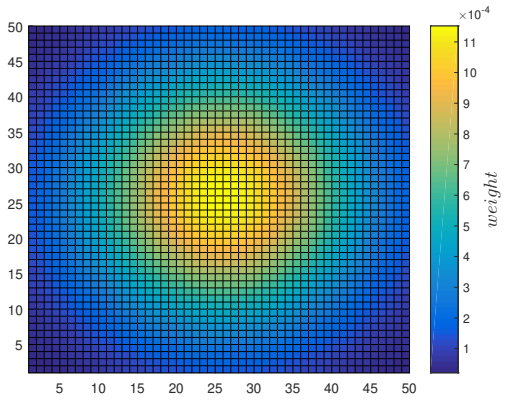

Figure 5.7: A 2D normal distribution kernel with 50×50 elements. The sum of all the weights is equal to 1.

5.3 Closing remarks

This thesis introduced a parameterized wave breaking model that is based on the known physics of wave breaking, including the breaking onset and dissipation. This model is validated for a range of 2D test cases with variable bathymetries without requiring any calibration, except for the termination criterion. Additionally, a straightforward numerical implementation method is presented to extend the model to 3D, and is validated with experiments from the literature. The accurate calculation of the phase speed forms the foundation of this model, used for both the accurate identification of onset and the magnitude of energy dissipation.

Appendix A

4^{th} B'WAVES (Virtual, June 16-18, 2021)

Depth-limited wave breaking dissipation in a potential flow code

SUNIL MOHANLAL,[1] MARISSA YATES,[1,2] AND JEFFREY C. HARRIS [1]

[1] *LHSV, Ecole des Ponts, Cerema, EDF R&D, Chatou, France*
[2] *Cerema, Risks, Water and Seas, Compiègne, France*

Abstract:
Simulation of waves beyond the breaking point in a fully non-linear potential flow model (e.g. Raoult et al. [1]) is considered with a semi-empirical dissipation term that requires correctly determining the breaking onset and estimating the energy dissipation rate. A kinematic breaking criterion, similar to those found recently to be practical for arbitrary water depth (e.g. Derakthi et al. [2]), is applied here. The criterion is based on U/C, the ratio of the free surface water velocity to the wave phase speed. To estimate the wave breaking strength in shallow water, previous work by Svendsen et al. [3] that continues to be used and developed (e.g. Grilli et al. [4]), has shown that a hydraulic jump model can provide a reliable approach for spilling shallow water breakers. Alternatively, Derakthi et al. [5] proposed a parameterization for the breaking strength in deep and intermediate water depending on the rate of change of U/C. Here, a range of depth-limited wave breaking cases for regular and irregular waves are considered and validated with experimental measurements, and values for the rate of change of U/C and the breaking strength are calculated for shallow water cases. Current work includes exploring if and how these different parameterizations may be combined to develop a unified approach to be applied in fully nonlinear potential flow models.

References

1. C. Raoult, M. Benoit, and M. L. Yates, "Validation of a fully nonlinear and dispersive wave model with laboratory non-breaking experiments," Coast. Eng. **114**, 194–207 (2016).
2. M. Derakhti, J. T. Kirby, M. L. Banner, S. T. Grilli, and J. Thomson, "A unified breaking onset criterion for surface gravity water waves in arbitrary depth," J. Geophys. Res. Ocean. **125** (2020).
3. I. Svendsen, P. Madsen, and J. B. Hansen, "WAVE CHARACTERISTICS IN THE SURF ZONE," (Coastal Engineering Research Council, 1978), p. 29.
4. S. T. Grilli, J. Horrillo, and S. Guignard, "Fully nonlinear potential flow simulations of wave shoaling over slopes: Spilling breaker model and integral wave properties," Water Waves **2**, 263–297 (2019).
5. M. Derakhti, M. L. Banner, and J. T. Kirby, "Predicting the breaking strength of gravity water waves in deep and intermediate depth," J. Fluid Mech. **848** (2018).

Appendix B

18^{th} Journées de l'Hydrodynamique (JH, Poitiers, France, November 22-24, 2022)

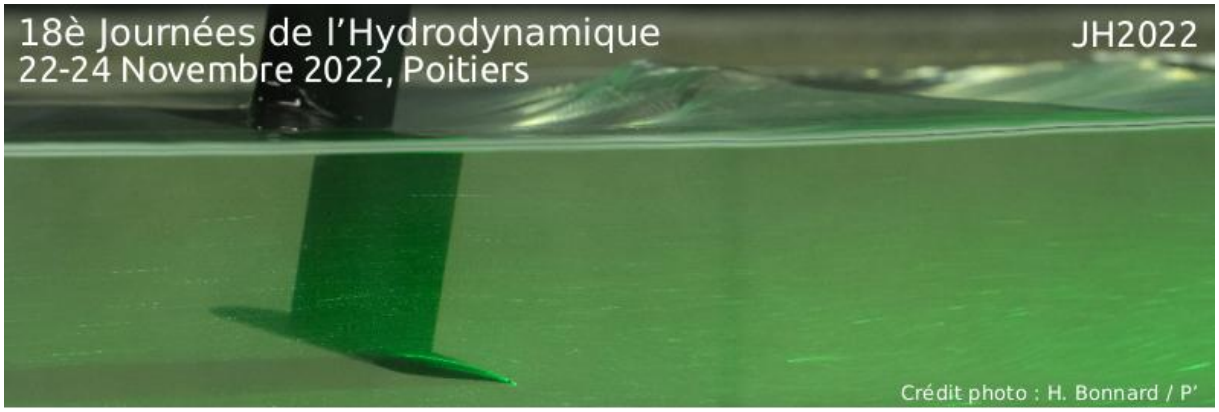

AMELIORATION DE LA MODELISATION 3D DE VAGUES DEFERLANTES EN MILIEU MARITIME

IMPROVEMENT OF THE 3D MODELING OF BREAKING WAVES IN A MARITIME ENVIRONMENT

J.C. HARRIS[(1)], M.L. YATES[(1,2)], S. MOHANLAL[(1)], L.R. PASTUR[(3)], C. PEYRARD[(1,4)], C. BUVAT[(1,4)], S.T. GRILLI[(5)] G. DREYSSE[(1)], A. GUIDEL[(1)], J. WANG[(1)]

jeffrey.harris@enpc.fr ; marissa.yates@cerema.fr ; sunil.mohanlal@enpc.fr
luc.pastur@ensta-paris.fr ; christophe.peyrard@edf.fr ; clement.buvat@edf.fr ; grilli@uri.edu
gabriel.dreysse@ensta-paris.fr ; arthur.guidel@ensta-paris.fr ; jiankai.wang@eleves.enpc.fr

[(1)]LHSV, Ecole des Ponts, EDF R&D, Chatou, France
[(2)]Cerema, Risk, Water, Sea and Coast, Compiègne, France
[(3)]Unité de Mécanique, ENSTA Paris, Institut Polytechnique de Paris, Palaiseau, France
[(4)]EDF R&D, Laboratoire National d'Hydraulique et Environnement, Chatou, France
[(5)]Department of Ocean Engineering, University of Rhode Island, Narragansett, RI, USA

Résumé

Une représentation précise de la propagation de vagues en trois dimensions en zone maritime et côtière reste un défi ouvert du fait de plusieurs verrous scientifiques et techniques à lever. Avec le développement des énergies en mer, et en particulier l'éolien offshore (ou les convertisseurs d'énergie de vagues), un intérêt croissant est porté à l'estimation des efforts de vagues sur les structures. De plus, pour valider les modèles de propagation de vagues et des interactions vague-structure (e.g., [2, 3]), il existe une manque d'observations précises du champ 3D de vagues (e.g., hauteurs et statistiques du déferlement) et de leurs impacts (efforts) sur des structures [1].

Ce projet est centré sur des travaux de recherche pour développer, améliorer et valider des nouvelles approches de modélisation numérique capable de simuler précisément et efficacement la propagation d'un champs de vagues jusqu'aux structures et ensuite les efforts d'ordre élevé de ces vagues sur des structures. Deux axes de travail sont en cours, consacrés au développement et à l'extension d'un modèle 3D complètement non-linéaire et dispersif de propagation de vagues et à la réalisation des essais en laboratoire pour de fournir des données de validation des modèles numériques.

Les essais en laboratoire ont pour objectif d'étudier la transformation des vagues sur une bathymétrie variable incluant les effets de dissipation d'énergie liée au déferlement,

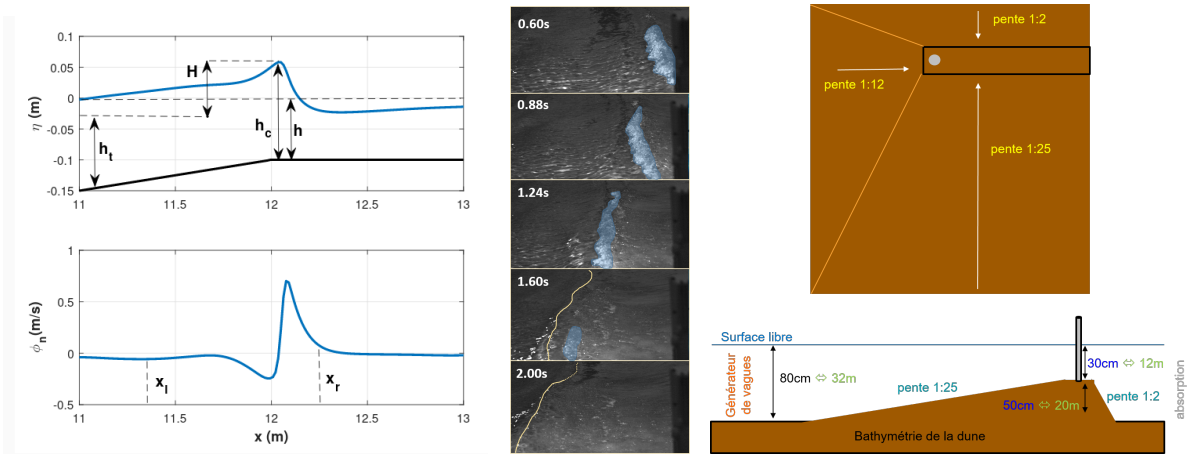

FIGURE 1 – Schéma 2D des paramètres d'une vague déferlante [3] (gauche) ; timestack des images d'une vague déferlante avec l'identification de la mousse générée (zones bleues) et d'une deuxième crête de vague (ligne jaune) avant déferlement (centre) ; et schéma 3D de la dune et de la position de la structure sur la dune (droite).

les statistiques de déferlement et les efforts des vagues (non-déferlantes et déferlantes) sur une structure en profondeur d'eau faible et intermédiaire. Une bathymétrie variable représentant une forme de "dune" schématique (Fig. 1) a été construite. Dans le cas des essais avec la présence d'un une structure, un monopile cylindrique, représentative d'un éolien fixe, est positionnée à la crête de la dune (Fig. 1).

Les statistiques de déferlement de vagues sont estimées à partir du traitement des images obtenues avec une caméra de haute résolution (12 MP) installée au dessus du bassin, avec un champs de vue d'environ 10 m par 8 m. Les conditions de vagues (H_s, T) dans le bassin sont mesurées avec une vingtaine de sondes résistives. Une balance d'effort, installée à intérieur de la structure, mesure les efforts de vagues à haute fréquence (1000Hz) afin d'observer la variabilité en fonction de la phase de la vague, et notamment pour capturer les effets du "slamming". En parallèle, une deuxième caméra avec une haute fréquence d'acquisition, enregistre une vue de la surface libre à la crête de la dune (e.g. Fig. 1), incluant le monopile dans le cas des essais avec la structure afin de caractériser le type de déferlement.

L'objectif final est de proposer un système de modélisation utilisable pour des applications réelles. Nous allons présenter à la conférence les résultats préliminaires des analyses des essais en laboratoire, et en parallèle, les résultats des simulations numériques.

Les auteurs tiennent à remercier l'équipe du POMPHY au LNHE d'EDF R&D et aux financeurs (Energy4Climate, EDF Renouvelables).

Références

[1] M. Alagan Chella, A. Tørum, and D. Myrhaug. An overview of wave impact forces on offshore wind turbine substructures. *Energy Procedia*, 20 :217–226, 2012.

[2] S. T. Grilli, J. Skourup, and I. Svendsen. An efficient boundary element method for nonlinear water waves. *Engng. Analysis with Boundary Elemts.*, 6(2) :97–107, 1989.

[3] S. Mohanlal, J. Harris, M. Yates, and S. Grilli. Unified depth-limited wave breaking detection and dissipation in fully nonlinear potential flow models. *Coastal Engineering*, Submitted, 2022.

Appendix C

37^{th} International Conference on Coastal Engineering (ICCE, Sydney, Australia, December 4-9, 2022)

SIMULATION OF STEEPNESS-LIMITED BREAKING WAVES IN A FULLY NONLINEAR POTENTIAL FLOW MODEL

Sunil Mohanlal, LHSV, Ecole des Ponts, EDF R&D, Chatou, France, sunil.mohanlal@enpc.fr
Lili Kimmoun, Centrale Marseille, IRPHE, France, lili.kimmoun@centrale-marseille.fr
Stephan Grilli, Department of Ocean Engineering, University of Rhode Island, Narragansett, RI, USA, grilli@uri.edu
Jeffrey Harris, LHSV, Ecole des Ponts, EDF R&D, Chatou, France, jeffrey.harris@enpc.fr

INTRODUCTION

Steepness-limited wave breaking is simulated in a fully nonlinear potential flow model and validated with laboratory data. Breaking onset is based on the ratio of horizontal particle velocity at the crest, relative to the crest velocity reaching a threshold value. A breaking dissipation model, where the non-dimensional breaking strength parameter is predicted based on the linear wave steepness is used. A new time-dependent dissipation is tested, and the breaking termination criterion is studied.

NUMERICAL MODEL

Fully non-linear potential flow model (FNPF) assumes the fluid flow to be irrotational and inviscid, therefore the Laplacian of the velocity potential equal to zero. These models are computationally more efficient than the Navier-stokes models, but dissipation processes have to be explicitly modelled - for example, in situations when breaking waves are present. The FNPF model used here solves this Laplacian equation based on a boundary integral equation derived from Green's second identity, and time-integration of the free surface kinematic and dynamic boundary condition with a 2^{nd} order Taylor series expansion (Grilli et al., 1989).

EXPERIMENTAL SETUP

The test facility is a wave flume at a constant depth of $h = 0.667\ m$, where a flap wavemaker hinged $0.4\ m$ below the actual bottom is located at $x = 0$, and a wall at $x = 12.535\ m$ (Fig. 1). Focused waves are generated by the wavemaker based on a Ricker spectrum given by,

$$s(\omega) = H\sqrt{T}e^{-\omega^m T}[1 - a(\omega^m T - 1)] \qquad (1)$$

with $a = 1/(\omega_p^m T - 2)$, where ω_p is the peak angular frequency, H is a design wave height, m and T are spectral design parameters. The corresponding first-order transfer function is used to obtain the wavemaker kinematics (angular displacement, velocity and acceleration) in time. These kinematics are used as boundary conditions in the NWT (Grilli et al., 1997).

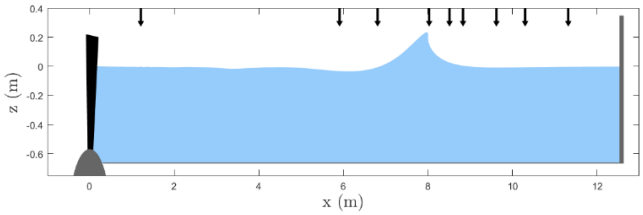

Figure 1: Experimental setup showing the flap wavemaker on the left and a wall on the right and a typical free surface elevation at the breaking onset. The arrows on the top indicates the location of gauges (Note: axis not equal).

BREAKING DISSIPATION

Implementing wave breaking in a fully nonlinear potential flow model is carried out in three steps. First, an onset, the instant at which wave breaking starts, is identified. We use the recently proposed universal criterion, i.e., an evolving crest whose ratio of horizontal particle velocity at the crest u, relative to the crest velocity c, $B = u/c$ exceeds 0.85, has not yet, but will break (Barthelemy et al., 2018). Derakhti et al. (2020) showed that this criterion applies well to arbitrary wavetrains in all ranges of water depth, including shallow water. Second, the magnitude of the energy dissipated is determined. This is done in two steps, the non-dimensional breaking strength parameter b (defined such that wave energy dissipation rate per unit length of the breaking crest, $\varepsilon = b\rho g^{-1}c^5$) is determined, which is used to obtain an instantaneous power to be dissipated. This power is then modelled by applying a damping pressure across the breaking wave free surface (Grilli et al., 2020; Papoutsellis et al. 2019). Lastly, a breaking termination criterion is specified to cease this dissipation.

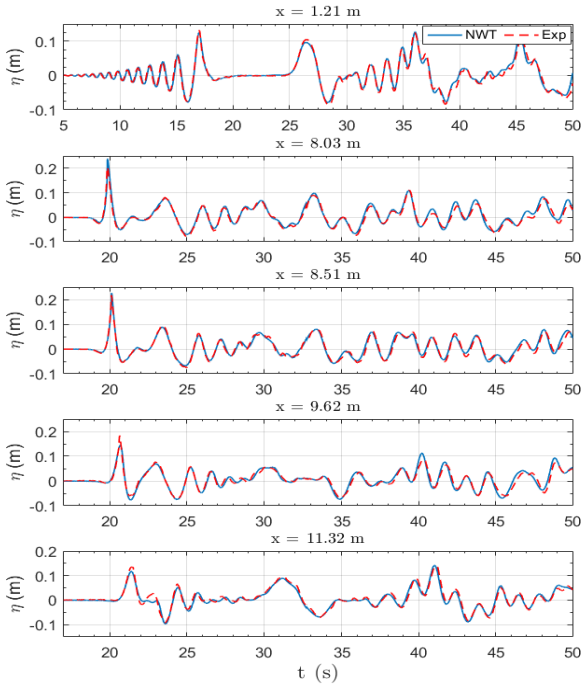

Figure 2: Free surface time series measurements at 5 gauges (dashed: experiment and solid: NWT) for a test case with $T_p = 2.4\ s$, $H = 0.2593\ m$, $T = 0.2285$ and $m = 1.42$. Onset is identified at $x = 8.05\ m$ and $t = 19.83\ s$.

B_{off}	$\bar{\bar{\eta}}(cm^2)$
Measured	110.1
0.1	83.3
0.2	97.7
0.3	106.1
0.4	109.7
0.5	112.9

Table 1: Sensitivity of B_{off} to the breaking dissipation. $\bar{\bar{\eta}} = \int_t^{t+T_p} \eta^2 dt$ where η is the elevation at $x = 9.62\ m$. T_p is the peak period and t is the instant the breaking wave crest reaches this gauge.

RESULTS

In the test cases under study, focused waves are generated that break in the domain and are reflected back from the wall. Free surface time series are measured at 9 gauges for a series of test cases with different wave steepness and focusing distances (x_f). Several videos and snapshots of the breaking waves are captured. Fig. 2 shows free surface measurements at 5 gauges of a test case with $x_f = 7.8\ m$. This test case corresponds to a linear wave steepness, $S = \sum_i a_i k_i = 0.45$, where a^i is the wave amplitude and k^i, the wave number of the i^{th} component, with $T_p = 2.4\ s$, $H = 0.2593\ m$, $T = 0.2285$ and $m = 1.42$. At the breaking onset has $d/L_b = 0.1618$ and $H_b/L_b = 0.0656$, thus characterising the breaker as an intermediate one, where d is the water depth, L_b is the wavelength measured as twice the distance between two zero-crossing points and H_b is the crest to trough height.

Testing different values of the dissipation strength, we see that the empirical prediction of Romero et al. (2012) for breaking strength based on linear wave steepness is reasonable, with $b \approx 0.033$, and is used to model the resulting breaking wave dissipation. The instantaneous power is then dissipated as in Mohanlal et al. (in revisions).

The breaking termination criterion, $B_{off} = 0.4$ is used, after testing a variety of values (see Table 1). Results show a very close agreement achieved between numerical simulations (NWT) and measurements, including close to the onset (Fig. 3) (at $x = 8.03\ m$) and beyond breaking (at $x = 11.32\ m$).

CONCLUSION

From the results, we see that the NWT is able to simulate non-linear waves accurately until the onset. Then, with the onset criterion $B = 0.85$, that determines a wave that is about to break, is seen to be an instant when the free surface is close to being vertical. The dissipation strength for steepness-limited breaking waves, predicted by their linear wave steepness (Romero et al. 2012), then models the resulting breaking wave to reasonable accuracy. This prediction however is determined by a narrow spread of data. Therefore, a quantitative study will be shown at the conference, showing the sensitivity in simulation results on b. A similar study will be done on the sensitivity of the breaking termination criterion.

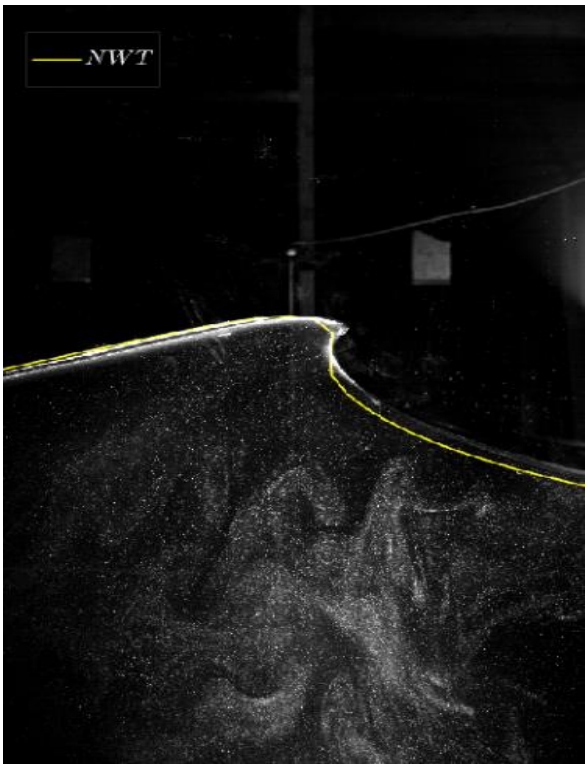

Figure 3: Free surface elevation at the onset, of NWT results for the case of Fig. 2 (yellow) compared with the experimental figure at an overturning instant.

REFERENCES

Barthelemy, X., Banner, M.L., Peirson, W.L., Fedele, F., Allis, M., Dias, F., 2018. On a unified breaking onset threshold for gravity waves in deep and intermediate depth water. Journal of Fluid Mechanics 841, 463–488.

Derakhti M. , J.T. Kirby, M.L. Banner, S.T. Grilli and J. Thomson 2020. A unified breaking onset criterion for surface gravity water waves in arbitrary depth. J. Geophys. Res., 125(7), e2019JC015886.

Grilli, S.T., Horrillo, J., 1997. Numerical generation and absorption of fully nonlinear periodic waves. Journal of engineering mechanics 123, 1060–1069

Grilli, S.T., Horrillo, J., Guignard, S., 2020. Fully nonlinear potential flow simulations of wave shoaling over slopes: Spilling breaker model and integral wave properties. Water Waves 2, 263–297.

Grilli, S.T., Skourup, J., Svendsen, I., 1989. An efficient boundary element method for nonlinear water waves. Engineering Analysis with Boundary Elements 6, 97–107.

Mohanlal, S., Harris, J., Yates, M., Grilli, S., In Revisions. Unified depth-limited wave breaking detection and dissipation in fully nonlinear potential flow models. Coastal Engineering.

Papoutsellis, C.E., Yates, M.L., Simon, B., Benoit, M., 2019. Modelling of depth-induced wave breaking in a fully nonlinear free surface potential flow model. Coastal Engineering 154, 103579.

Romero, L., Melville, W.K., Kleiss, J.M., 2012. Spectral energy dissipation due to surface wave breaking. Journal of Physical Oceanography 42, 1421–1444.

Appendix D

26^{th} Rencontre du Non-Linéaire (RNL, University of Paris Cité, France, March 28-30, 2023)

Breaking waves in a fully non-linear potential flow model

Sunil Mohanlal[1], Jeffrey C. Harris[1], Marissa L. Yates[1], Luc Pastur[2], Christophe Peyrard[1,3], Stephan T. Grilli[4]

[1] LHSV, Ecole des Ponts, EDF R&D, Chatou, France
[2] IMSIA, ENSTA Paris
[3] EDF R&D LNHE
[4] Department of Ocean Engineering, University of Rhode Island, Narragansett, RI, USA
sunil.mohanlal@enpc.fr

Once generated by wind, ocean waves evolve, with complex kinematics and dynamics, as a result of nonlinear and dispersive effects, the effects of bathymetry, and dissipation from wave breaking and bottom friction, to name a few. Accurate simulations of this evolution are crucial for predicting phase-resolved surface wave properties in complex sea states, which govern wave interactions with fixed and floating objects, including offshore renewable energy systems, and surf zone parameters that drive nearshore currents and sediment processes, whose understanding and prediction are key to coastal management decisions.

Due to the computational complexity of modeling these phenomena over large domains in Navier–Stokes models, researchers rely on using simpler models and explicitly introduce the desired effects, e.g., the addition of a dissipative term in the Euler equations. Our work is concentrated on using the existing knowledge of breaking waves to mimic its effects in simpler models such as potential flow.

Extensive research has been done on understanding the many aspects of wave breaking (e.g., Duncan [1], Stive [2], Banner and Peregrine [3], Barthelemy et al. [4], Derakhti et al. [5]). This knowledge is used extensively to model breaking waves in 2D, in specific conditions (e.g, Simon et al. [7], Papoutsellis et al. [6], Grilli et al. [8]). We propose a unified method for modeling 2D depth-limited breaking waves, which is also being currently extended to 3D waves.

Références

1. James H. Duncan, *J. Fluid Mech.*, **126**, 507–520, (1983).
2. M.J.F. Stive, *Coastal Engng.*, **8**, 99–127, (1984).
3. M L Banner, D H Peregrine, *Annual Review of Fluid Mech.*, **25**, 373–397, (1993).
4. Barthelemy, X, Banner, ML, Peirson, WL, Fedele, F, Allis, M, Dias, F, *J. Fluid Mech.*, **841**, 463–488, (2018).
5. Morteza Derakhti, Michael L. Banner, James T. Kirby, *J. Fluid Mech.*, **848**, (2018).
6. Christos E. Papoutsellis, Marissa L. Yates, Bruno Simon, Michel Benoit, *Elsevier*, **154**, (2019).
7. Bruno Simon, Christos E. Papoutsellis, Michel Benoit, Marissa L. Yates, *Springer Science and Business Media*, **5**, 365–383, (2019).
8. Grilli, Stephan T, Horrillo, Juan, Guignard, Stephan, *Water Waves*, **2**, 263–297, (2020).

Appendix E

38^{th} International Workshop on Water Waves and Floating Bodies (IWWWFB, University of Michigan, USA, May 7-10, 2023)

3D depth-limited breaking waves in fully non-linear potential flow

Sunil Mohanlal[1], **Jeffrey C. Harris**[1], **Marissa L. Yates**[1], **Stephan T. Grilli**[2]
(1) LHSV, Ecole des Ponts, EDF R&D, Chatou, France
(2) Department of Ocean Engineering, University of Rhode Island, Narragansett, RI, USA
sunil.mohanlal@enpc.fr

HIGHLIGHTS

A new method of modeling 3D depth-limited breaking waves is proposed and implemented in a fully non-linear potential flow model based on the boundary element method. The method is implemented in three steps: (1) identification of breaking onset using the kinematic B criterion; (2) application of damping pressure in the dynamic free surface condition, function of crest kinematics; and (3) a breaking termination criterion to stop this dissipation. A validation case for a numerical experiment set-up is presented.

1 INTRODUCTION

The study of breaking waves is crucial to establish engineering wave properties in complex sea states, which govern, among other things, wave interaction with fixed and floating structures. Extensive research has being done on understanding the many aspects of this phenomenon (e.g., Duncan [1], Stive [2], Banner and Peregrine [3], Barthelemy et al. [4], Derakhti et al. [5], Derakhti et al. [6]). Due to the computational complexity of modeling breaking waves over large domains in Navier–Stokes models, researchers still rely on using simpler models in which the effects of breaking waves are explicitly introduced. This was done in 2D with a variety of advanced models and methods, e.g., by Guignard and Grilli [7], Kennedy et al. [8], Simon et al. [9], Papoutsellis et al. [10], and Mohanlal et al. [11]. In 3D, however, numerical techniques have mostly been simpler and limited to preventing numerical instabilities in the model when wave breaking occurs (e.g., Pierella et al. [12], Ghadirian et al. [13]). Here, we propose a new method for modeling 3D depth-limited breaking waves, which is an extension of our earlier work in 2D (Mohanlal et al. [11]).

2 FULLY NON LINEAR POTENTIAL FLOW (FNPF) MODEL

The considered FNPF model assumes the fluid flow to be inviscid and irrotational such that the flow velocity can be written as $\mathbf{V} = \nabla\phi$, where ϕ is a velocity potential, such that $\nabla^2\phi = 0$. We use the model of Harris et al. [14], in which, as in Grilli et al. [15], Laplace's equation is solved as a boundary integral equation, discretized with a higher-order BEM,

$$\alpha(\mathbf{x}_i)\phi(\mathbf{x}_i) = \int_\Gamma \left\{ \frac{\partial\phi}{\partial n}(\mathbf{x})G(\mathbf{x}-\mathbf{x}_i) - \phi(\mathbf{x})\frac{\partial G}{\partial n}(\mathbf{x}-\mathbf{x}_i) \right\} \mathrm{d}\Gamma, \tag{1}$$

where Γ is the boundary, α is the interior solid angle at the boundary at point $\mathbf{x}_i$, and $G(\mathbf{x},\mathbf{x}_i) = 1/(4\pi r_i)$ is the 3D free space Green's function (with $r_i = |\mathbf{x}-\mathbf{x}_i|$).

3 WAVE BREAKING MODEL

To demonstrate the breaking model, a simple 3D submerged bar (Fig. 1a) is considered,

with an incident solitary wave of relative height $H/h = 0.7$ (as in Antuono et al. [16]). Wave breaking is modeled in three steps: (1) wave crests reaching breaking onset are identified with the universal criterion that an evolving crest, whose ratio of horizontal particle velocity at the crest, u, to crest velocity, c, exceeds a critical value, $B = u/c = 0.85$, will always break; and otherwise it will not (e.g., Derakhti et al. [6]); (2) an absorbing pressure is applied to breaking crest regions [7, 17]; (3) absorption is terminated when $B_{off} = 0.3$, as in Mohanlal et al. [11], who found this to be optimal for 2D wave breaking on submerged bars, based on a few test cases.

To detect breaking crests in a general way, local maxima are first found (Fig. 1a,b), then, the surrounding 16 BEM nodes are fitted with a bi-cubic fit (see Fig. 1b; Grilli et al. [15]) in which a wave crest line segment is calculated (Fig. 1c), defined by a length (δ), mean position ($\overline{x_c}$, $\overline{y_c}$), and horizontal flow velocity at the surface, $u = \sqrt{u_x^2 + u_y^2}$ at this mean position, slope, and intercept. These crest segments are tracked in time by assuming that, for a small time step, they move approximately in the local normal direction. Phase speed along each crest segment is finally calculated as $c = \sqrt{(d\overline{x_c}/dt)^2 + (d\overline{y_c}/dt))^2}$, which yields $B = u/c$. Fig. 2 shows positions and B values of detected crests, up to breaking onset.

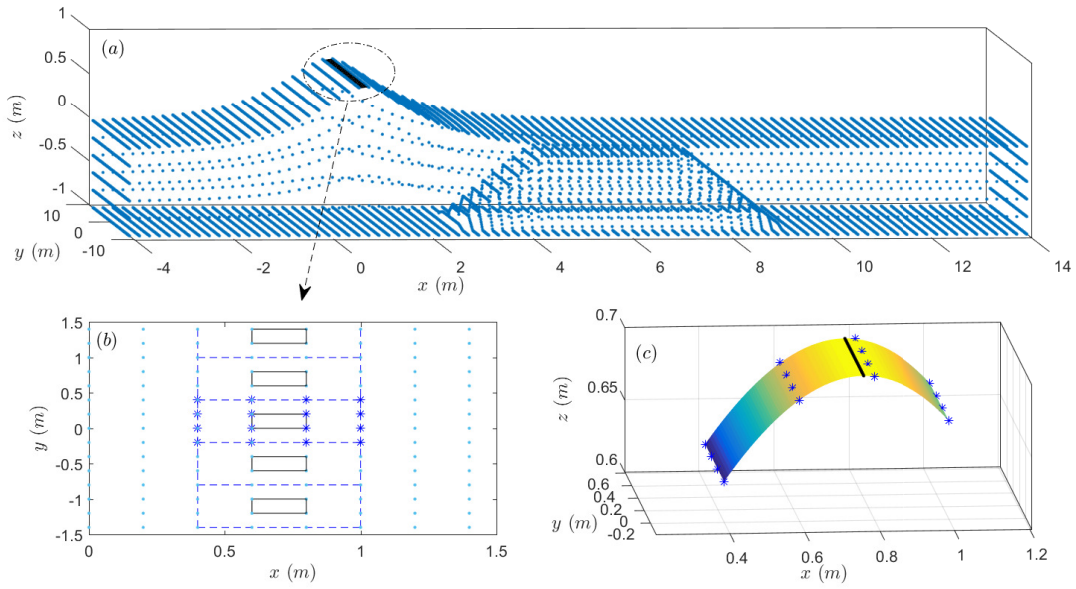

Figure 1: (a) Solitary wave propagating over 3D submerged bar ($h = 1\ m$; depth near the wavemaker); dots indicate BEM nodes. (b) Close-up top view of the free surface nodes around the crest, with solid rectangles indicating the selected elements for further analysis. Nodes selected around an element for crest detection are marked as stars. (c) Bi-cubic fit on 16 nodes around selected element, with detected crest shown as black line.

The energy dissipation in breaking crests is then determined as: (1) the non-dimensional breaking strength parameter b (defined such that wave energy dissipation rate per unit length of the breaking crest, $\epsilon = b\rho g^{-1}c^5$) is determined following Mohanlal et al. [11]; and (2) $b = 0.05$ is used to calculate the instantaneous power dissipated per unit length of crest Π_b, modeled as the work over one time step of a damping pressure P_b specified in the dynamic

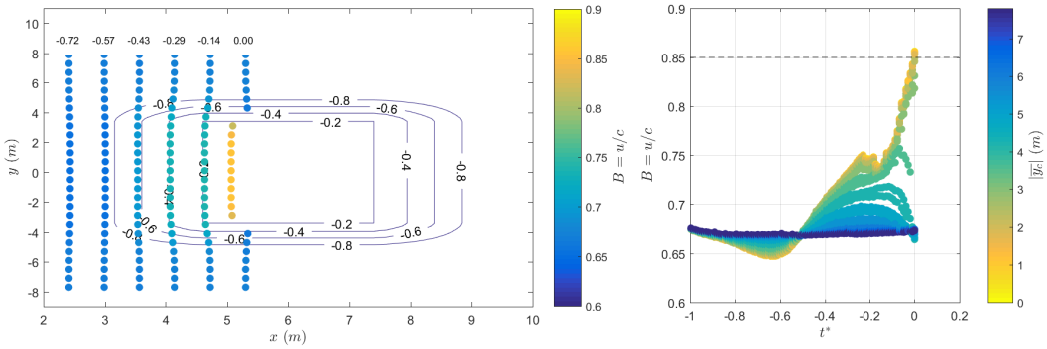

Figure 2: Left: Solitary wave crests ($\overline{x_c}$, $\overline{y_c}$) at six times $t^* = (t - t_b)/\sqrt{gh}$, with breaking onset at t_b; color scale is $B = u/c$; bottom contours shown as black lines (in meter). Right: B *vs* t^* for all crests, up to breaking onset ($B = 0.85$); color scale is $|\overline{y_c}|$ (m).

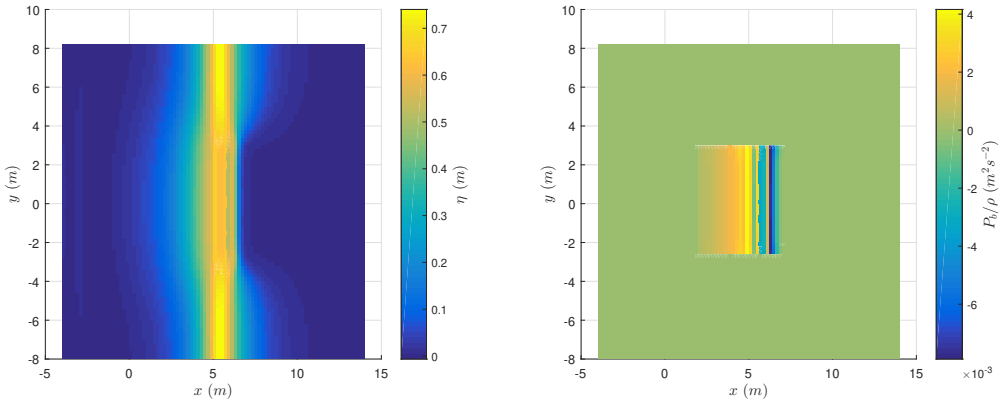

Figure 3: Left: a plot of the free surface at the breaking onset time t_b. Right: the damping pressure (P_b/ρ) applied on a section of the free surface. Note: for stability in more general cases, this should be smoothed between breaking and non breaking regions, not shown here.

free surface condition around the breaking wave crests (Grilli et al. [17]), with $P_b(x, y, t) = \nu(t)\phi_n(x, y, t)$, where the absorbing function is $\nu(t) = \Pi_b\delta/(\int_x \int_y \phi_n^2 \sqrt{1 + \eta_x^2 + \eta_y^2} dxdy)$, ϕ_n is the normal surface velocity. Fig. 3 shows computed surface and pressure at breaking onset time t_b.

4 SUMMARY

A method of modeling depth-limited breaking waves in a 3D FNPF-BEM model is demonstrated. The approach is easily extendable to other evolving wave crests, for regular waves or more realistic sea-states, as was done in earlier 2D work [11]. Numerical developments are in preparation for comparisons with existing experimental data from the literature, e.g., the free surface elevation post-breaking, and identification of wave breaking regions.

ACKNOWLEDGEMENTS

This research was produced within the framework of Energy4Climate Interdisciplinary Center (E4C) of IP Paris and Ecole des Ponts ParisTech. This research was supported by 3rd

Programme d'Investissements d'Avenir [ANR-18-EUR-0006-02]. This action benefited from the support of the Chair «Challenging Technology for Responsible Energy» led by l'X – Ecole Polytechnique and the Fondation de l'Ecole Polytechnique, sponsored by Total Energies. SG is gratefully acknowledging support from the US National Science Foundation grant #OCE-19-47960. The authors also thank Luc Pastur (ENSTA Paris) and Christophe Peyrard (EDF R&D LNHE) for helpful discussions.

REFERENCES

[1] Duncan, J. H. 1983. *The breaking and non-breaking wave resistance of a two-dimensional hydrofoil. J. Fluid Mech. 126*, 507–520.

[2] Stive, M. 1984. *Energy dissipation in waves breaking on gentle slopes.* Coastal Engng. 8(2), 99–127.

[3] Banner, M. L., and Peregrine, D. H. jan 1993. *Wave Breaking in Deep Water.* Annual Review of Fluid Mech. 25(1), 373–397.

[4] Barthelemy, X., Banner, M., Peirson, W., Fedele, F., Allis, M., and Dias, F. 2018. *On a unified breaking onset threshold for gravity waves in deep and intermediate depth water. J. Fluid Mech. 841*, 463–488.

[5] Derakhti, M., Banner, M. L., and Kirby, J. T. jun 2018. *Predicting the breaking strength of gravity water waves in deep and intermediate depth. J. Fluid Mech. 848*.

[6] Derakhti, M., Kirby, J. T., Banner, M. L., Grilli, S. T., and Thomson, J. 2020. *A Unified Breaking Onset Criterion for Surface Gravity Water Waves in Arbitrary Depth.* J. Geophys. Res.: Oceans 125(7).

[7] Guignard, S., and Grilli, S. T. Modeling of wave shoaling in a 2D-NWT using a spilling breaker model. In *The Eleventh International Offshore and Polar Engineering Conference* (2001), OnePetro.

[8] Kennedy, A. B., Chen, Q., Kirby, J. T., and Dalrymple, R. A. 2000. *Boussinesq modeling of wave transformation, breaking, and runup. I: 1D.* J. Waterway, Port, Coastal, and Ocean Engng. 126(1), 39–47.

[9] Simon, B., Papoutsellis, C. E., Benoit, M., and Yates, M. L. 2019. *Comparing methods of modeling depth-induced breaking of irregular waves with a fully nonlinear potential flow approach.* J. Ocean Engineering and Marine Energy 5(4), 365–383.

[10] Papoutsellis, C. E., Yates, M. L., Simon, B., and Benoit, M. 2019. *Modelling of depth-induced wave breaking in a fully nonlinear free-surface potential flow model. Coastal Engng. 154*, 103579.

[11] Mohanlal, S., Harris, J., Yates, M., and Grilli, S. 2022. *Unified depth-limited wave breaking detection and dissipation in fully nonlinear potential flow models. Coastal Engng. Submitted*.

[12] Pierella, F., Lindberg, O., Bredmose, H., Bingham, H. B., Read, R. W., and Engsig-Karup, A. P. 2021. *The DeRisk database: Extreme design waves for offshore wind turbines. Marine Structures 80*, 103046.

[13] Ghadirian, A., Pierella, F., and Bredmose, H. 2023. *Calculation of slamming wave loads on monopiles using fully nonlinear kinematics and a pressure impulse model. Coastal Engng. 179*, 104219.

[14] Harris, J. C., Dombre, E., Benoit, M., Grilli, S. T., and Kuznetsov, K. I. 2022. *Nonlinear time-domain wave-structure interaction: a parallel fast integral equation approach.* Intl. J. Numer. Meth. Fluids 94(2), 188–222.

[15] Grilli, S. T., Guyenne, P., and Dias, F. 2001. *A fully non-linear model for three-dimensional overturning waves over an arbitrary bottom.* Intl. J. Numer. Meth. Fluids 35(7), 829–867.

[16] Antuono, M., Lucarelli, A., Bardazzi, A., and Brocchini, M. 2022. *A wave-breaking model for the depth-semi-averaged equations. J. Fluid Mech. 948*, A50.

[17] Grilli, S. T., Horrillo, J., and Guignard, S. 2020. *Fully nonlinear potential flow simulations of wave shoaling over slopes: Spilling breaker model and integral wave properties.* Water Waves 2(2), 263–297.

Appendix F

5^{th} B'WAVES (INRIA, Bordeaux, FRANCE, May 30-June 1, 2023)

Simulation of 3D depth-limited breaking waves on a submerged bar in a fully non-linear potential flow model.

Sunil Mohanlal[1], Jeffrey C. Harris[1], Marissa L. Yates[1], Luc Pastur[2], Christophe Peyrard[1,3], Stephan T Grilli[4]

[1] LHSV, Ecole des Ponts, EDF R&D, Chatou, France
[2] UME, ENSTA Paris, Palaiseau, France
[3] EDF R&D LNHE, Chatou, France
[4] Department of Ocean Engineering, University of Rhode Island, Narragansett, RI, USA

Simulating breaking waves in Navier-Stokes models is computationally intensive, motivating researchers in the past and present, to develop efficient numerical methods. Generally, these methods are calibrated for specific cases since they are based on assumptions that do not consider the complete physics of breaking waves. We have developed a method of modelling 3D depth-limited breaking waves, based on our recent work proposing a unified 2D depth-limited wave breaking model (Mohanlal et al.) in the boundary element method, fully non-linear potential model of Grilli et al. 2001; Harris et al. 2022. The proposed wave breaking model consists of (1) a universal breaking onset criterion from Barthelemy et al. 2018 and Derakhti et al. 2020, i.e., an evolving crest, whose ratio of horizontal particle velocity at the crest, u, to crest velocity, c, exceeding a critical value, $B = u/c = 0.85$, will always break; (2) the energy dissipation in breaking crests that is determined by a non-dimensional breaking strength parameter b (defined such that wave energy dissipation rate per unit length of the breaking crest, $\varepsilon = b\rho g^{-1}c^5$) following Mohanlal et al., which is then modeled as an absorbing pressure on the free surface; (3) a termination criterion based on B to stop this dissipation. At the workshop, we will present the most recent results, including validation of the wave breaking model in comparison to the laboratory measurements of regular wave propagation over 3D submerged bar of Kamath et al. 2022.

References

1. Mohanlal, S., Harris, J., Yates, M., and Grilli, S. 2022. Unified depth-limited wave breaking detection and dissipation in fully nonlinear potential flow models. Coastal Engng. *Submitted*.
2. Grilli, S. T., Guyenne, P., and Dias, F. 2001. A fully non-linear model for three-dimensional overturning waves over an arbitrary bottom. Intl. J. Numer. Meth. Fluids 35(7), 829–867.
3. Jeffrey Harris, Emmanuel Dombre, Michel Benoit, Stephan T. Grilli, Konstantin Kuznetsov. Nonlinear time-domain wave-structure interaction: a parallel fast integral equation approach. International Journal for Numerical Methods in Fluids, Wiley, 2022.
4. Barthelemy, X., Banner, M., Peirson, W., Fedele, F., Allis, M., and Dias, F. 2018. On a unified breaking onset threshold for gravity waves in deep and intermediate depth water. J. Fluid Mech. 841, 463–488.
5. Derakhti, M., Kirby, J. T., Banner, M. L., Grilli, S. T., and Thomson, J. 2020. A Unified Breaking Onset Criterion for Surface Gravity Water Waves in Arbitrary Depth. J. Geophys. Res.: Oceans 125(7).
6. Kamath, A., Roy, T., Seiffert, B.R. and Bihs, H., 2022. Experimental and numerical study of waves breaking over a submerged three-dimensional bar. Journal of Waterway, Port, Coastal, and Ocean Engng, 148(2), p.04021052.

Appendix G

Input conditions of all the focused breaking tests conducted by Lili Kimmoun in ECM

Test	$d\ (cm)$	$H\ (m)$	$x_f\ (m)$	Remarks	dx (cm/px)	SL (px)
8	66.7	0.2377	8	no camera	0.03188	-
9	66.7	0.2377	7.8	camera, lens $28\ mm$	0.03188	920
10	66.7	0.2377	7.6	-	0.03188	920
11	66.7	0.2377	7.3	-	0.03188	920
12	66.7	0.2485	7.4	-	0.03188	920
13	66.7	0.2485	7.2	-	0.03188	920
14	66.7	0.2485	7.2	camera centered vertically on the crest	0.03188	1915
15	66.7	0.2485	7.2	the laser sheet is moved left	0.03021	1915
16	66.7	0.2485	7.5	-	0.03021	1915
17	66.7	0.2593	7.5	-	0.03021	1915
18	66.7	0.2593	7.2	-	0.03021	1915
19	66.7	0.2593	7.8	-	0.03021	1915
20	66.7	0.2593	7.5	same position of the camera, lens $50\ mm$	0.016445	2480
21	66.7	0.2593	7.2	over-exposed	0.016445	2480
22	66.7	0.2593	7.2	diaphragm is adjusted	0.016445	2480
23	66.7	0.2593	7.8	-	0.016445	2480

Table G.1: Test 2021: $T = 0.2285$, $m = 1.42$, $T_p = 2.4\ s$

Bibliography

Abadie, S., Morichon, D., Grilli, S. & Glockner, S. (2010), 'Numerical simulation of waves generated by landslides using a multiple-fluid Navier–Stokes model', *Coastal Engineering* **57**(9), 779–794.

Adytia, D., Husrin, S. & Adiwijaya (2018), Numerical simulation of breaking regular and irregular wave propagation above a sloping bottom, *in* 'Journal of Physics: Conference Series', Vol. 1090, IOP Publishing, p. 012065.

Agnon, Y., Madsen, P. A. & Schäffer, H. A. (1999), 'A new approach to high-order Boussinesq models', *Journal of Fluid Mechanics* **399**, 319–333.

Banari, A., Janßen, C. F. & Grilli, S. T. (2014), 'An efficient lattice Boltzmann multiphase model for 3D flows with large density ratios at high Reynolds numbers', *Computers & Mathematics with Applications* **68**(12), 1819–1843.

Banner, M. L. & Peirson, W. L. (2007), 'Wave breaking onset and strength for two-dimensional deep-water wave groups', *Journal of Fluid Mechanics* **585**, 93–115.

Banner, M. L. & Peregrine, D. H. (1993), 'Wave breaking in deep water', *Annual Review of Fluid Mechanics* **25**(1), 373–397.

Barthelemy, X., Banner, M. L., Peirson, W. L., Fedele, F., Allis, M. & Dias, F. (2018), 'On a unified breaking onset threshold for gravity waves in deep and intermediate depth water', *Journal of Fluid Mechanics* **841**, 463–488.

Basco, D. R. & Svendsen, I. A. (1984), Modeling turbulent bore propagation in the surf zone, *in* 'Coastal Engineering 1984', pp. 99–114.

Battjes, J. A. (1974), Surf similarity, *in* 'Coastal Engineering Proceedings', pp. 466–480.

Beji, S. & Battjes, J. A. (1993), 'Experimental investigation of wave propagation over a bar', *Coastal Engineering* **19**(1-2), 151–162.

Belibassakis, K. & Athanassoulis, G. (2011), 'A coupled-mode system with application to nonlinear water waves propagating in finite water depth and in variable bathymetry regions', *Coastal Engineering* **58**(4), 337–350.

Benoit, M., Coulaud, G., Capillon, S., Teles, M., Benguigui, W. & Robaux, F. (2023), Numerical modeling of depth-induced wave breaking: a review and comparison of low-to high-fidelity simulation methods., *in* 'B'WAVES. May 30 - June 1, Bordeaux'.

Benoit, M., Luck, M., Chevalier, C. & Belorgey, M. (2002), Near-bottom kinematics of shoaling and breaking waves: Experimental investigation and numerical prediction, *in* 'Proceedings of 28th International Conference on Coastal Engineering', pp. 306–318.

Benoit, M., Marcos, F. & Becq, F. (1997), Development of a third generation shallow-water wave model with unstructured spatial meshing, *in* 'Coastal Engineering 1996', pp. 465–478.

Benoit, M., Yates, M. & Chazel, F. (2013), A comparison of simulation approaches based on the zakharov equations for nonlinear waves in the coastal zone, *in* 'Proceedings of the 28th International Workshop on Water Waves and Floating Bodies, L'Isle-sur-la-Sorgue, France'.

Bingham, H. B. & Zhang, H. (2007), 'On the accuracy of finite-difference solutions for nonlinear water waves', *Journal of Engineering Mathematics* **58**, 211–228.

Blenkinsopp, C. & Chaplin, J. (2007), 'Void fraction measurements in breaking waves', *Proceedings of the Royal Society A: Mathematical, Physical and Engineering Sciences* **463**(2088), 3151–3170.

Boettger, D. G., Keating, S. R., Banner, M. L., Morison, R. P. & Barthélémy, X. (2023), 'An energetic signature for breaking inception in surface gravity waves', *Journal of Fluid Mechanics* **959**, A33.

Bonneton, P., Barthélemy, E., Chazel, F., Cienfuegos, R., Lannes, D., Marche, F. & Tissier, M. (2011), 'Recent advances in Serre-Green Naghdi modelling for wave transformation, breaking and runup processes', *European Journal of Mechanics-B/Fluids* **30**(6), 589–597.

Bonneton, P., Chazel, F., Lannes, D., Marche, F. & Tissier, M. (2011), 'A splitting approach for the fully nonlinear and weakly dispersive Green–Naghdi model', *Journal of Computational Physics* **230**(4), 1479–1498.

Boussinesq, J. (1872), 'Théorie des ondes et des remous qui se propagent le long d'un canal rectangulaire horizontal, en communiquant au liquide contenu dans ce canal des vitesses sensiblement pareilles de la surface au fond', *Journal de Mathématiques Pures et Appliquées* **17**, 55–108.

Cienfuegos, R., Barthélemy, E. & Bonneton, P. (2006), 'A fourth-order compact finite volume scheme for fully nonlinear and weakly dispersive Boussinesq-type equations. Part I: model development and analysis', *International Journal for Numerical Methods in Fluids* **51**(11), 1217–1253.

Cointe, R. (1987), *A theory of breakers and breaking waves*, University of California, Santa Barbara.

Craig, W. & Sulem, C. (1993), 'Numerical simulation of gravity waves', *Journal of Computational Physics* **108**(1), 73–83.

Dalrymple, R. A. & Rogers, B. (2006), 'Numerical modeling of water waves with the SPH method', *Coastal Engineering* **53**(2-3), 141–147.

De Vita, F., Verzicco, R. & Iafrati, A. (2018), 'Breaking of modulated wave groups: kinematics and energy dissipation processes', *Journal of fluid mechanics* **855**, 267–298.

Dean, R. G. (1965), 'Stream function representation of nonlinear ocean waves', *Journal of Geophysical Research* **70**(18), 4561–4572.

Dean, R. G. & Dalrymple, R. A. (1991), 'Water wave mechanics for engineers and scientists'.

Deardorff, J. W. (1970), 'A numerical study of three-dimensional turbulent channel flow at large reynolds numbers', *Journal of Fluid Mechanics* **41**(2), 453–480.

Deike, L., Melville, W. K. & Popinet, S. (2016), 'Air entrainment and bubble statistics in breaking waves', *Journal of Fluid Mechanics* **801**, 91–129.

Derakhti, M., Banner, M. L. & Kirby, J. T. (2018), 'Predicting the breaking strength of gravity water waves in deep and intermediate depth', *Journal of Fluid Mechanics* **848**.

Derakhti, M., Kirby, J. T., Banner, M. L., Grilli, S. T. & Thomson, J. (2020), 'A unified breaking onset criterion for surface gravity water waves in arbitrary depth', *Journal of Geophysical Research: Oceans* **125**(7).

Derakhti, M., Kirby, J. T., Grilli, S. T. & Thomson, J. (2023), 'From deep to shallow water: a unified scaling and parameterization of wave breaking dissipation', The WISE Zoominar series https://youtu.be/iTyAaExxLSw.

Derakhti, M., Kirby, J. T., Shi, F. & Ma, G. (2016), 'Wave breaking in the surf zone and deep-water in a non-hydrostatic RANS model. part 1: Organized wave motions', *Ocean Modelling* **107**, 125–138.

Derakhti, M., Kirby Jr, J. T., Banner, M. L., Grilli, S. T. & Thomson, J. (2018), A unified formulation for predicting the breaking strength of gravity water waves from deep to shallow water, *in* 'AGU Fall Meeting Abstracts', Vol. 2018, pp. OS31E–1826.

Derakhti, M., Kirby Jr, J. T., Banner, M. L., Thomson, J. & Grilli, S. T. (2022), 'Predicting the rate of energy dissipation in breaking gravity water waves from deep to shallow water', *Journal of Fluid Mechanics* **(in preparation)**.

Dingemans, M. W. (1997), *Water wave propagation over uneven bottoms: Linear wave propagation*, Vol. 13, World Scientific.

Dold, J. & Peregrine, D. (1985), Steep unsteady water waves: an efficient computational scheme, *in* 'Proceedings of the 19th International Coastal Engineering Conference', pp. 955–967.

Dombre, E. (2015), Nonlinear modelling of wave-structure interactions applied to offshore wind turbine platforms, PhD thesis, Université Paris-Est.

Dombre, E., Harris, J., Benoit, M., Violeau, D. & Peyrard, C. (2019), 'A 3D parallel boundary element method on unstructured triangular grids for fully nonlinear wave-body interactions', *Ocean Engineering* **171**, 505–518.

Dommermuth, D. G. & Yue, D. K. (1987), 'A high-order spectral method for the study of nonlinear gravity waves', *Journal of Fluid Mechanics* **184**, 267–288.

Drazen, D. A., Melville, W. K. & Lenain, L. (2008), 'Inertial scaling of dissipation in unsteady breaking waves', *Journal of Fluid Mechanics* **611**, 307–332.

Ducrozet, G., Bonnefoy, F., Le Touzé, D. & Ferrant, P. (2007), '3-D HOS simulations of extreme waves in open seas', *Natural Hazards and Earth System Sciences* **7**(1), 109–122.

Ducrozet, G., Bonnefoy, F., Le Touzé, D. & Ferrant, P. (2012), 'A modified high-order spectral method for wavemaker modeling in a numerical wave tank', *European Journal of Mechanics-B/Fluids* **34**, 19–34.

Ducrozet, G., Bonnefoy, F. & Perignon, Y. (2017), 'Applicability and limitations of highly non-linear potential flow solvers in the context of water waves', *Ocean Engineering* **142**, 233–244.

Ducrozet, G., Wang, Y. & Derakhti, M. (2023), Enhanced wave breaking modelling in a high-order spectral model, *in* 'B'WAVES. May 30 - June 1, Bordeaux'.

Duncan, J. (1981), 'An experimental investigation of breaking waves produced by a towed hydrofoil', *Proceedings of the Royal Society of London. A. Mathematical and Physical Sciences* **377**(1770), 331–348.

Duncan, J. H. (1983), 'The breaking and non-breaking wave resistance of a two-dimensional hydrofoil', *Journal of Fluid Mechanics* **126**, 507–520.

Engsig-Karup, A. P., Bingham, H. B. & Lindberg, O. (2009), 'An efficient flexible-order model for 3D nonlinear water waves', *Journal of Computational Physics* **228**, 2100–2118.

Filipot, J.-F. et al. (2018), Extreme sea states and wave breaking characterization for mre activities, *in* 'JH2018-16èmes Journées de l'Hydrodynamique. 27-29 Novembre 2018, Marseille'.

Fochesato, C. & Dias, F. (2006), 'A fast method for nonlinear three-dimensional free-surface waves', *Proceedings of the Royal Society A: Mathematical, Physical and Engineering Sciences* **462**(2073), 2715–2735.

Fochesato, C., Grilli, S. & Dias, F. (2007), 'Numerical modeling of extreme rogue waves generated by directional energy focusing', *Wave Motion* **44**(5), 395–416.

Grilli, A. R., Westcott, G., Grilli, S. T., Spaulding, M. L., Shi, F. & Kirby, J. T. (2020), 'Assessing coastal hazard from extreme storms with a phase resolving wave model: Case study of Narragansett, RI, USA', *Coastal Engineering* **160**, 103735.

Grilli, S., Gilbert, R. W., Lubin, P., Vincent, S., Astruc, D., Legendre, D., Duval, M., Kimmoun, O., Branger, H., Devrard, D. et al. (2004), Numerical modeling and experiments for solitary wave shoaling and breaking over a sloping beach, *in* 'Proceedings of the 14th International Offshore and Polar Engineering Conference', pp. 306–312.

Grilli, S., Losada, M. & Martin, F. (1992), The breaking of a solitary wave over a step: Modeling and experiments, *in* 'Proceedings of the 4th International Conference on Hydraulic Engineering Software (HYDROSOFT92, Valencia, Spain', pp. 575–586.

Grilli, S., Subramanya, R., Svendsen, I. & Veeramony, J. (1994), 'Shoaling of solitary waves on plane beaches', *Journal of Waterway, Port, Coastal, and Ocean Engineering* **120**(6), 609–628.

Grilli, S. & Svendsen, I. (1990*a*), Computation of nonlinear wave kinematics during propagation and runup on a slope, *in* 'Water wave kinematics', Springer, pp. 387–412.

Grilli, S. & Svendsen, I. (1990*b*), 'Corner problems and global accuracy in the boundary element solution of nonlinear wave flows', *Engineering Analysis with Boundary Elements* **7**(4), 178–195.

Grilli, S. T., Dias, F., Guyenne, P., Fochesato, C. & Enet, F. (2010), 'Progress in fully nonlinear potential flow modeling of 3D extreme ocean waves', *Advances in Numerical Simulation of Nonlinear Water Waves* pp. 75–128.

Grilli, S. T., Guyenne, P. & Dias, F. (2001), 'A fully non-linear model for three-dimensional overturning waves over an arbitrary bottom', *International Journal for Numerical Methods in Fluids* **35**(7), 829–867.

Grilli, S. T. & Horrillo, J. (1997), 'Numerical generation and absorption of fully nonlinear periodic waves', *Journal of Engineering Mechanics* **123**(10), 1060–1069.

Grilli, S. T. & Horrillo, J. (1999), 'Shoaling of periodic waves over barred-beaches in a fully nonlinear numerical wave tank', *International Journal of Offshore and Polar Engineering* **9**(04), 257–263.

Grilli, S. T., Horrillo, J. & Guignard, S. (2020), 'Fully nonlinear potential flow simulations of wave shoaling over slopes: Spilling breaker model and integral wave properties', *Water Waves* **2**(2), 263–297.

Grilli, S. T., Losada, M. A. & Martin, F. (1994), 'Characteristics of solitary wave breaking induced by breakwaters', *Journal of Waterway, Port, Coastal, and Ocean Engineering* **120**(1), 74–92.

Grilli, S. T., Skourup, J. & Svendsen, I. (1989), 'An efficient boundary element method for nonlinear water waves', *Engineering Analysis with Boundary Elements* **6**(2), 97–107.

Grilli, S. T. & Subramanya, R. (1994), 'Quasi-singular integrals in the modeling of nonlinear water waves in shallow water', *Engineering Analysis with Boundary Elements* **13**(2), 181–191.

Grilli, S. T. & Subramanya, R. (1996), 'Numerical modeling of wave breaking induced by fixed or moving boundaries', *Computational Mechanics* **17**(6), 374–391.

Grilli, S. T., Svendsen, I. A. & Subramanya, R. (1997), 'Breaking criterion and characteristics for solitary waves on slopes', *Journal of Waterway, Port, Coastal, and Ocean Engineering* **123**(3), 102–112.

Grilli, S. T., Svendsen, I. A. & Subramanya, R. (1998), 'Closure of: Breaking criterion and characteristics for solitary waves on slopes', *Journal of Waterway, Port, Coastal, and Ocean Engineering* **124**(6), 333–335.

Grilli, S. T., Voropayev, S. I., Testik, F. Y. & Fernando, H. J. S. (2003), Numerical modeling and experiments of wave shoaling over semi-buried cylinders in sandy bottom, *in* 'Proceedings of the 13th International Ocean and Polar Engineering Conference', International Society of Offshore and Polar Engineers, pp. 405–412.

Grue, J. & Jensen, A. (2012), 'Orbital velocity and breaking in steep random gravity waves', *Journal of Geophysical Research: Oceans* **117**(C7).

Guerber, E. (2011), Numerical modelling of nonlinear interactions of waves with submerged structures: applied to the simulation of wave energy converters, PhD thesis, Université Paris-Est.

Guignard, S. & Grilli, S. T. (2001), Modeling of wave shoaling in a 2D-NWT using a spilling breaker model, *in* 'Proceedings of the 11th International Offshore and Polar Engineering Conference', Vol. 3, International Society of Offshore and Polar Engineers, pp. 116–123.

Guignard, S., Marcer, R., Rey, V., Kharif, C. & Fraunié, P. (2001), 'Solitary wave breaking on sloping beaches: 2-D two phase flow numerical simulation by SL-VOF method', *European Journal of Mechanics-B/Fluids* **20**(1), 57–74.

Guthrie, W. F. (2020), *NIST/SEMATECH e-Handbook of Statistical Methods (NIST Handbook 151)*, National Institute of Standards and Technology.

Guyenne, P. & Grilli, S. (2006), 'Numerical study of three-dimensional overturning waves in shallow water', *Journal of Fluid Mechanics* **547**, 361–388.

Hansen, J. & Svendsen, I. (1979), *Regular Waves in Shoaling Water Experimental Data*, Institute of Hydrodynamics and Hydraulic Engineering, Technical University of Denmark.

Harris, J. C., Dombre, E., Benoit, M., Grilli, S. T. & Kuznetsov, K. I. (2022), 'Nonlinear time-domain wave-structure interaction: A parallel fast integral equation approach', *International Journal for Numerical Methods in Fluids* **94**(2), 188–222.

Harris, J., Dombre, E., Mivehchi, A., Benoit, M., Grilli, S. & Peyrard, C. (2016), Avancees de la modelisation non-lineaire des interactions vague-structure, *in* 'JH2018-15èmes Journées de l'Hydrodynamique. 22-24 Novembre 2016, Brest'.

Harris, J. & Grilli, S. (2014), 'Large eddy simulation of sediment transport over rippled beds', *Nonlinear Processes in Geophysics* **21**(6), 1169–1184.

Hasan, S., Sriram, V. & Selvam, R. P. (2019), 'Evaluation of an eddy viscosity type wave breaking model for intermediate water depths', *European Journal of Mechanics-B/Fluids* **78**, 115–138.

Hasselmann, K., Barnett, T. P., Bouws, E., Carlson, H., Cartwright, D. E., Enke, K., Ewing, J., Gienapp, A., Hasselmann, D., Kruseman, P. et al. (1973), 'Measurements of wind-wave growth and swell decay during the joint north sea wave project (JONSWAP).', *Ergaenzungsheft zur Deutschen Hydrographischen Zeitschrift, Reihe A* .

Hayes, M. O. (1985), 'In clark, J.R. (editor) Coastal Resources Management: Development Case Studies. Renewable Resources Information Series, Coastal Management publications, No. 3. Research Planning Institute, Inc, Columbia, South Carolina'.

Higuera, P., Lara, J. L. & Losada, I. J. (2013), 'Realistic wave generation and active wave absorption for Navier-Stokes models: Application to OpenFOAM®', *Coastal Engineering* **71**, 102–118.

Iafrati, A. (2009), 'Numerical study of the effects of the breaking intensity on wave breaking flows', *Journal of Fluid Mechanics* **622**, 371–411.

Iafrati, A. (2011), 'Energy dissipation mechanisms in wave breaking processes: spilling and highly aerated plunging breaking events', *Journal of Geophysical Research: Oceans* **116**(C7).

IEA, Net Zero by 2050 (2021), *IEA, Paris* .
URL: *https://www.iea.org/reports/net-zero-by-2050, License: CC BY 4.0*

IEA, Offshore Wind Outlook (2019), *IEA, Paris* .
URL: *https://www.iea.org/reports/offshore-wind-outlook-2019, License: CC BY 4.0*

IEA, Renewables (2022), *IEA, Paris* .
URL: *https://www.iea.org/reports/renewables-2022, License: CC BY 4.0*

Judge, F. M., Hunt-Raby, A. C., Orszaghova, J., Taylor, P. H. & Borthwick, A. G. (2019), 'Multi-directional focused wave group interactions with a plane beach', *Coastal Engineering* **152**, 103531.

Kamath, A., Roy, T., Seiffert, B. R. & Bihs, H. (2022), 'Experimental and numerical study of waves breaking over a submerged three-dimensional bar', *Journal of Waterway, Port, Coastal, and Ocean Engineering* **148**(2), 04021052.

Kazolea, M. & Ricchiuto, M. (2018), 'On wave breaking for Boussinesq-type models', *Ocean Modelling* **123**, 16–39.

Kennedy, A. B., Chen, Q., Kirby, J. T. & Dalrymple, R. A. (2000), 'Boussinesq modeling of wave transformation, breaking, and runup. I: 1D', *Journal of Waterway, Port, Coastal, and Ocean Engineering* **126**(1), 39–47.

Kimmoun, O. & Branger, H. (2007), 'A particle image velocimetry investigation on laboratory surf-zone breaking waves over a sloping beach', *Journal of Fluid Mechanics* **588**, 353–397.

Kimmoun, O., Ratouis, A. & Brosset, L. (2010), Sloshing and scaling: experimental study in a wave canal at two different scales, *in* 'The Twentieth International Offshore and Polar Engineering Conference', OnePetro.

Kirby, J. T. (1998), 'Discussion of 'Note on a nonlinearity parameter of surface waves' by S. Beji', *Coastal Engineering* **34**(1-2), 163–168.

Kirby, J. T. (2016), 'Boussinesq models and their application to coastal processes across a wide range of scales', *Journal of Waterway, Port, Coastal, and Ocean Engineering* **142**(6), 03116005.

Kirby, J. T. & Dalrymple, R. A. (1983), 'A parabolic equation for the combined refraction–diffraction of Stokes waves by mildly varying topography', *Journal of Fluid Mechanics* **136**, 453–466.

Korteweg, D. J. & De Vries, G. (1895), 'Xli. on the change of form of long waves advancing in a rectangular canal, and on a new type of long stationary waves', *The London, Edinburgh, and Dublin Philosophical Magazine and Journal of Science* **39**(240), 422–443.

Kurnia, R. & van Groesen, E. (2014), 'High order hamiltonian water wave models with wave-breaking mechanism', *Coastal Engineering* **93**, 55–70.

Kuznetsov, K., Harris, J., Peyrard, C., Mivehchi, A., Grilli, S. & Benoit, M. (2018), Development of numerical wave tank using boundary element method with cubic B-splines, *in* 'EGU General Assembly Conference Abstracts', p. 19842.

Lachaume, C., Biausser, B., Fraunié, P., Grilli, S. T. & Guignard, S. (2003), Modeling of breaking and post-breaking waves on slopes by coupling of BEM and VOF methods, *in* 'The Thirteenth International Offshore and Polar Engineering Conference', OnePetro, pp. 353–359.

Landesman, P. (2022), Simulation d'interactions vagues-structure par un couplage bidirectionnel entre un codepotentiel complètement non-linéaire et un code Navier-Stokes, PhD thesis, École des Ponts ParisTech.

Liu, P. L.-F., Lin, P., Chang, K.-A. & Sakakiyama, T. (1999), 'Numerical modeling of wave interaction with porous structures', *Journal of Waterway, Port, Coastal, and Ocean Engineering* **125**(6), 322–330.

Liu, Y., Eeltink, D., Tang, T., Barratt, D., Li, Y., Adcock, T. & Van Den Bremer, T. (2023), 'Comparison of breaking models in envelope-based surface gravity wave evolution equations', *Physical Review Fluids* **8**(5), 054803.

Longuet-Higgins, M. S. & Cokelet, E. (1976), 'The deformation of steep surface waves on water-I. A numerical method of computation', *Proceedings of the Royal Society of London. A. Mathematical and Physical Sciences* **350**(1660), 1–26.

Lubin, P. & Glockner, S. (2015), 'Numerical simulations of three-dimensional plunging breaking waves: generation and evolution of aerated vortex filaments', *Journal of Fluid Mechanics* **767**, 364–393.

Lubin, P., Glockner, S., Kimmoun, O. & Branger, H. (2011), 'Numerical study of the hydrodynamics of regular waves breaking over a sloping beach', *European Journal of Mechanics-B/Fluids* **30**(6), 552–564.

Lubin, P., Kimmoun, O., Véron, F. & Glockner, S. (2019), 'Discussion on instabilities in breaking waves: vortices, air-entrainment and droplet generation', *European Journal of Mechanics-B/Fluids* **73**, 144–156.

Lubin, P., Vincent, S., Abadie, S. & Caltagirone, J.-P. (2006), 'Three-dimensional large eddy simulation of air entrainment under plunging breaking waves', *Coastal engineering* **53**(8), 631–655.

Lubin, P., Vincent, S., Caltagirone, J.-P. & Abadie, S. (2003), 'Fully three-dimensional direct numerical simulation of a plunging breaker', *Comptes Rendus Mecanique* **331**(7), 495–501.

Madsen, P. A., Bingham, H. B. & Liu, H. (2002), 'A new Boussinesq method for fully nonlinear waves from shallow to deep water', *Journal of Fluid Mechanics* **462**, 1–30.

Madsen, P. A. & Schäffer, H. A. (1998), 'Higher-order Boussinesq-type equations for surface gravity waves: derivation and analysis', *Philosophical Transactions of the Royal Society A* **356**, 3123–3181.

McCowan, J. (1894), 'Xxxix. On the highest wave of permanent type', *The London, Edinburgh, and Dublin Philosophical Magazine and Journal of Science* **38**(233), 351–358.

Mei, C. C. (1989), *The applied dynamics of ocean surface waves*, Vol. 1, World scientific.

Miche, R. (1944), Breaking wave motion in water of constant depth, *in* 'Annales des Ponts et Chaussees', Vol. 121, pp. 285–319.

Michell, J. H. (1893), 'On the highest waves in water', *Philosophical Magazine series 5* **365**, 430–437.

Mivehchi, A. (2018), 'Experimental and numerical simulations for fluid body interaction problems', *PhD Dissertation, University of Rhode Island.* .

Mivehchi, A., Harris, J. C., Grilli, S. T., Dahl, J. M., O'Reilly, C. M., Kuznetsov, K. & Janssen, C. F. (2017), A hybrid solver based on efficient BEM-potential and LBM-NS models: recent BEM developments and applications to naval hydrodynamics, *in* 'Proceedings of the 27th International Ocean and Polar Engineering Conference', International Society of Offshore and Polar Engineering, pp. 721–728.

Mohanlal, S., Harris, J. C., Yates, M. L. & Grilli, S. T. (2023), 'Unified depth-limited wave breaking detection and dissipation in fully nonlinear potential flow models', *Coastal Engineering* **183**, 104316.

Moin, P. & Mahesh, K. (1998), 'Direct numerical simulation: a tool in turbulence research', *Annual Review of Fluid Mechanics* **30**(1), 539–578.

Mostert, W. & Deike, L. (2020), 'Inertial energy dissipation in shallow-water breaking waves', *Journal of Fluid Mechanics* **890**.

Narayanan, C. & McCalpin, J. D. (1997), 'Vertical structure of horizontal velocity in regular shoaling waves', *Journal of Waterway, Port, Coastal, and Ocean Engineering* **123**(3), 130–136.

Newman, J. N. & Lee, C.-H. (2002), 'Boundary-element methods in offshore structure analysis', *Journal of Offshore Mechanics and Arctic Engineering* **124**(2), 81–89.

Nimmala, S. B., Yim, S. C. & Grilli, S. T. (2013), 'An efficient three-dimensional FNPF numerical wave tank for large-scale wave basin experiment simulation', *Journal of Offshore Mechanics and Arctic Engineering* **135**(2).

Nwogu, O. G. (1996), 'Numerical prediction of breaking waves and currents with a Boussinesq model', *Coastal Engineering* pp. 4807–4820.

Okamoto, T. & Basco, D. R. (2006), 'The relative trough Froude number for initiation of wave breaking: Theory, experiments and numerical model confirmation', *Coastal Engineering* **53**(8), 675–690.

Papoutsellis, C. E., Yates, M. L., Simon, B. & Benoit, M. (2019), 'Modelling of depth-induced wave breaking in a fully nonlinear free-surface potential flow model', *Coastal Engineering* **154**, 103579.

Phillips, O. (1985), 'Spectral and statistical properties of the equilibrium range in wind-generated gravity waves', *Journal of Fluid Mechanics* **156**, 505–531.

Pierella, F., Lindberg, O., Bredmose, H., Bingham, H. B., Read, R. W. & Engsig-Karup, A. P. (2021), 'The DeRisk database: Extreme design waves for offshore wind turbines', *Marine Structures* **80**, 103046.

Pomeau, Y., Le Berre, M., Guyenne, P. & Grilli, S. T. (2008), 'Wave-breaking and generic singularities of nonlinear hyperbolic equations', *Nonlinearity* **21**(5), T61.

Raoult, C. (2016), Modélisation numérique non-linéaire et dispersive des vagues en zone côtiere, PhD thesis, Paris Est.

Rapp & Melville (1990), 'Laboratory measurements of deep-water breaking waves', *Philosophical Transactions of the Royal Society of London. Series A, Mathematical and Physical Sciences* **331**(1622), 735–800.

Romero, L., Melville, W. K. & Kleiss, J. M. (2012), 'Spectral energy dissipation due to surface wave breaking', *Journal of Physical Oceanography* **42**(9), 1421–1444.

Roy, T. L. (2018), Experiments for waves breaking over a three-dimensional submerged bar, PhD thesis, Florida Atlantic University.

Schäffer, H. A., Madsen, P. A. & Deigaard, R. (1993), 'A Boussinesq model for waves breaking in shallow water', *Coastal Engineering* **20**(3-4), 185–202.

Scolan, Y.-M. & Etienne, S. (2023), 'Pressure analysis in nonlinear waves by revisiting the breaking wave onset', *European Journal of Mechanics-B/Fluids* .

Seiffert, B. R. & Ducrozet, G. (2018), 'Simulation of breaking waves using the high-order spectral method with laboratory experiments: wave-breaking energy dissipation', *Ocean Dynamics* **68**(1), 65–89.

Seiffert, B. R., Ducrozet, G. & Bonnefoy, F. (2017), 'Simulation of breaking waves using the high-order spectral method with laboratory experiments: Wave-breaking onset', *Ocean Modelling* **119**, 94–104.

Shi, F., Kirby, J. T., Harris, J. C., Geiman, J. D. & Grilli, S. T. (2012), 'A high-order adaptive time-stepping TVD solver for Boussinesq modeling of breaking waves and coastal inundation', *Ocean Modelling* **43**, 36–51.

Shi, F., Kirby, J. T., Tehranirad, B., Harris, J. C. & Grilli, S. (2011), 'FUNWAVE-TVD, fully nonlinear boussinesq wave model with TVD solver, documentation and user's manual', *Center for Applied Coastal Research, University of Delaware, Newark, DE, USA, Res. Rep. No CACR-11-04* **2**, 1.

Simon, B., Papoutsellis, C. E., Benoit, M. & Yates, M. L. (2019), 'Comparing methods of modeling depth-induced breaking of irregular waves with a fully nonlinear potential flow approach', *Journal of Ocean Engineering and Marine Energy* **5**(4), 365–383.

Smith, J. M., Sherlock, A. R. & Resio, D. T. (2001), STWAVE: Steady-state spectral wave model user's manual for STWAVE, version 3.0, Technical report, Engineer Research and Development Center Vicksburg MS Coastal and Hydraulics Lab.

Stansell, P. & MacFarlane, C. (2002), 'Experimental investigation of wave breaking criteria based on wave phase speeds', *Journal of Physical Oceanography* **32**(5), 1269–1283.

Steer, J. N., Kimmoun, O. & Dias, F. (2021), 'Breaking-wave induced pressure and acceleration on a clifftop boulder', *Journal of Fluid Mechanics* **929**, R1.

Stelling, G. & Zijlema, M. (2003), 'An accurate and efficient finite-difference algorithm for non-hydrostatic free-surface flow with application to wave propagation', *International Journal for Numerical Methods in Fluids* **43**, 1–23.

Stive, M. (1984), 'Energy dissipation in waves breaking on gentle slopes', *Coastal Engineering* **8**(2), 99–127.

Stokes, G. (1847), 'On the theory of oscillatory waves', *Transactions of the Cambridge Philosophical Society.* **8**, 441–455.

Stokes, G. G. (1880), 'Considerations relative to the greatest height of oscillatory irrotational waves which can be propagated without change of form', *Mathematical and physical papers* **1**, 225–228.

Svendsen, I. A., Madsen, P. A. & Hansen, J. B. (1978), 'Wave characteristics in the surf zone', *Coastal Engineering Proceedings* **1**(16), 29.

Taylor, G. I. (1953), 'An experimental study of standing waves', *Proceedings of the Royal Society of London. Series A. Mathematical and Physical Sciences* **218**(1132), 44–59.

Tian, Y. & Sato, S. (2008), 'A numerical model on the interaction between nearshore nonlinear waves and strong currents', *Coastal Engineering Journal* **50**(04), 369–395.

Tian, Z., Perlin, M. & Choi, W. (2010), 'Energy dissipation in two-dimensional unsteady plunging breakers and an eddy viscosity model', *Journal of Fluid Mechanics* **655**, 217–257.

Tian, Z., Perlin, M. & Choi, W. (2012), 'An eddy viscosity model for two-dimensional breaking waves and its validation with laboratory experiments', *Physics of Fluids* **24**(3), 036601.

Ting, F. C. & Kirby, J. T. (1994), 'Observation of undertow and turbulence in a laboratory surf zone', *Coastal Engineering* **24**(1-2), 51–80.

Tolman, H. L. (2009), 'User manual and system documentation of wavewatch iii tm version 3.14', *Technical note, MMAB Contribution* **276**(220).

Tonelli, M. & Petti, M. (2009), 'Hybrid finite volume–finite difference scheme for 2DH improved Boussinesq equations', *Coastal Engineering* **56**(5-6), 609–620.

Tonelli, M. & Petti, M. (2010), 'Finite volume scheme for the solution of 2D extended Boussinesq equations in the surf zone', *Ocean Engineering* **37**(7), 567–582.

Vincent, C. L. & Briggs, M. J. (1989), 'Refraction—diffraction of irregular waves over a mound', *Journal of Waterway, Port, Coastal, and Ocean Engineering* **115**(2), 269–284.

Viviano, A., Musumeci, R. E. & Foti, E. (2015), 'A nonlinear rotational, quasi-2dh, numerical model for spilling wave propagation', *Applied Mathematical Modelling* **39**(3-4), 1099–1118.

Vyzikas, T., Stagonas, D., Maisondieu, C. & Greaves, D. (2020), 'Intercomparison of three open-source numerical flumes for the surface dynamics of steep focused wave groups', *Fluids* **6**(1), 9.

Wang, W., Pákozdi, C., Kamath, A., Fouques, S. & Bihs, H. (2022), 'A flexible fully nonlinear potential flow model for wave propagation over the complex topography of the Norwegian coast', *Applied Ocean Research* **122**, 103103.

Wei, G., Kirby, J. T., Grilli, S. T. & Subramanya, R. (1995), 'A fully nonlinear Boussinesq model for surface waves. Part 1. Highly nonlinear unsteady waves', *Journal of Fluid Mechanics* **294**, 71–92.

West, B. J., Brueckner, K. A., Janda, R. S., Milder, D. M. & Milton, R. L. (1987), 'A new numerical method for surface hydrodynamics', *Journal of Geophysical Research: Oceans* **92**(C11), 11803–11824.

Yates, M. & Benoit, M. (2012), Modelisation non-lineaire et dispersive des vagues en zone cotiere: Etude comparative de deux methodes de simulation precises, *in* 'JH2018-16èmes Journées de l'Hydrodynamique. 27-29 Novembre 2018, Marseille'.

Yates, M. L. & Benoit, M. (2015), 'Accuracy and efficiency of two numerical methods of solving the potential flow problem for highly nonlinear and dispersive water waves', *International Journal for Numerical Methods in Fluids* **77**(10), 616–640.

Zakharov, V. E. (1968), 'Stability of periodic waves of finite amplitude on the surface of a deep fluid', *Journal of Applied Mechanics and Technical Physics* **9**(2), 190–194.

Zhang, J. & Benoit, M. (2021), 'Wave–bottom interaction and extreme wave statistics due to shoaling and de-shoaling of irregular long-crested wave trains over steep seabed changes', *Journal of Fluid Mechanics* **912**, A28.

Zhao, B. B., Ertekin, R. C., Duan, W. Y. & Hayatdavoodi, M. (2014), 'On the steady solitary-wave solution of the Green-Naghdi equations of different levels', *Wave Motion* **51**, 1382–1395.

Zijlema, M. & Stelling, G. S. (2008), 'Efficient computation of surf zone waves using the nonlinear shallow water equations with non-hydrostatic pressure', *Coastal Engineering* **55**, 780–790.

Zijlema, M., Stelling, G. & Smit, P. (2011), 'SWASH: An operational public domain code for simulating wave fields and rapidly varied flows in coastal waters', *Coastal Engineering* **58**(10), 992–1012.